

Investigating the performance of wind farms with alternating tower heights

MEAH no.: 289, P&E report no.: 2695

S. van Heerde

8 October 2015

To obtain the degree of Master of Science at the Delft University of Technology.

Graduation committee:

Prof.dr.ir. J. Westerweel	Delft University of Technology Faculty of Mechanical, Maritime and Materials Engineering Mechanical Engineering, Section of Fluid Mechanics
Dr.ir. M.J.B.M. Pourquie	Delft University of Technology Faculty of Mechanical, Maritime and Materials Engineering Mechanical Engineering, Section of Fluid Mechanics
Ir. J.M. Tomas	Delft University of Technology Faculty of Mechanical, Maritime and Materials Engineering Mechanical Engineering, Section of Fluid Mechanics
Dr.ir. W.A.A.M. Bierbooms	Delft University of Technology Faculty of Aerospace Engineering Aerodynamics, Wind Energy & Propulsion, Section of Wind Energy
Dr. S.R. de Roode	Delft University of Technology Faculty of Civil Engineering and Geosciences Geoscience & Remote sensing, Section of Atmospheric Physics

Abstract

Johnstone and Coleman (2012) [18] were among the first to opt the idea of wind farms with mixed tower heights and predicted an increased power production due to the decrease of losses to TKE production from the mean kinetic energy balance. In the current study, the performance of infinite wind farms with alternating tower heights imposed by a neutrally stratified half-channel boundary layer is investigated.

A LES approach is selected by using the existing LES code DALESURBAN. To model wind turbines, the non-uniform actuator disk model is selected and its implementation into DALESURBAN described. Three wind farm configurations are investigated and compared: a farm with only high turbines, a farm with tower heights alternating in row configuration and a farm with tower heights alternating in staggered configuration. When comparing the two alternating configurations, no significant difference in power production is found. For the farm with tower heights alternating in staggered configuration, the fluctuation of power production is found higher and the fatigue life expected shorter. When comparing the alternating configurations with the farm with only high turbines, an increased power production of 4% to 5% is found. However, the source for this increase is primarily the decrease of tower drag surface and not the result of decreased losses to TKE production as proposed by Johnstone and Coleman (2012) [18]. Furthermore, the fluctuation of the power production increases and the fatigue life of the high turbines is expected to decrease. As an undesirable side-effect, in the alternating configurations the fatigue life for the high turbines is found to be shorter than for the low turbines.

Investigation of tower height alternation in the infinite wind farm gave results against its application. However, the effects of flow development along the wind farm are not taken into account. Therefore, it is recommended to perform future research on wind farms with tower height alternation within an inflow-outflow model description.

Acknowledgements

My thanks go to Jasper Tomas for continuously directing me throughout the project, his patience, his clear explanations and for his time invested into the project. To my supervisors, Mathieu Pourquoi and Stephan de Roode, I am thankful for their solid input on issues, the direction to go and improvements to be made. Furthermore, I'd like to thank the members of the graduation committee: Prof.dr.ir J. Westerweel and Dr.ir. W.A.A.M. Bierbooms for their time. Lastly, my thanks goes to all the thesis students for moral support, suggestions and discussions.

Contents

1	Introduction	1
2	Theoretical background and literature	4
2.1	Basics of LES as applied within DALESURBAN	4
2.2	Kinetic energy budget of the mean flow	7
2.3	The wind turbine wake	8
2.4	Introduction of wind turbine models for LES	9
2.5	Literature on wind turbine models for LES	12
3	Methodology	16
3.1	Selection of models and methods	16
3.1.1	Selection of wind turbine model	16
3.1.2	Distribution method	17
3.1.3	Implementation in DALESURBAN	19
3.2	Methodology for model verification and validation	24
3.3	Wind turbine model validation case	25
3.4	Simulation set-up	26
3.4.1	The single domain	27
3.4.2	The infinite domain	29
3.4.3	Boundary conditions and initial conditions	30
3.4.4	Model driving force	31
4	Model verification and validation	33
4.1	Code verification	33
4.2	Calculation verification by engineering wake solutions	34
4.3	Calculation verification by Frandsen’s double-log-law theory	35
4.4	Validation by measurements	37
4.5	Conclusions on verification and validation	39
5	Results and discussion for alternating tower heights	41
5.1	Tower height difference	41
5.1.1	Appropriateness of tower height difference	42
5.1.2	Optimal tower height difference	45
5.2	Introduction of wind farm configurations	48
5.3	Power production and mean kinetic energy profiles	49
5.4	Local fluctuation of power production	51
5.5	Fatigue and flow fields	53
6	Conclusions	58
7	Recommendations and future research	60
	Bibliography	61
A	List of Symbols	64

B	Mixed tower height wind farms	68
C	Validation measurements	70
D	Known model inputs	72
D.1	Blade geometry	72
D.1.1	Number of blade elements (or annuli)	72
D.1.2	Blade measurements	73
D.2	Lift and drag coefficients	75
D.3	Rotational speed	77
E	Parameter estimation	79
E.1	Grid convergence and sensitivity and smoothing	79
E.1.1	x-grid convergence and sensitivity	80
E.1.2	yz-grid convergence and sensitivity	82
E.1.3	Smoothing and 2dx-waves suppression	84
E.2	Single domain temporal analysis	85
E.2.1	Convergence time	85
E.2.2	Statistical averaging period	86
E.2.3	Wind turbine reference velocities averaging time	88
E.2.4	Time-step and temporal discretization error	89
E.3	Subgrid modeling	91
F	The infinite domain	93
F.1	Domain dimensions	93
F.2	Power production time-series and temporal analysis	96
G	Single domain flow fields	101

Chapter 1

Introduction

Thesis background and motivation

By the end of 2013, the global wind energy capacity has reached a total of 318GW. Over 2014, a record breaking 51GW has been installed additionally [20]. Strong ongoing development calls for work on a great number of research subjects. Current major research subjects are: micro-siting and wind farm layout optimization, accurate prediction of the atmospheric boundary layer, blade optimization and modeling, detailed turbine and flow modeling, support structures and sound modeling. [2],[29]. One recently opted alternative research topic is on the performance of wind farms with mixed tower height. [18], [29]. Johnstone and Coleman (2012) [18] were the first to opt a more efficient power extraction by application of a wind farm with mixed tower height wind turbines. Johnstone and Coleman (2012) [18] performed a Large-Eddy Simulation (LES) imposed by a neutral turbulent Ekman boundary layer description for a conventional infinite wind farm. For such farm, the physics were discussed based on the mean kinetic energy profiles. At turbine height, the power extracted by the turbine is locally balanced largely by the turbulent transport of mean kinetic energy. The increased turbulence kinetic energy (TKE) production attributed to the turbines is a large fraction of the power extracted by them. The TKE production and viscous stresses represent additional sink terms that must be balanced by pressure work. These losses are found to be significant: overall TKE production is larger than the useful power extracted by the turbines, i.e. more energy is transferred into turbulence than into effective power. High values of TKE production offer no obvious direct benefit in the context of a wind farm. Rather an increase of velocity fluctuations implied by a high Reynolds stress and thus high TKE production could lead to component fatigue. For the design of the wind farm it thus seems desirable to reduce the absolute value of the Reynolds stress while keeping its gradients high at turbine height. To do this, Johnstone and Coleman (2012) [18] suggest using a mixture of mixed tower heights in the hope of obtaining a sawtooth curve for the Reynolds stress. This would imply high local gradients of the stress and thus high kinetic energy transport, but might keep its maximum level, and therefore TKE production, lower, i.e. higher energy transport and less turbulence production. [18].

Although Johnstone and Coleman (2012) suggest a more efficient power extraction due to mixed tower height wind farms, they do not perform any actual measurements or simulations onto this specific subject. A scarce total of three other publications on mixed tower height wind farms are known and described in detail in appendix B. All three publications use an optimization algorithm to optimize the number of low tower and high tower turbines over a fixed 1D length or 2D area. Wind turbines are analytically modeled according to Jensen's wake model and the imposed inflow velocity profile is analytically modeled by the logarithmic law. Acero et al. (2009) performed a 1D optimization and an increase of 10 to 24% in power production due to enabling mixed tower heights in the optimization algorithm was found. Ying Chen et al. (2015) also performed a 1D optimization and found a 6 to 12.4% increased power production. Lastly, Ying Chen et al. (2013) performed a 2D area optimization and found an increase of 4 to 7.3% in power production.

To summarize, previous work on mixed tower height wind farms consistently give an increase in power production compared to conventional wind farms. However, there is little agreement on the quantitative aspect. Additionally, only analytic models are applied, no turbulence is considered and Jensen's wake model is applied outside its intended and validated purposes: non-aligned wakes and the near wake region. Furthermore, other aspects of wind farms with mixed tower heights such as the physics and change in fatigue life, are yet to be investigated. Therefore, the research topic on wind farms with mixed tower heights is highly interesting for further advancements.

Thesis research question and general assumptions

In line with Johnstone and Coleman (2012) [18] only infinite wind farm conditions are considered in the current study. Furthermore, all simulations are imposed by a neutrally stratified half-channel boundary layer. This simplification omits the difficulty of developing and verifying a realistic atmospheric boundary layer. The Coriolis force, gravity and any thermal effects are assumed negligible. While these assumptions are significant with respect to a real atmospheric boundary layer, study into their validity is considered out of scope.

For the current study the term 'alternating tower height wind farm' is introduced, defined as a wind farm composed by two turbines with different tower heights and implemented in a structured streamwise alternating manner. Johnstone and Coleman (2012) [18] did not give guidelines or suggestions on the tower height difference and tower height spatial configuration within the wind farm. Based on these definitions and simplifications, the main research question and its sub questions are defined:

How is the power production, the fluctuation of power production and the fatigue life affected by application of tower height alternation for an infinite wind farm imposed by a neutrally stratified half-channel boundary layer?

Sub questions:

- *What tower height difference is appropriate and optimal?*
- *What wind farm configurations to consider and is there a performance difference between configurations?*
- *Are the physics as proposed by Johnstone and Coleman (2012) valid for such application?*

The power production and fluctuation of power production are chosen performance measures to give an indication of the quantity and quality of power extraction. Additionally, the fatigue life is identified as a performance measure. Summarizing the physics proposed by Johnstone and Coleman (2012) [18], the occurrence of the following is discussed:

- Decreased local and overall TKE production.
- A sawtooth curve for the Reynolds shear stress magnitude.

As infinite wind farms are considered, experimental work is not applicable and computational modeling is required. Atmospheric boundary layer flows and turbine wakes are known to be anisotropic and dominated by large-scale turbulent structures and turbulent mixing. Additionally, the flow through a wind farm comprises eddies that range in size from the smallest dissipative scales to the atmospheric boundary layer height. Widely used engineering models such as WaSP are fast and accurate for an overview of wind farm aerodynamics and gauging mean power production. However, they cannot resolve phenomena like wake meandering, the effect of atmospheric stratification and a turbine's response to partial wake interaction and yawed inflows. [26]. An alternative for engineering models are models based on the Navier-Stokes (NS) equations, such as Reynolds Averaged Navier-Stokes simulations (RANS), LES and Direct Numerical Simulations (DNS). These models solve the full relevant flow field, while the underlying turbulence model differs. RANS generally assumes isotropic turbulence and is therefore unfit for atmospheric boundary layer flows. In recent years, LES is receiving more attention in the

wind energy wake community. For LES the dominant large-scale turbulent structures are fully resolved, while the small-scale structures are treated by a subgrid model. Lastly, DNS resolves all eddies of a flow but requires very fine grids of the order of the Kolmogorov scale. This unfortunately makes application of DNS for wind turbine wakes and atmospheric boundary flows unworkable with today's computational means [26],[34]. Therefore, LES is chosen for further advancements.

To choose a proper LES code, the following considerations are stated:

- The tip speed of large turbines might approach the limit of the incompressibility assumption ($Ma=0.3$ at sea level), the flow in the wake remains incompressible. [26].
- A wind turbine wake experiences high shear near wake shear layers, which might result in overapproximation of the turbulent viscosity if not compensated. Therefore, there is a need for a dynamic Smagorinsky sub-grid model (SGM) or Vreman SGM [35], [41].

Within the Technical University of Delft, the DALES (Delft Atmospheric Large Eddy Simulation) code has been in development for many years. A spin-off of the DALES code (v.3.2) is the DALESURBAN code, mostly identical to the DALES code, however, with the advantage of having both static Smagorinsky and Vreman SGM built in. Therefore, the DALESURBAN code is chosen for further development regarding wind turbine modeling. Application of a wind turbine in DALESURBAN requires the development of a wind turbine model. To guide this development, the following sub questions are introduced:

- *What wind turbine models are applicable for LES and how have such models been implemented in literature?*
- *What model is selected, how is it implemented to DALESURBAN, to what validation case is the implementation aimed and what are its inputs?*
- *How does the model perform compared with analytic wind turbine models and experiments?*

Thesis overview

First, the basics of LES as applied in DALESURBAN are described in chapter 2, Theoretical background and literature. The mean kinetic energy budget is introduced as it is applied in the current study for analysis purposes. In order to describe characteristics of wind turbine models, the properties of the wind turbine wake are discussed. An overview of wind turbine models applicable to the selected code is given, followed by the literature on application of such models.

In chapter 3, Methodology, one wind turbine model is selected and its implementation to DALESURBAN is described. Then, the methodology for the verification and validation of the selected model is introduced and a validation case is selected. Two simulations are set-up: the simulation for model verification and validation and the infinite domain for alternating tower height wind farms. Lastly, all wind turbine model inputs are summarized.

In chapter 4, Validation, the implemented wind turbine model is verified and validated. First, code verification is performed. Then, the calculation is verified by comparing the implemented model to engineering wake solutions and Frandsen's double-log-law theory. Lastly, the model is validated by measurements as introduced by the validation case.

The fully validated wind turbine model is then finally applied with respect to the research questions in chapter 5. The sub questions are discussed and results for the power production, the fluctuation of power production and the fatigue life are given.

Chapter 2

Theoretical background and literature

First the basics of LES as applied within DALESURBAN are described and the mean kinetic energy budget is introduced. The latter is applied in the current study for analysis purposes. Then, the characteristics of the wind turbine wake are discussed. An overview of wind turbine models applicable to the selected code is given, followed by the literature on application of such models.

2.1 Basics of LES as applied within DALESURBAN

LES formulations are based on the filtered Navier-Stokes equations, as defined by equations 2.1 and 2.2. All notations follow the Einstein-summation-convention and symbols indicating the notation of filtering is omitted.

$$\frac{\partial u_i}{\partial x_i} = 0 \quad (2.1)$$

$$\frac{\partial u_i}{\partial t} + \frac{\partial u_i u_j}{\partial x_j} = -\frac{\partial}{\partial x_i} \left(\frac{p}{\rho} \right) + \nu \frac{\partial^2 u_i}{\partial x_j^2} - \frac{\partial \tau_{ij}}{\partial x_j} + M_{body}. \quad (2.2)$$

In equation 2.2, M_{body} is a collective term for all large-scale body forces. Further, the term τ_{ij} is the subgrid scale stress tensor, generally unknown and approximated by the Boussinesq hypothesis as found in equation 2.3. Here, e is the subgrid energy, δ_{ij} the Kronecker delta and ν_e the eddy viscosity.

$$\tau_{ij} = \frac{2}{3} \delta_{ij} e - 2\nu_e S_{ij} \quad (2.3)$$

In the Boussinesq hypothesis τ_{ij} consists of an isotropic part, $\frac{2}{3} \delta_{ij} e$ and an anisotropic part, $-2\nu_e S_{ij}$. The isotropic part may be lumped with the pressure into the so-called modified pressure term. For the anisotropic part S_{ij} is defined according to equation 2.4 and therefore, the anisotropic part may be lumped with the diffusion term, as found in equation 2.5.

$$S_{ij} = \frac{1}{2} \left(\frac{\partial u_i}{\partial x_j} + \frac{\partial u_j}{\partial x_i} \right) \quad (2.4)$$

$$\frac{\partial u_i}{\partial t} + \frac{\partial u_i u_j}{\partial x_j} = -\frac{\partial p_{mod}}{\partial x_i} + \frac{\partial}{\partial x_j} (2(\nu + \nu_e) S_{ij}) + M_{body} \quad (2.5)$$

Code flowchart

Figure 2.1 gives a simplified flowchart of the DALESURBAN code. The code consist of two main steps: first fill in the Navier-Stokes equations and second, solve the Navier-Stokes equations. These two steps are repeated every Runga-Kutta (RK) time integration step within each full time-step. Time integration is achieved by application of an explicit three-stage Runga-Kutta method wherein the value of any term for the current time-step, χ^{m+1} , is calculated based on the previous time-step according to three Runga-Kutta steps as described by equations 2.6, 2.7 and 2.8.

$$\chi^{RK1} = \chi^m + \frac{\Delta t}{3} \left(\frac{\partial \chi}{\partial t} \right)^m \quad (2.6)$$

$$\chi^{RK2} = \chi^m + \frac{\Delta t}{2} \left(\frac{\partial \chi}{\partial t} \right)^{RK1} \quad (2.7)$$

$$\chi^{m+1} = \chi^m + \Delta t \left(\frac{\partial \chi}{\partial t} \right)^{RK2} \quad (2.8)$$

Here, Δt is either a predefined fixed time-step or a dynamic time-step based on the CFL-criterion. For all momentum terms, the required time-derivatives are found by means of the pressure-correction method.

Pressure-correction method

The Navier-Stokes' equation as defined in equation 2.5 may be written discretized as equation 2.9, with superscript 'n' indicating Runga-Kutta steps.

$$\frac{u_i^{n+1} - u_i^n}{\Delta t_{RK}} = - \left(\frac{\partial p_{mod}}{\partial x_i} \right)^n - \frac{\partial \tilde{p}}{\partial x_i} + Rem^n \quad (2.9)$$

Where \tilde{p} is a correction for the fact that the pressure gradient at the previous time step is used, i.e. $p^{n+1} = p^n + \tilde{p}$. Furthermore, the term Rem^n is a collective term including advection, diffusion and body-forces. Equation 2.9 may be split into two components by application of a prediction velocity u^* , as found in equations 2.10 and 2.11.

$$\frac{u_i^* - u_i^n}{\Delta t_{RK}} = - \left(\frac{\partial p_{mod}}{\partial x_i} \right)^n + Rem^n \quad (2.10)$$

$$\frac{u_i^{n+1} - u_i^*}{\Delta t_{RK}} = - \frac{\partial \tilde{p}}{\partial x_i} \quad (2.11)$$

Taking the divergence of equation 2.11 gives equation 2.12. Due to mass conservation, $\nabla \bar{u}_i^{n+1} = 0$, equation 2.12 simplifies to equation 2.13.

$$\nabla \left(\frac{u_i^{n+1}}{\Delta t_{RK}} \right) - \nabla \left(\frac{u_i^*}{\Delta t_{RK}} \right) = -\nabla^2 \tilde{p} \quad (2.12)$$

$$\nabla \left(\frac{u_i^*}{\Delta t_{RK}} \right) = \nabla^2 \tilde{p} \quad (2.13)$$

The LHS of equation 2.13 is found by taking the divergence of equation 2.10 and reordering as in equation 2.14. Equation 2.13 is then solvable for the RHS by application of a Poisson solver.

$$\nabla \left(\frac{u_i^*}{\Delta t_{RK}} \right) = -\nabla \left(\frac{\partial p_{mod}}{\partial x_i} \right)^n + \nabla \left(\frac{u_i^n}{\Delta t_{RK}} \right) + \nabla Rem^n \quad (2.14)$$

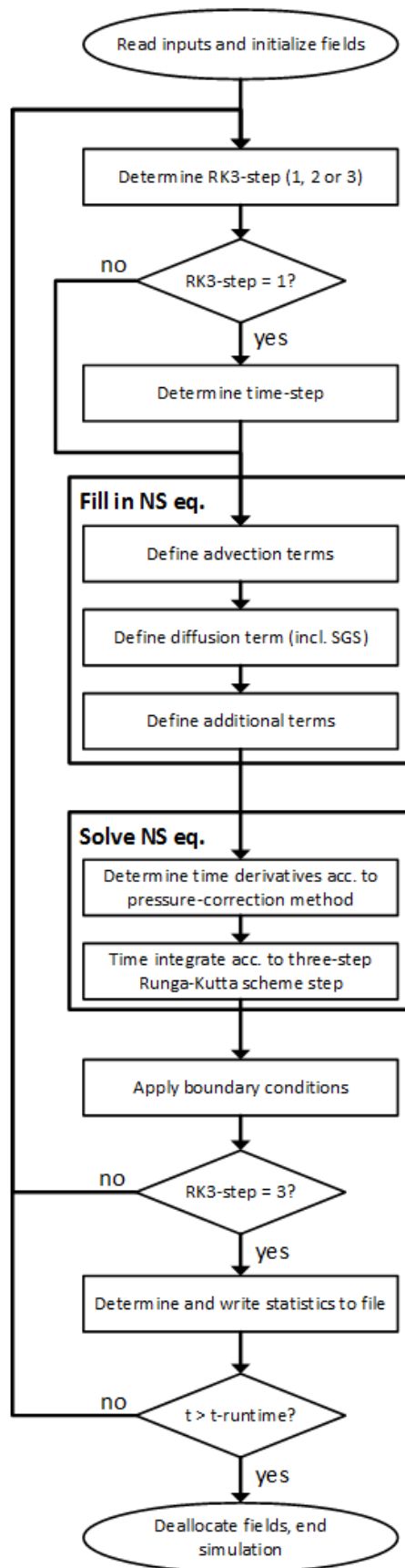


Figure 2.1: Flowchart of the DALESURBAN code.

2.2 Kinetic energy budget of the mean flow

The energy budget of the mean flow is found by multiplying the Reynolds averaged Navier-Stokes equations with \bar{u}_i . The fully developed (converged) mean flow is considered stationary: $\frac{\partial \bar{u}_i}{\partial t} = 0$, resulting in equation 2.15 for the energy budget of the mean flow.

$$\bar{u}_i \frac{\partial \bar{u}_i \bar{u}_j}{\partial x_j} = -\bar{u}_i \frac{\partial \bar{p}_{mod}}{\partial x_i} + \bar{u}_i \frac{\partial}{\partial x_j} (2(\overline{\nu + \nu_e}) \bar{S}_{ij}) - \bar{u}_i \frac{\partial \overline{u'_i u'_j}}{\partial x_j} - \bar{u}_i M_{body} \quad (2.15)$$

By application of the product rule for derivatives, equation 2.15 is rewritten into equation 2.16 as four components [30]: kinetic energy work, transport, production and extraction, respectively given in equations 2.17, 2.18, 2.19 and 2.20.

$$0 = \bar{\mathcal{W}} + \bar{\mathcal{T}} + \bar{\mathcal{P}} + \bar{\mathcal{E}} \quad (2.16)$$

$$\bar{\mathcal{W}} = -\bar{u}_i \frac{\partial \bar{p}_{mod}}{\partial x_i} \quad (2.17)$$

$$\bar{\mathcal{T}} = \underbrace{-\bar{u}_i \frac{\partial \bar{u}_i \bar{u}_j}{\partial x_j}}_{\text{advection}} - \underbrace{\frac{\partial}{\partial x_j} (\bar{u}_i \overline{u'_i u'_j})}_{\text{Reynolds stresses}} + \underbrace{\frac{\partial}{\partial x_j} (2\bar{u}_i (\overline{\nu + \nu_e}) \bar{S}_{ij})}_{\text{viscous and subgrid}} \quad (2.18)$$

$$\bar{\mathcal{P}} = \underbrace{\overline{u'_i u'_j} \frac{\partial \bar{u}_i}{\partial x_j}}_{\text{Reynolds stresses}} - \underbrace{2(\overline{\nu + \nu_e}) \bar{S}_{ij} \bar{S}_{ij}}_{\text{viscous and subgrid}} \quad (2.19)$$

$$\bar{\mathcal{E}} = \bar{u}_i M_{body} \quad (2.20)$$

The work term, \mathcal{W} , describes the mean work performed by the set pressure gradient. The transport term, \mathcal{T} , is responsible for transporting or distributing KE over the domain. This term consists of four different components: advective transport, transport due to Reynolds stresses, transport due to viscous stresses and transport due to subgrid stresses. The production term, \mathcal{P} , is a loss in KE and is better known as the production term for turbulent kinetic energy. This term consists of three different components: production due to Reynolds stresses, production due to viscous stresses and production due to subgrid stresses. The extraction term, \mathcal{E} , is the direct result of body forces.

Due to the complexity of the discretization, the transport term is not calculated explicitly and is found as the residual of all other terms by equation 2.21.

$$\bar{\mathcal{T}} = -\bar{\mathcal{W}} - \bar{\mathcal{P}} - \bar{\mathcal{E}} \quad (2.21)$$

1D profiles of the kinetic energy budget of the mean flow

For assessment of the energy budget, 1D profiles in wall-normal direction are used. These profiles are defined according to equation 2.22 analogously for each component.

$$\bar{\mathcal{W}}(z_k) = \sum_{N_x} \sum_{N_y} \bar{\mathcal{W}}(x_i, y_j, z_k) \frac{\Delta x \Delta y}{L_x L_y} \quad (2.22)$$

Domain averaged kinetic energy budget of the mean flow

Additionally, an energy budget for the whole domain is introduced according to equation 2.23. By definition, the integral of the transport term over the whole domain equals zero [30]. Therefore, the transport term is not explicitly present in equation 2.23, yet lumped in a newly introduced budget error, $E_{budgets}$. This budget error is defined by 2.24 and is thus the resultant of equation 2.23. Practically, this integral is calculated according to equation 2.25, analogously for each component and following up on the previously defined 1D profiles.

$$0 = \iiint \bar{W}dV + \iiint \bar{P}dV + \iiint \bar{\mathcal{E}}dV + E_{budgets} \quad (2.23)$$

$$E_{budgets} = - \iiint \bar{W}dV - \iiint \bar{P}dV - \iiint \bar{\mathcal{E}}dV \quad (2.24)$$

$$\iiint \bar{W}dV = \sum^{N_z} \bar{W}(z_k)L_xL_y\Delta z \quad (2.25)$$

2.3 The wind turbine wake

A wind turbine subtracts momentum from the flow, thereby forming two straightforward wake characteristics: decreased velocity and increased turbulence. For the turbulence within a wake, three main sources may be identified [34]:

- Atmospheric turbulence
- Mechanical turbulence
- Wake turbulence

The latter two sources are wind turbine specific. Mechanical turbulence is the result of the direct interaction of the flow with the blades, tower and nacelle. Wake turbulence on the other hand results from shear layers and the breakdown of tip vortices. Tip vortices describe helical trajectories and are the product of the roll-up of vortex sheets[39]. Further downstream of the rotor these tip vortices break down, inducing additional wake turbulence and therewith thickening of the shear layer. The break down of tip vortices has been found to occur about 2 to 4 rotor diameter lengths downstream of the turbine, the distance at which the peak turbulence is generally observed [26]. Additionally, the wake experiences wake rotation and wake meandering. Wake rotation occurs in opposite rotation direction to the direction of rotation of the turbine [24]. Wake meandering is the appearance of a low-frequency fluctuation both in the wake and in the flow outside.[24, 25]

The wind turbine wake may be divided into two regions: the near wake region and the far wake region. The downstream division distance between these two regions is defined as the point at which the shear layer created near the the blades' tips thickens with downstream distance and merges near the wake's center line. As noted, additional shear layer thickening is caused by tip vortex breakdown, therefore, the division between near wake and far wake region is again found to occur about 2 to 4 rotor diameter lengths downstream of the turbine [26, 39]. The near wake and far wake regions may be considered as two separate research areas: near wake research and far wake research. Near wake research is specifically focused on the performance and physical process of power production. Both mechanical and wake turbulence play an important role on near wake characteristics, as is wake rotation and the occurrence, production and development of helical tip vortices. Furthermore, other mechanical processes as blade bending, blade vibrations and noise generation may be considered [39]. Far wake research is specifically focused on the mutual influence when wind turbines are placed in clusters. Mechanical turbulence becomes insignificant compared to atmospheric and wake turbulence [33, 34], while all tip vortices are assumed to have broken down in the near wake region. Tip vortices are therefore commonly neglected in far wake research.

2.4 Introduction of wind turbine models for LES

Wind turbine modeling for the current study is focused on far wake applications: no mechanical turbulence is considered and modeling of tip vortices is optional. Additionally, only wind turbine models applicable for Navier-Stokes based solutions are introduced. Figure 2.2 gives a hierarchical overview of wind turbine models. Two main types are identified on level 1 [34]:

- Model the wind turbine as a distributed momentum sink
- Model the wind turbine as actual rotating solid geometry

The application of the latter of these two with respect to the far wake study focus is rarely found in literature, one example being the work of Gross [16] in which the blades are modeled as solid geometry following the cubic grid cells. For the momentum sink models, the wind turbine forces are modeled as an additional momentum sink term added to the filtered Navier-Stokes equation. The momentum sink, here expressed as a cartesian vector \mathbf{M} , is defined according to equation 2.26. Here, $A_{cell,\perp}$ is the cell surface perpendicular to the Cartesian flow direction and the term $(\mathbf{F}/(\rho A))$ is the force per unit mass vector and differs in magnitude for each type of momentum sink model.

$$\mathbf{M} = \left(\frac{\mathbf{F}}{\rho A} \right) \frac{A_{cell,\perp}}{V_{cell}} = \left(\frac{\mathbf{F}}{\rho A} \right) \frac{1}{dx} \quad (2.26)$$

On level 2 of figure 2.2, the momentum sink models are introduced. Figure 2.3 gives an illustrated overview of the three momentum sink based models [34]:

- Actuator disk model, uniform or non-uniform (ADM)
- Actuator line model (ALM)
- Actuator surface model (ASM)

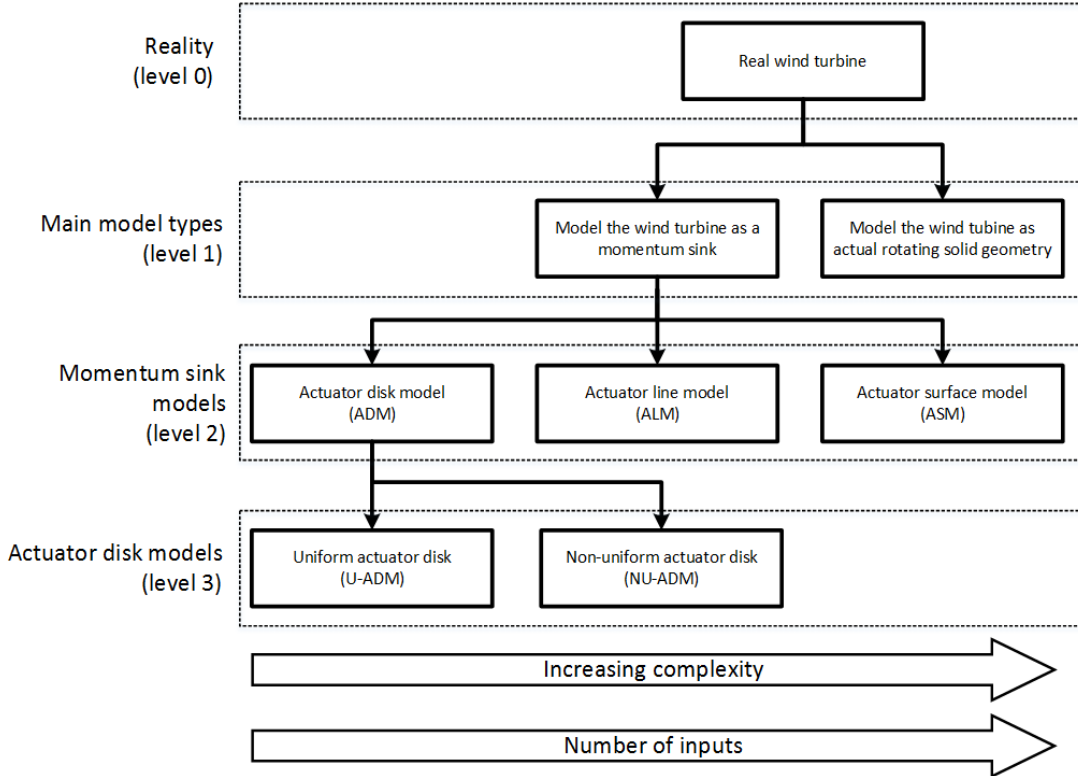


Figure 2.2: Hierarchical overview of wind turbine models. The models have been ordered by increasing complexity and number of inputs per hierarchical level.

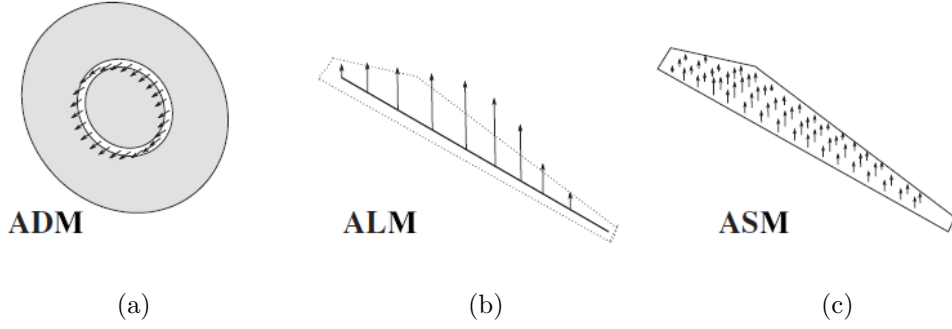


Figure 2.3: Types of distributed momentum sink models (level 2) (modified from[34]).

Uniform actuator disk model (U-ADM)

For the U-ADM the applied force per unit mass on the flow is defined by equation 2.27.

$$\frac{\mathbf{F}}{\rho A} = -\frac{1}{2}u_{ref}^2 C_T^{loc} \quad (2.27)$$

The applied force of the U-ADM depends on a local thrust coefficient, C_T^{loc} , and a streamwise reference velocity, u_{ref} . The thrust force only acts streamwise and thus the force vector \mathbf{F} is only non-zero for the streamwise direction. Distribution of the resulting momentum sink over the LES grid underlying the disk may be performed according to various methods, for example an area-factorization based distribution or a regularized smoothing by a Gaussian filter. As the grid and actuator disk do not geometrically change over time, the distribution is constant in time. Due to the fact that: the U-ADM only models a streamwise applied force and the only modeled wake phenomena is a velocity deficit, the U-ADM is only expected to give acceptable results in the far wake region. A summary of the explanation above is found in table 2.1.

Non-uniform actuator disk model (NU-ADM)

For the NU-ADM, the applied force per unit mass on the flow is defined by equation 2.28 and a non-zero streamwise, spanwise and wall-normal component holds.

$$\frac{\mathbf{F}}{\rho A} = -\frac{1}{2}U^2 \frac{Bc}{2\pi r} (C_l \mathbf{e}_l + C_d \mathbf{e}_d) \quad (2.28)$$

Here, B is the number of blades, r is the radius of the blade element and c is the chord of the blade element. Additionally, equation 2.28 requires the lift and drag coefficients, C_l and C_d . The vectors \mathbf{e}_l and \mathbf{e}_d are unit vectors in the direction of lift and drag. More detail on the calculation of the velocity relative to the blade, U , and these unit vectors is found in chapter 3.1.3. Equation 2.28 has its origin in the blade element theory. In this theory, the blade is divided into multiple elements and for each element a constant geometry is assumed [22]. The definition and distribution of the forces is performed over annuli corresponding with the chosen blade elements, as illustrated by figure 2.3(a). All relevant geometry remains constant over time, therefore the distribution is constant over time. The NU-ADM models two wake phenomena: a velocity deficit and wake rotation, and thus, the NU-ADM is expected to give acceptable results in the far wake region. A summary of the explanation above is found in table 2.1.

Actuator line model (ALM)

For the ALM, the applied force per unit mass on the flow is defined by equation 2.29. Again, the applied force vector contains a non-zero streamwise, spanwise and wall-normal component.

$$\frac{\mathbf{F}}{\rho A} = -\frac{1}{2}U^2 c (C_l \mathbf{e}_l + C_d \mathbf{e}_d) \quad (2.29)$$

Equation 2.29 differs from equation 2.28 only due to disk-averaging; locally, the force is determined based on the number of blades divided over the circumference of the annulus, hence the $\frac{B}{2\pi r}$ term. This has its origin from the fact that actuator disk models average the local forces (at blade location) over a disk (or annulus). As the ALM applies the force only at the location of the blade, the distribution of the applied force changes over time based on the rotational speed of the turbine. Contrary to the NU-ADM, the ALM is capable of modeling tip-vortices [34]. Therefore, the actuator line model is expected to give acceptable results for both near wake as far wake regions. A summary of the explanation above is found in table 2.2.

Actuator surface model (ASM)

For the actuator surface model (ASM) the applied force on the flow is defined by equation 2.30. This model has been developed by Shen et al and is yet highly experimental [36]. The required inputs for the actuator surface model are chord-wise pressure and skin friction distributions.

$$\frac{\mathbf{F}}{\rho A} = -f_{2D} F_{distr}(\xi) \quad (2.30)$$

The term f_{2D} is the skin friction and $F_{distr}(\xi)$ is determined by fitting empirical functions to chord-wise pressure distributions [34]. More detail on this model can be found in the article by Shen et al [36]. The ASM is however not considered a feasible model for application due to the high complexity of the model and the required inputs that are difficult to obtain. Some additional properties of the actuator surface model are given in table 2.2.

Table 2.1: Overview of properties of the actuator disk models (ADM) (level 3).

Property	U-ADM	NU-ADM
Inputs	$C_T^{loc}(u_{ref})$, turbine geometry	$C_l(Re, \alpha), C_d(Re, \alpha), \Omega$, turbine and blade geometry
Distribution	constant over disk	constant over annuli
Modeled phenomena	velocity deficit	velocity deficit, wake rotation
Application	far wake	far wake

Table 2.2: Overview of properties of the actuator line and actuator surface models (level 2).

Property	ALM	ASM
Inputs	$C_l(Re, \alpha), C_d(Re, \alpha), \Omega$, turbine and blade geometry	$Cp_{distr}(Re, \alpha), Cf_{distr}(Re, \alpha), \Omega$, turbine and blade geometry
Distribution	time-dependent over rotating line	time-dependent over rotating surface
Modeled phenomena	velocity deficit, wake rotation, tip vortices	velocity deficit, wake rotation, tip vortices
Application	far wake and near wake	far wake and near wake

2.5 Literature on wind turbine models for LES

There are three main groups actively publishing a large variety of articles on topics wherein wind turbine(s) are applied within a Large-Eddy Simulation description:

- John Hopkins University, Baltimore, Maryland, USA, lead by C. Meneveau
- KU Leuven, Leuven, Belgium, lead by J. Meyers
- École Polytechnique Fédérale de Lausanne, Lausanne, Switzerland, lead by F. Porté-Agel

Additionally, the application of the study by Johnstone and Coleman (2012) [18] is noted. For each group, first, the type of actuator disk(s) and its driving inputs are given. Then, the method of distribution of the forces on the LES grid is described and, if applicable, the direction of smoothing is discussed. For smoothing, two types may be applied: radial smoothing and axial smoothing. Smoothing is recommended to avoid singular behavior and numerical instabilities such as 2dx-waves and Gibbs instabilities [37][28].

John Hopkins University

For the JHU-LES (John Hopkins University -LES) the application of the wind turbine model starts at the definition of the total actuator thrust force on the flow, F_t , as given by equation 2.31 [4].

$$F_t = -\frac{1}{2}\rho C_T u_\infty^2 \frac{\pi}{4} D_{disk}^2 \quad (2.31)$$

Here, the thrust coefficient, C_T is defined as function of the upstream undisturbed reference velocity, u_∞ . Equation 2.31 is only applicable for research on isolated turbines as the undisturbed reference velocity is unknown for turbines disturbed by a upstream turbine wake. Therefore, a method is implemented to relate the force of each turbine to a local reference velocity, u_{disk} . Classic actuator disk theory allows the use of equation 2.32 to transform the undisturbed disk velocity into the disk velocity by application of the induction factor, a . Equation 2.33 then gives a definition of the local thrust coefficient, C_T^{loc} .

$$u_\infty = \frac{u_{disk}}{(1-a)} \quad (2.32)$$

$$C_T^{loc} = \frac{C_T}{(1-a)^2} \quad (2.33)$$

The total thrust force as function of the disk reference velocity is then given by equation 2.34. Here, the term $\langle \bar{u}^T \rangle_{disk}^2$ stands for the disk averaged and time-averaged local disk velocity. Time-averaging is performed by application of a one-sided exponential time filter, whereas the averaging time-scale is defined by equation 2.35.

$$F_t = -\rho \frac{1}{2} C_T^{loc} \langle \bar{u}^T \rangle_{disk}^2 \frac{\pi}{4} D_{disk}^2 \quad (2.34)$$

$$\frac{T u_\tau}{\delta} = 0.27 \quad (2.35)$$

In equation 2.35, u_τ is the friction velocity (including turbines) and δ is the boundary layer height. For the relevant thrust coefficient, typical values for existing wind turbines, $C_T = 0.75$ and $a = 1/4$, are applied. This leads to $C_T^{loc} = 4/3$ assumed as a constant model input. For the distribution of the total thrust force over the grid, area-factorization is applied. Here, the area-factor variable is defined as $\gamma_{j,k}$. For the disk interior grid points representing cells entirely

contained inside the disk, $\gamma_{j,k} = 1$ holds. For cells with partial overlap, the factor corresponds to the fractional area overlap of the disk within that cell. Equation 2.36 gives the distributed force (per unit mass) in the streamwise direction at a given grid point.

$$\left(\frac{\mathbf{F}}{\rho A}\right)_{i,j,k} = -\frac{1}{2}C_T^{loc}\langle\bar{u}^T\rangle_{disk}^2\gamma_{j,k} \quad (2.36)$$

Due to the application of distribution by area-factorization, no smoothing of the forces is applied. Table 2.3 gives a summary of the JHU application and a comparison with other applications, while figure 2.4 gives a plot of the applied distribution.

KU Leuven

The KU Leuven application follows the same method for the definition of the total undistributed thrust force as the JHU application as given in equation 2.34 [4]. Distribution of the force over the mesh and the definition of the disk-averaged and time-averaged reference velocity is performed differently for the KU Leuven application and allows for a rotation of the disk over any axis. In a first step, turbine forces are described in the turbine-rotor plane. In a second step, these forces are smoothed over the grid using a Gaussian convolution filter on locations which correspond to the coordinates of the LES grid. Two frames of reference are of relevance. First, the coordinate system in the turbine rotor plane is defined by $\mathbf{y} = (y_1, y_2)$ with origin in the rotor center and y_1 and y_2 the horizontal and vertical direction on this rotor plane respectively. Second, in the LES coordinate frame, the rotor plane is given by \mathbf{x}_t which satisfies $\mathbf{e}_\perp \cdot (\mathbf{x}_t - \mathbf{x}_0) = 0$ with \mathbf{x}_0 the coordinate of the rotor center and \mathbf{e}_\perp a unit vector perpendicular to the rotor plane. The distributed forces in the LES coordinate frame are defined by equation 2.37.

$$\left(\frac{\mathbf{F}}{\rho A}\right)_{i,j,k} = Q_{ij}\mathcal{F}_{t,j}(\mathbf{x}) \quad (2.37)$$

Here, Q_{ij} is a rotation matrix accounting for possible different orientations between the rotor plane, \mathbf{y} , and the LES \mathbf{x} coordinate frame. $\mathcal{F}_{t,j}(\mathbf{x})$ is the turbine thrust force smoothed over the grid by a Gaussian convolution filter in the LES coordinate frame as defined by equation 2.38, with \mathbf{x}^c the coordinates of the closest disk position relative to the relevant cell. Furthermore, δ_{dirac} is the Dirac function and the selected Gaussian filter is defined by equation 2.39.

$$\mathcal{F}_{t,j}(\mathbf{x}) = \left(\frac{F_t}{\rho A}\right) (\mathbf{y}(\mathbf{x}^c - \mathbf{x}_0)) * (G(\mathbf{x} - \mathbf{x}^c)\delta_{dirac}(\mathbf{e}_\perp \cdot (\mathbf{x}^c - \mathbf{x}_0))) \quad (2.38)$$

$$G(\mathbf{x}) = \frac{6^{(3/2)}}{\epsilon^3\pi^{(3/2)}}exp\left[-\frac{6\|\mathbf{x}\|^2}{\epsilon^2}\right] \quad (2.39)$$

In equation 2.39, ϵ is a regularization kernel, chosen as $1.5h$ with h the grid spacing in the relevant direction. This method of distribution allows for the smoothing of the applied forces in the turbine-rotor plane and axial direction. A similar distribution approach is also applicable for the non-uniform actuator disk method and the actuator line method. Table 2.3 gives a summary of the KU Leuven application and a comparison with other applications, while figure 2.4 gives a plot of the applied distribution. Spatial averaging of the reference velocities is performed accordingly. Furthermore, one-sided exponential time-averaging of the reference velocities is performed according to the time-scale T defined by equation 2.35 set at 0.60.

École Polytechnique Fédérale de Lausanne

Porté-Agel (2011) [32] implemented three wind turbine models: the uniform actuator disk, non-uniform actuator disk and actuator line model. For all three models, the force on the flow per unit mass is defined by equations 2.27, 2.28 and 2.29 respectively. For the uniform actuator disk,

the instantaneous streamwise velocity at disk center is taken as reference velocity. For the other two models, the relative velocity is analogously defined as described in chapter 3.1.3 for each separate blade element, while instantaneous reference velocities are used.

Distribution of the force is again performed by smoothing over the grid by application of a Gaussian convolution filter. Furthermore, Porté-Agel (2011) implements all three wind turbine models oriented perpendicular to the bulk flow, resulting in a simplified expression for the Gaussian convolution filter by equation 2.40 [32]. Here, η_ϵ , is defined by equation 2.41.

$$\left(\frac{\mathbf{F}}{\rho A}\right)_{i,j,k} = \left(\frac{\mathbf{F}}{\rho A}\right) * \eta \quad (2.40) \quad \eta = \frac{1}{\epsilon^3 \pi^{(3/2)}} \exp\left[-\frac{d}{\epsilon}\right]^2 \quad (2.41)$$

In equation 2.41, the term d is the distance between grid points and points representing the actuator disk and is comparable with the term $\|\mathbf{x}^c - \mathbf{x}_0\|$ as applied by the KU Leuven application. Furthermore, ϵ is chosen as Δx , the grid spacing in streamwise direction for an uniform grid [44]. Application of equation 2.40 results in both radial and axial smoothing. Additionally, Porté-Agel (2011) [32] also applied the tower and nacelle as uniform drag force surfaces distributed over the LES grid in a similar way as described in equation 2.40. Table 2.3 gives a summary of the Lausanne application and a comparison with other applications, while figure 2.4 gives a plot of the applied distribution.

University of Southampton

Johnstone and Coleman (2012) [18] essentially apply the same method as applied by the John Hopkins University to define the total thrust force of the disk on the flow, as previously defined by equation 2.34. Here, C_T^{loc} is set at 2 corresponding to the Betz limit. The reference velocity is only spatially averaged over the disk by area-factorization. The resulting momentum sink is distributed over several grid points in the axial direction and similar smoothing is performed in the radial direction at the edge of the disk. Equation 2.42 describes this smoothing.

$$\left(\frac{\mathbf{F}}{\rho A}\right)_{i,j,k} = -\frac{\left(\frac{\mathbf{F}}{\rho A}\right)}{\sqrt{\pi}\epsilon_x} \exp\left(-\left[\frac{d_x}{\epsilon_x}\right]^2\right) \frac{1}{2} \left[1 - \operatorname{erf}\left(\frac{r^2 - r_{disk}^2}{D_{disk}\epsilon_r}\right)\right] \quad (2.42)$$

Here, d_x is the axial distance between the grid points and the points representing the actuator disk. ϵ_x and ϵ_r are again regularization kernels controlling the smoothing and are set at $\frac{1}{10}D_{disk}$ and $\frac{1}{16}D_{disk}$, respectively. These imposed parameters are however case-specific and dependent on the diameter of the disk and the grid. Both in-plane and axial smoothing is applied, while the method applied for smoothing is only applicable for uniform actuator disks. Additionally, Johnstone and Coleman (2012) [18] also implemented rotation of the actuator disk over its z-axis, i.e. swivel of the disk. This method is however not described in detail. Table 2.3 gives a summary of the Southampton application and a comparison with other applications, while figure 2.4 gives a plot of the applied distribution.

Summary and comparison of distributions

Table 2.3 gives a summary of presented methods for wind turbine modeling in LES. Figure 2.4 compares the continuous smoothing / distribution of the presented methods. In figure 2.4, the JHU distribution is radial only and cuts off directly at the disk edge. Both KU Leuven and Lausanne applications apply axial and radial smoothing by a Gaussian convolution filter. Although the applied Gaussian filters differ for the KU Leuven and Lausanne applications, the resulting smoothing is near identical due to different values for the regularization kernels, ϵ . Furthermore, the KU Leuven and Lausanne applications only exhibit radial smoothing past the actuator disk edge, while for the Southampton application radial smoothing already starts within the actuator disk and drops to exactly 50% of the central uniform forcing at the actuator disk edge. Under the correct settings, all distributions are continuously self-containing, i.e. the integral of the continuous distributed force, as plotted in figure 2.4, matches the real total force,

as defined by equation 2.34. The smoothing is applied on a computational spatial grid and thus discretization of continuous smoothing occurs. Due to this discretization, an error between this continuous smoothing and the resulting discretized smoothing is introduced. Minimization of this error is possible by two methods. First the application of an as fine as possible grid over the disk. Or, second, grid-specific fine-tuning of the regularization kernels to ensure correct match between the real total force, again as defined by equation 2.34, and the total sum of the distributed force. The second method is applied by the University of Southampton, while for the other applications no notice is made of this discretization error. Moreover, the second method requires iterative fine-tuning, only feasibly applicable with regards to the required wall-clock time for actuator disk models with a constant distribution.

Table 2.3: Summary and comparison of application of wind turbine models in LES by research group.

Property	JHU	KU Leuven	Lausanne	Southampton
Disk type	uniform	uniform & line	uniform, non-uniform & line	uniform
Driving inputs	constant C_T	constant C_T	all variable	constant C_T
Distribution	area-factorization	Gaussian convolution filter	Gaussian convolution filter	equation 2.42
Smoothing	none	radial & axial	radial & axial	radial & axial
Specifics	fixed disk	all-axis rotation	fixed disk, tower & nacelle	z-axis rotation

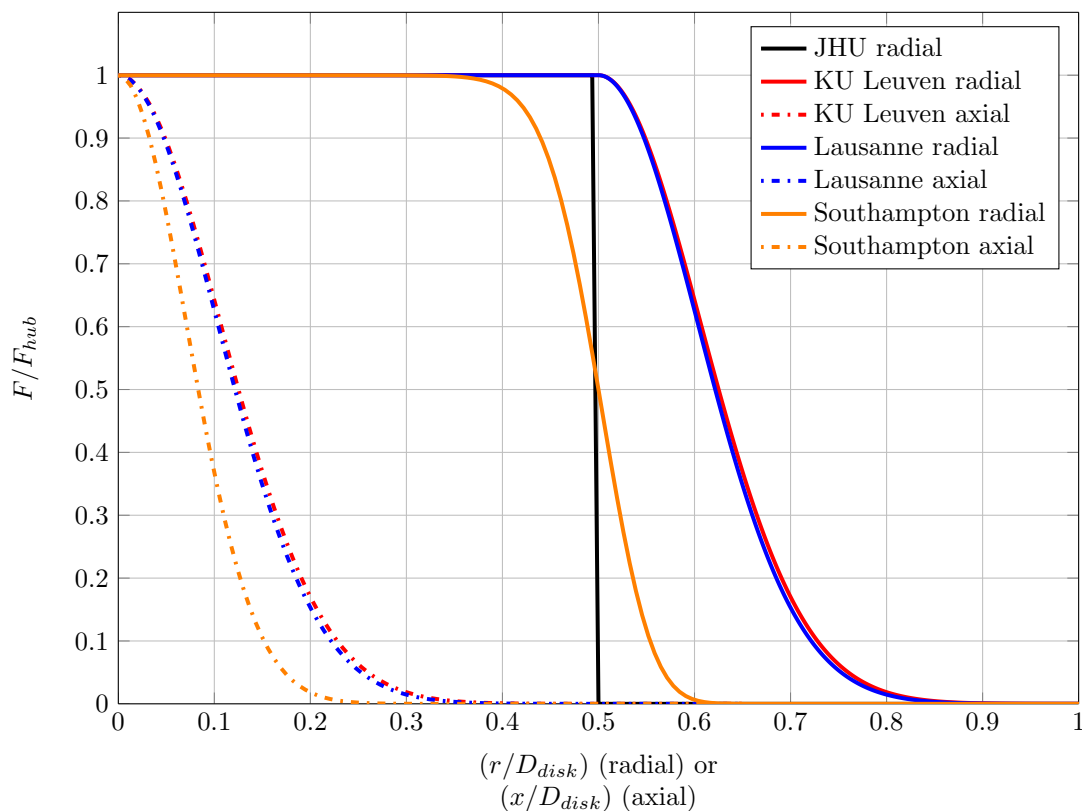


Figure 2.4: Comparison of distribution methods from literature.

Chapter 3

Methodology

From the overview of applicable wind turbine models as presented in chapter 2 a wind turbine model is selected and the distribution method described. Then, the methodology for the development of the selected wind turbine model is introduced and a validation case is selected. Two simulations are set-up: the simulation for model verification and validation and the infinite domain for wind farms. Lastly, all wind turbine model inputs are summarized.

3.1 Selection of models and methods

To select the model to implement, two selections are required: first the selection of the actuator disk model and second the selection of the distribution method. The following model requirements are set with respect to the research question:

- Far wake research focused, i.e. wake interactions between turbines are of importance while near wake phenomena such as tip vortices and mechanical turbulence are not considered relevant.
- Constant wind direction, constant driving force.
- Actuator disk plane fixed and oriented perpendicular to streamwise direction.
- Actuator disk plane oriented on cubic grid.
- Application of smoothing by distribution to give control over singular behavior and numerical instabilities.

3.1.1 Selection of wind turbine model

From section 2.5 it is found that the majority of far wake research applies the uniform actuator disk model (U-ADM). This model requires a thrust coefficient. For alternating tower height wind farms, two different tower heights are implemented and non-aligned wakes occur. Currently, the value of the thrust coefficient is unknown and it is unclear if the thrust coefficients are identical for turbines with different tower heights. Therefore, the thrust coefficient cannot be estimated as a constant and a relation between the thrust coefficient and the reference velocity is required. Determination of this relationship can either be performed experimentally or computationally. One computational method is by application of the Blade Element Theory [22]. Here, the thrust coefficient is determined as a result of the turbine blade geometry and its lift and drag coefficients. Execution of this practice is the basis behind the non-uniform actuator disk model (NU-ADM). Therefore, instead of implementing the simpler U-ADM with the requirement to determine the thrust coefficient as function of the reference velocity, the NU-ADM is selected for implementation. Additionally, the actuator line model (ALM) is not selected due to the higher complexity and the non-constant nature of the location of the forces. Furthermore, tip-vortices as modeled by the ALM require the application of a relatively high resolution grid, which is unlikely to be feasible for the final infinite domain with respect to wall-clock time.

From section 2.5 it is also found that the tower and nacelle are mostly neglected. Turbines with different tower heights experience a difference in tower drag due to a difference in tower drag surface. The influence on performance measures by tower height alternation is yet unclear. As a result, it is unclear whether or not the influence of the tower and nacelle is negligible. Therefore, the tower and nacelle are taken into consideration and implemented in the wind turbine model. To summarize:

- The NU-ADM is the selected model for implementation.
- Additionally, the tower and nacelle are implemented.

3.1.2 Distribution method

The applied distribution method is not directly a selection of previously applied methods as described in the literature, section 2.5. Rather, a custom method is implemented with the following aims:

- Minimize spread and maximize concentration.
- Fix discretization error between continuous smoothing and discretized smoothing.

The first aim is based on the large spread of the implemented distribution methods as previously found in figure 2.4. Smoothing spreads to nearly twice the diameter of the actuator disk for the KU Leuven and Lausanne application. Increased spread also results in a decreased uniform forcing near the disk center and thus, the forcing becomes less concentrated. The second aim concerns the discretization error as discussed in section 2.5. As stated, one method to reduce this discretization error without increasing the number of cells over the disk, is to apply grid-specific fine-tuning of the regularization kernels, ϵ . This method then assures a correct match between the intended total force and the total sum of the distributed forces, and is applied for the current application.

Equation 3.1 gives the discretized force per unit mass distributed over the grid. First, the magnitude of the force per blade element (a) is described according to equation 2.28. Then, this force is distributed by multiplication with the smoothing factor, η .

$$\left(\frac{\mathbf{F}}{\rho A}\right)_{i,j,k,a} = \left(\frac{\mathbf{F}}{\rho A}\right)_a \eta_{i,j,k,a} \quad (3.1)$$

This smoothing factor consist of two components: first an axial smoothing component, η^x , and second a radial smoothing component, η^r . Equation 3.2 defines the smoothing factor, with equations 3.3 and 3.4 defining the axial and radial components. Both smoothing components are Gaussian distributions and originally proposed by Mikkelsen (2003) [28]. Additionally, modification is applied by addition of the $(10/D_{disk})$ factor to allow for more sensible response on the relevant distance (d_i and $d_{j,k}$) for miniature wind turbines.

$$\eta_{i,j,k,a} = \eta_i^x \eta_{j,k,a}^r \quad (3.2)$$

$$\eta_i^x = \frac{1}{\epsilon_x \sqrt{\pi}} \exp \left[- \left(\frac{(10/D_{disk})d_i}{\epsilon_x} \right)^2 \right] \quad (3.3)$$

$$\eta_{j,k,a}^r = \frac{1}{\epsilon_r^3 \pi^{3/2}} \exp \left[- \left(\frac{(10/D_{disk})d_{j,k}}{\epsilon_r} \right)^2 \right] \quad \text{for} \quad a = N_a \quad (3.4)$$

Both smoothing components are based on a certain distance to the disk, for axial smoothing defined by equation 3.5 and for radial smoothing by equation 3.6, the latter is only non-zero if the cell is located outside the outer edge. Here, β is the angle between cell-center and the horizon as illustrated in figure 3.2. Also, x_{disk} , y_{disk} , z_{hub} and r_{disk} describe the location of the hub and the radius of the disk and are all global constants.

$$d_i = |x_i - x_{disk}| \quad (3.5)$$

$$d_{j,k} = \sqrt{(y_j - y_{hub} - 0.5D_{disk}\cos(\beta_{j,k}))^2 + (z_k - z_{hub} - 0.5D_{disk}\sin(\beta_{j,k}))^2} \quad (3.6)$$

The axial smoothing component is comparable with the Southampton application, while the radial smoothing component is comparable with the Lausanne application. Additionally, to give control over the minimization of the spread two input parameters are introduced: the number of upstream axial cells over which smoothing is set to occur, $N_{smooth,x}$, and the number of radial cells over which smoothing is set to occur, $N_{smooth,r}$. For example, if $N_{smooth,r}$ is set to zero radial smoothing is only present for cells within the first radial cell-distance. If $N_{smooth,r}$ is set at 5, radial smoothing occurs up to 5 cells radially removed from the actuator disk edge. Furthermore, axial smoothing only occurs upstream in order to increase the concentration of the forces.

Figure 3.1 compares the implemented distribution method with the methods from literature. Both axial and radial smoothing exhibit a smaller spread of forces than the KU Leuven and Lausanne application. The spread of axial and radial smoothing is comparable with the Southampton application, while the radial smoothing only occurs past the actuator disk edge.

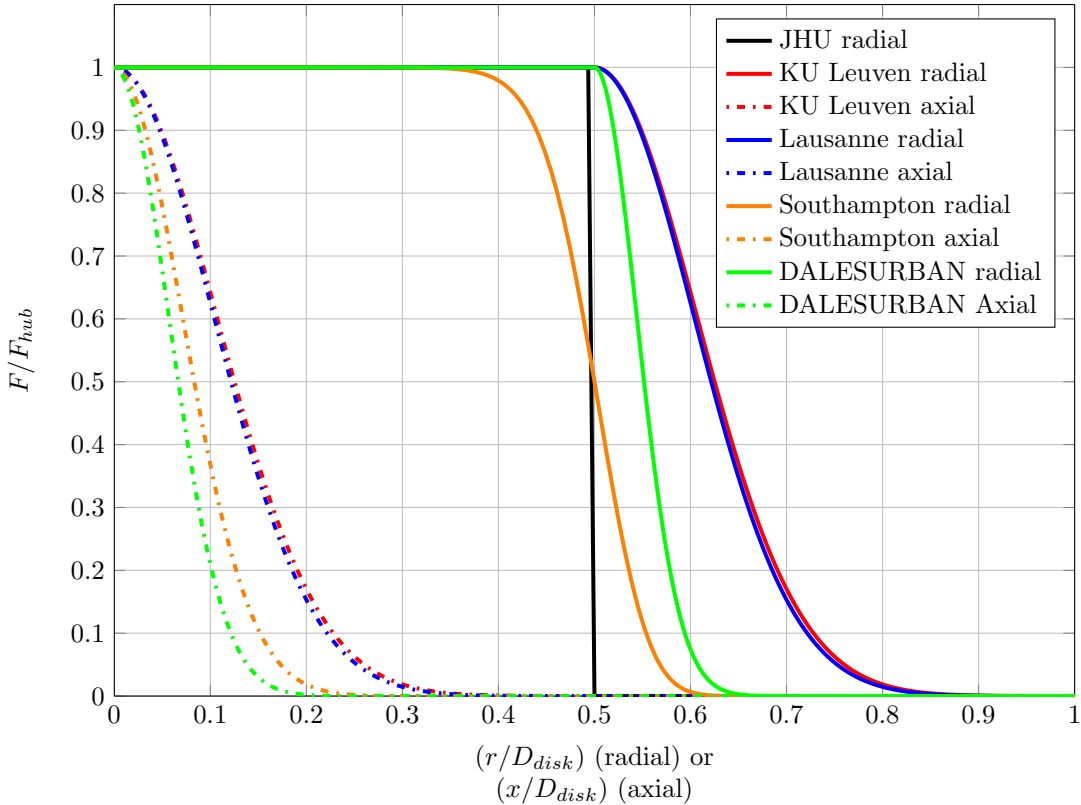


Figure 3.1: Comparing applied radial and axial smoothing with methods from literature.

3.1.3 Implementation in DALESURBAN

The DALESURBAN code as described in section 2.1 is extended with a new module specifically for the application of the wind turbine model: `modwindturbines`. The module is requested three times in the main program loop: first during the initialization of the fields, then during the definition of the additional NS terms and finally during the writing of statistics to file. Therefore, the module on itself may be separated into three main parts: imports, processing and exports. Figure 3.3 gives an overview of the position at which the new module is requested within the main program loop and summarizes the steps taken in that part of the module.

Imports

As the blade element theory discretizes the blade into separate elements, the actuator disk is separated into multiple annuli with each annulus corresponding to a certain blade element. For each blade element, inputs are the blade geometry, the smoothing factors and the area factors. The latter are used for the determination of the spatially averaged reference velocity and distribution of the inner annuli. The area factors, γ , are defined as the cell-area that overlaps the annulus over the annulus area of the blade element as given in equation 3.7.

$$\gamma_{j,k,a} = \frac{A_{overlap,j,k,a}}{A_{annulus,a}} \quad (3.7)$$

The area factors and smoothing factors are defined using a separate MatLab code and exported to DALESURBAN by text-file. For the outer annulus, smoothing is performed as previously described by equation 3.2. For all other annuli, only axial smoothing is applied according to equation 3.3, while distribution in the radial direction is based on area-factorization with an additional overall smoothing correction as stated by equation 3.8. Figure 3.2 gives an example of the distributed forces.

$$\eta_{j,k,a}^r = \gamma_{j,k,a} \cdot \frac{1}{\epsilon_r^3 \pi^{3/2}} \exp \left[- \left(\frac{0}{\epsilon_r} \right)^2 \right] \quad \text{for} \quad a < N_a \quad (3.8)$$

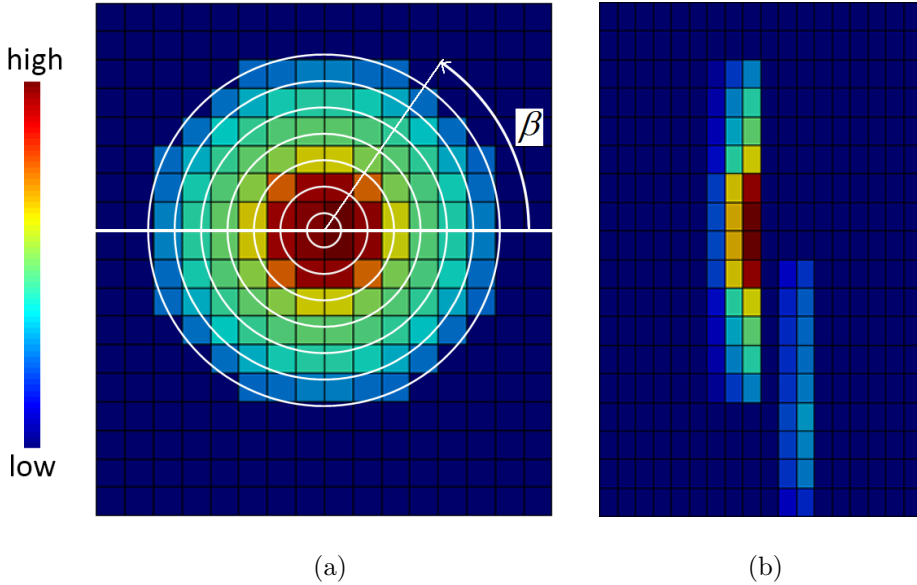


Figure 3.2: Smoothed / distributed force per unit mass. (a) Radial smoothing, white circles indicate boundaries of blade elements. (b) Axial smoothing through turbine midplane, additionally the tower and nacelle are present.

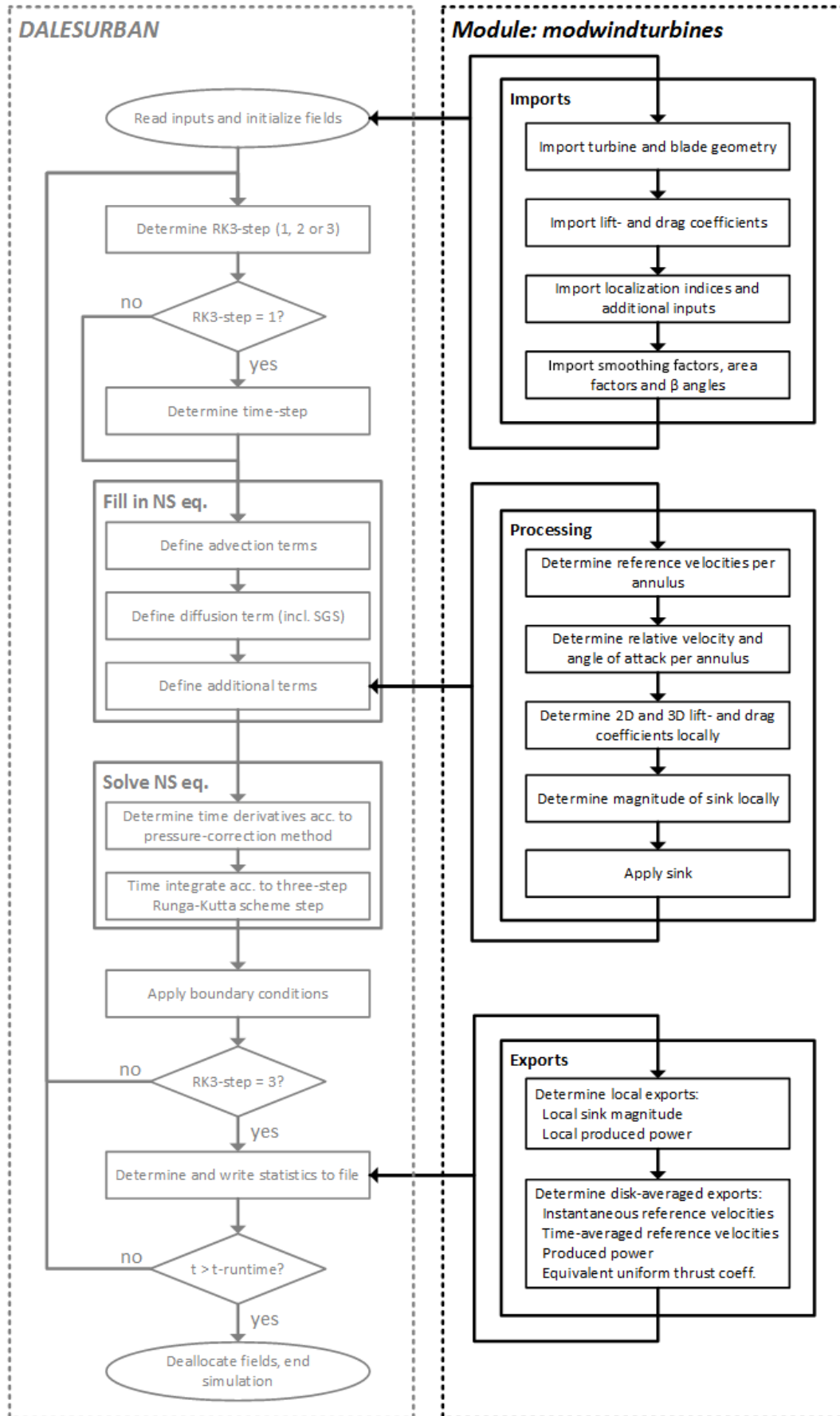


Figure 3.3: Flow chart of the NU-ADM. Showing the locations where the newly added module modwindturbines is used including the steps taken in that part of the module.

Processing

Equation 3.9 repeats the definition of the magnitude of the force per unit mass, but now explicitly for each annulus.

$$\left(\frac{\mathbf{F}}{\rho A}\right)_a = -\frac{1}{2}U_a^2 \frac{Bc_a}{2\pi r_a} (C_l \mathbf{e}_l + C_d \mathbf{e}_d) \quad (3.9)$$

To determine the relative velocity, U , three reference velocities are required for each annulus: $\langle \bar{u} \rangle_a$, $\langle \bar{v} \rangle_a$ and $\langle \bar{w} \rangle_a$. To ensure a realistic response of the wind turbine model to small-scale turbulence (small time-scale and spatial-scale), the reference velocities are time-averaged and spatially-averaged. For each reference velocity, time-averaging is performed analogously to equation 3.10 [21]. Here, the averaging time, T , is yet undefined and $\langle u \rangle_a^{n-1}$ is the annulus-averaged velocity of the previous RK3-step.

$$\langle \bar{u} \rangle_a = \frac{\Delta t_{RK}}{T} \langle u \rangle_a^{n-1} + \left(1 - \frac{\Delta t_{RK}}{T}\right) \langle \bar{u} \rangle_a^{n-1} \quad (3.10)$$

The term $\langle u \rangle_a^{n-1}$ is defined by equation 3.11. Here, the reference velocity is sampled at an imposed position upstream, set by i_{ref} .

$$\langle u \rangle_a^{n-1} = \sum_{N_y} \sum_{N_z} (u_{i_{ref},j,k}^{n-1} \gamma_{j,k,a}) \quad (3.11)$$

The resulting velocity relative to the blade, $U_{j,k,a}$, and angle of attack, α_a , are then defined by equations 3.12 and 3.14 respectively. Both are dependent on the angle of relative wind as defined by equation 3.13. The angle of relative wind is dependent on the clockwise rotational speed of the turbine and the blade tangential reference velocity. Figure 3.4 illustrates these different terms.

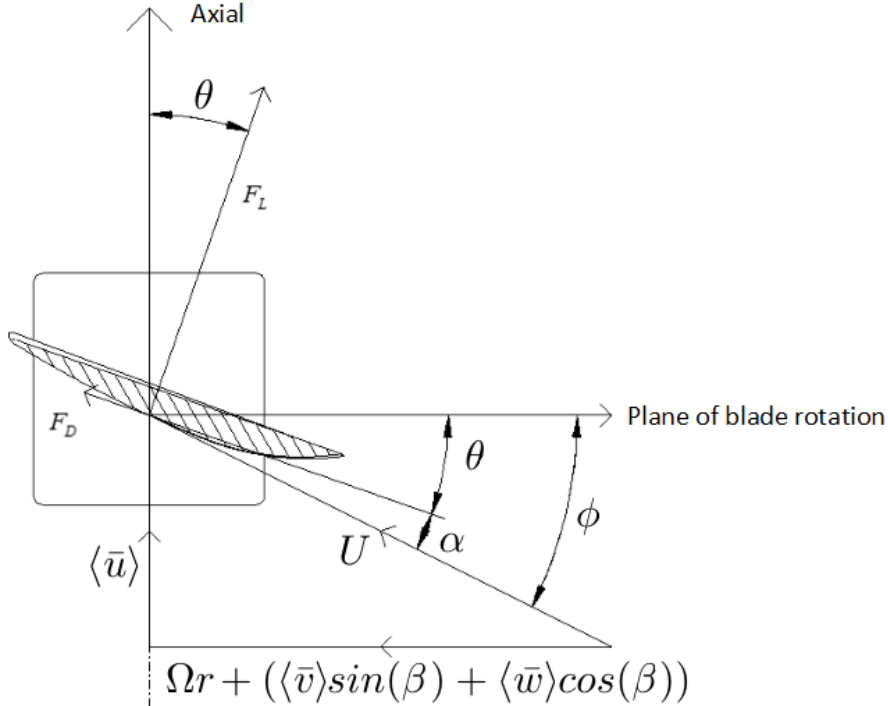


Figure 3.4: Relevant terms to define velocity relative to blade, $U_{j,k,a}$, and direction of resultant lift and drag force.

$$U_{j,k,a} = \frac{\langle \bar{u} \rangle_a}{\sin(\phi_{j,k,a})} \quad (3.12)$$

$$\phi_{j,k,a} = \arctan \left(\frac{\langle \bar{u} \rangle_a}{\Omega r_a + (\langle \bar{v} \rangle_a \sin(\beta_{j,k}) + \langle \bar{w} \rangle_a \cos(\beta_{j,k}))} \right) \quad (3.13)$$

$$\alpha_{j,k,a} = \phi_{j,k,a} - \theta_a \quad (3.14)$$

The relative velocity and angle of attack are cell dependent and thus each cell experiences a different lift- and drag coefficient. The final magnitude of the cell momentum sink is then found by substitution of equation 3.9 to equation 3.1 and equation 3.1 to equation 2.26. These substitutions are summarized in equation 3.15 and given fully discretized. Also, the two direction vectors \mathbf{e}_l and \mathbf{e}_d are readily defined.

$$\mathbf{M}_{i,j,k} = \sum^{N_a} \left(-\frac{1}{2} U_{j,k,a}^2 \frac{Bc_a}{2\pi r_a} \left(C_l \begin{bmatrix} \cos(\theta_a) \\ \sin(\theta_a) \\ \sin(\theta_a) \end{bmatrix} + C_d \begin{bmatrix} \sin(\theta_a) \\ -\cos(\theta_a) \\ -\cos(\theta_a) \end{bmatrix} \right) \eta_{i,j,k,a} \frac{1}{\Delta \mathbf{x}_{i,j,k}} \right) \quad (3.15)$$

The final distributed momentum sink is then implemented to the NS-equations by modifying the cell prediction velocity according to equation 3.16.

$$\mathbf{u}_{i,j,k}^* = \mathbf{u}_{i,j,k}^* - \mathbf{M}_{i,j,k} \Delta t_{RK} \quad (3.16)$$

Exports

Every full time-step the following disk-averaged data is exported to file for each wind turbine:

- Time [s]
- Disk-averaged streamwise ref. velocity [m/s] as defined by equation 3.17
- Disk-averaged spanwise ref. velocity [m/s] as analogously defined by equation 3.17
- Disk-averaged wall-normal ref. velocity [m/s] as analogously defined by equation 3.17
- Produced power [W] as defined by equation 3.18
- Uniform equivalent thrust coefficient C_T^{loc} as defined by equation 3.19

Additionally, equation 3.20 gives an expression for the local power coefficient, while, according to this specific definition (equation 3.20), the thrust and power coefficient are identical and thus the power coefficient is not exported separately.

$$u_{ref,disk} = \sum^{N_a} \left(\langle \bar{u} \rangle_a \frac{A_{annulus,a}}{A_{disk}} \right) \quad (3.17)$$

$$P_x = \rho \sum^{N_a} \left[\sum^{N_x} \sum^{N_y} \sum^{N_z} \left(\left(\frac{F_x}{\rho A} \right)_{i,j,k,a} u_{ref,disk} A_{cell,j,k} \right) \right] \quad (3.18)$$

$$C_T^{loc} = \sum^{N_a} \left[\sum^{N_x} \sum^{N_y} \sum^{N_z} \left(\left(\frac{F_x}{\rho A} \right)_{i,j,k,a} A_{cell,j,k} \right) \right] \frac{1}{\frac{1}{2} u_{ref,disk}^2 \cdot A_{disk}} \quad (3.19)$$

$$C_P = \frac{P_x}{\frac{1}{2} \rho u_{ref,disk}^3 \cdot A_{disk}} \quad (3.20)$$

Modeling of tower and nacelle

For the tower the streamwise drag is considered and the applied force per unit mass is defined by equation 3.21. Here, the reference velocity, $u_{tower,i,j,k}$, is instantaneous and cell-local.

$$\left(\frac{F_{tower}}{\rho A} \right) = -\frac{1}{2} u_{tower,i,j,k}^2 C_{d,tower} \quad (3.21)$$

The tower force per unit mass is again smoothed over the grid by application of a smoothing factor, η^{tower} . This smoothing factor is the product of two components: axial smoothing and spanwise smoothing. Both components are defined analogously to equation 3.3. For axial smoothing, the distance d_i is defined by equation 3.22. For spanwise smoothing, the distance d_j as defined by equation 3.23 holds. Here, d_j is substituted in equation 3.3 for d_i . Equation 3.24 gives the distributed momentum sink for the tower drag.

$$d_i = |x_i - x_{tower}| \quad (3.22)$$

$$d_j = |y_j - y_{hub} \pm 0.5D_{tower}| \quad (- \text{ if } y_j < y_{hub} \quad \text{and} \quad + \text{ if } y_j > y_{hub}) \quad (3.23)$$

$$M_{tower,i,j,k} = \left(\frac{F_{tower}}{\rho A} \right) \eta_{i,j,k}^{tower} \frac{1}{\Delta x_i} \quad (3.24)$$

The nacelle is located at the center of the disk as illustrated by figure 3.2. For the nacelle, the force per unit mass is defined by equation 3.25 and the resulting applied momentum sink term by equation 3.26.

$$\left(\frac{F_{nacelle}}{\rho A} \right) = -\frac{1}{2} u_{nacelle}^2 C_{d,nacelle} \quad (3.25)$$

$$M_{nacelle,i,j,k} = \left(\frac{F_{nacelle}}{\rho A} \right) \eta_{i,j,k}^{nacelle} \frac{1}{\Delta x_i} \quad (3.26)$$

The nacelle's momentum sink is distributed in axial direction by the same axial smoothing factor as applied for the actuator disk, equation 3.3. Radially, the nacelle is distributed area-factorization based. See equation 3.27 for the definition of the area-factors for the nacelle and equation 3.28 for the definition of $\eta_{i,j,k}^{nacelle}$. The reference velocity for the nacelle, $u_{nacelle}$, is taken as the streamwise reference velocity of the most inner annulus, $\langle \bar{u} \rangle_1$. Both tower and nacelle drag coefficients are model inputs considered constant.

$$\gamma_{nacelle,j,k} = \frac{A_{cell,j,k} - \gamma_{j,k,1} A_{cell,j,k}}{0.25\pi D_{nacelle}^2} \quad (3.27)$$

$$\eta_{i,j,k}^{nacelle} = \eta_i^x \gamma_{nacelle,jk} \quad (3.28)$$

3.2 Methodology for model verification and validation

Figure 3.5 gives the followed methodology for wind turbine model development. The model inputs are divided into two categories: the known inputs and the unknown inputs. The known inputs are either known or estimated from the validation case. The unknown inputs cannot be defined without parameter estimation. For this, the sensitivity of the model to a certain input and its induced uncertainty is assessed. Examples of unknown inputs are model specifics, such as the spatial and temporal discretization and non-physical inputs such as subgrid constants. Finally, the model's uncertainty is quantified and full model verification and validation is applied.

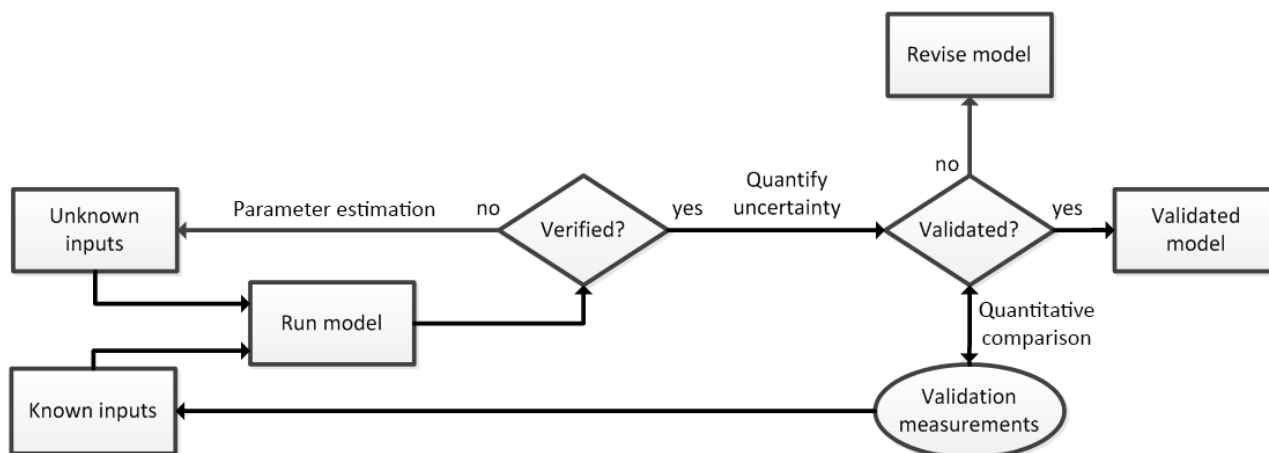


Figure 3.5: Followed methodology for model parametrization and uncertainty quantification with regards to verification and subquential validation.

The process of verification consist of two steps: code verification and calculation verification [38]. The purpose of code verification is to confirm that the software is working as intended and the main focus is to identify and eliminate programming and implementation errors. The purpose of calculation verification is to quantify the error of numerical simulation by demonstration of convergence of the model and, if possible, to provide an estimation of the numerical errors induced by the use of the model. Furthermore, model validation is the process of determining the degree to which a model is an accurate representation of the real world from the perspective of the intended uses of the model. [38]. The validation case is chosen from literature to omit the need of performing a new experiment. For the validation case, the following requirements are set:

- A multitude of turbines in a streamwise aligned arrangement, which experience fully developed flow conditions.
- Actual turbines, no model simplifications such as semi-permeable surfaces, i.e. gauzes.
- Detailed geometric specifications.
- Constant flow direction perpendicular to turbines and aligned with column of turbines.
- Measurements within a neutrally stratified boundary layer, preferably approaching half-channel flow simplification.
- Detailed measurements: time-averaged flow fields and profiles of streamwise velocity and Reynolds stresses.

3.3 Wind turbine model validation case

The measurements performed by Chamorro and Porté -Agel [5] fit stated validation case requirements. Measurements are presented in appendix C. Figure 3.6 gives a graphical representation of the measurement setup. A total of 30 turbines are placed: 10 in a column and 3 on each row. Here, the last 3 to 4 turbines seem to approach infinite wind farm conditions; time-averaged flow and turbulence profiles remain approximately identical while the relative rotational speed of the turbines has approached an asymptote. The distance between turbines is five turbine diameters streamwise (S_x) and four turbine diameters spanwise (S_y). All turbines are fitted with a GWS/EP-6030x3 propeller with a diameter of about 15cm, more detail on this propeller and its blades is presented in appendix D.1. The hub-height is 12.5cm. Figure 3.7 gives more detail on the miniature wind turbines.

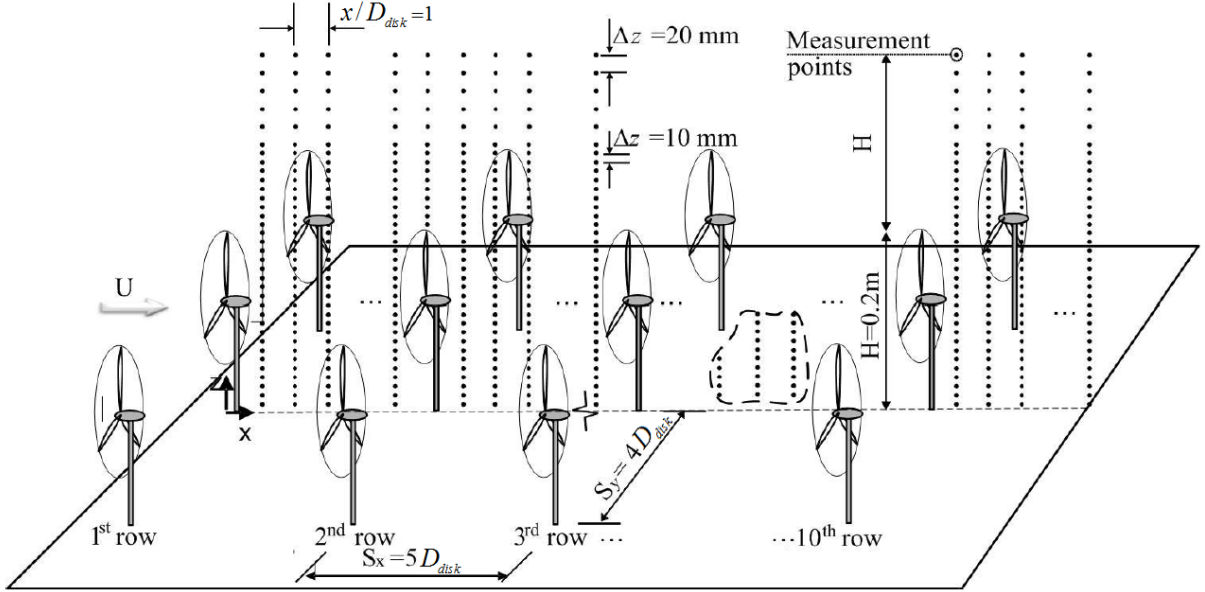


Figure 3.6: Schematic of wind turbine array for validation measurements (modified from [5]).

All measurements are performed based on a neutrally stratified inflow profile as defined by table 3.1. Measurements are performed on the midplane of the middle row of a 10x3 miniature wind turbine array, as shown in figures 3.6 and 3.7. Data are given for the time-averaged flow fields of the streamwise velocity and $\overline{u'u'}$ Reynolds stress in the turbine midplane. Furthermore, the streamwise flow profiles at specific distances behind the turbines and the average rotational speed of the turbines in a column are given, see appendix C.

Table 3.1: Specification of inflow profile as applied in the validation measurements [31].

Attribute	Symbol	Value	Unit
Shear velocity	u_τ	0.12	m/s
Roughness length	z_0	3.0×10^{-5}	m
Boundary layer height	δ	0.68	m
Reynolds number	Re_δ	14.5×10^3	–

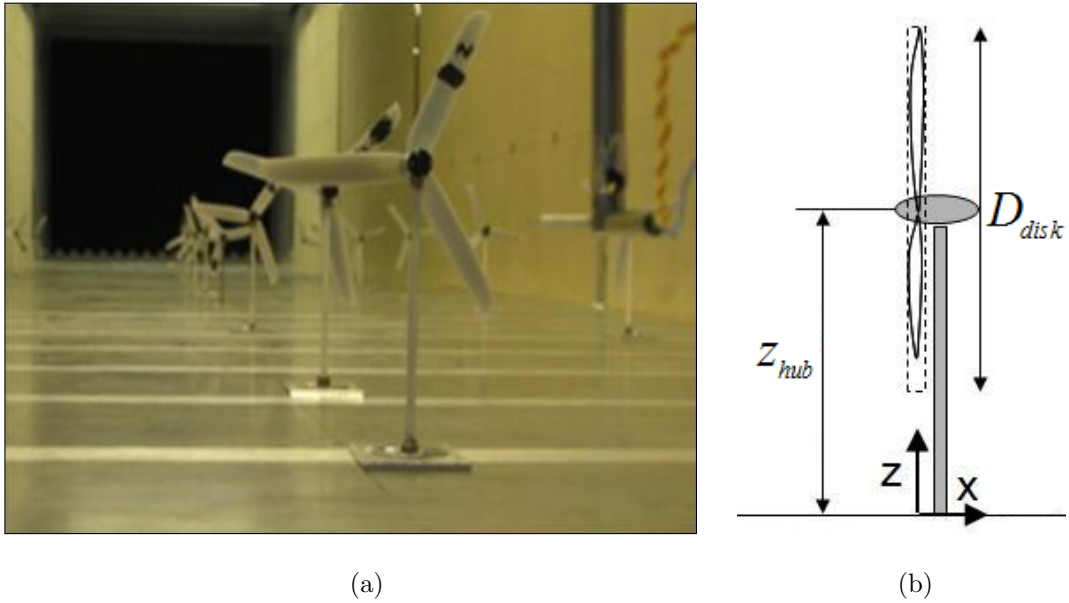


Figure 3.7: (a) Overview of wind turbine array for validation measurements. (b) Schematic of a single wind turbine used for validation measurements within the wind turbine array (modified from [5]).

3.4 Simulation set-up

With respect to the research question, all simulations are performed for an infinite wind farm. The infinite wind farm is a theoretical approach for which the following statements are considered true [4], [18]:

- Boundary layer flow approaches fully developed regime.
- The power output is only governed by the rate at which the ABL replenishes energy.

In practice, wind farms exceeding horizontal extents of 10 to 20km may approach these statements. With the current development of large offshore wind farm, such theoretical approach becomes more realistic [12]. For example, the current largest off-shore wind farm, London Array, is built over a total surface area of 100km^2 [10]. However, not only size is a restriction for infinite wind farms. Other restrictions such as a flat terrain and a minimal difference in surface roughness should be noted. The main reason the infinite wind farm approach is considered in a large number of wind farm studies is its practicality regarding academic and engineering exercises. The approach allows for the application of streamwise and spanwise periodicity, useful for both analytic and numeric wind farm solutions.

As the scales of the largest eddies are limited by the size of the computational domain, it is important to define the requirements for a proper infinite wind farm simulation. The smallest infinite domain imaginable is based around a single wind turbine and limited in size by the streamwise and spanwise spacing between turbines within the considered wind farm. Such a domain is hereby defined as the single domain. This smallest infinite domain is however not capable of resolving the larger scale eddies occurring within a wind farm. Therefore, only time-averaged results are considered for the single domain. In order to prevent contamination of the flow by periodic boundary conditions, to allow analysis of instantaneous results and to model large scale wind farm phenomena, a larger infinite (double-periodic) domain is required for applications such as wind farms with alternating tower heights.

Initially, to optimize the efficiency of parameter estimation, verification and validation of the wind turbine model, the smallest imaginable infinite domain is applied: the single domain. Final work on alternating tower height wind farms is performed for an infinite domain constructed from a multitude of these single domains. This choice is made to suppress the need for any redefinition and re-estimation of inputs and parameters. First, for the single domain all known and unknown wind turbine model inputs and its model uncertainty is quantified. Then, the infinite domain is defined and its model uncertainty quantified.

3.4.1 The single domain

Table 3.2 gives all known model inputs and, if applicable, refers to appendices describing how the input is found. Some inputs are chosen and estimated as weakly-sensitive. No further sensitivity study is performed on these inputs as the model is not expected significantly sensitive. Furthermore, table 3.3 gives all unknown inputs. Appendix E gives a comprehensive description of how these inputs are estimated.

The length and width of the domain is the result of the configuration of the wind turbines in the validation case. Introduction of wind turbines within an undisturbed boundary layer results in a growth of boundary layer height. Johnstone and Coleman (2012) state a 45% increase from the undisturbed height for an infinite wind farm in a turbulent neutral Ekman boundary layer [18]. Based on the specification of the inflow profile as found in table 3.1, the model boundary layer is set at $1m$ accordingly. The position of the wind turbine, x_{hub} and y_{hub} , is freely chosen and the simulation results are considered non-sensitive due to domain periodicity. Figure 3.8 gives a graphical representation of the single domain. The nacelle drag coefficient is chosen high to ensure no bypass of flow from the disk through disk center. The drag coefficient of the tower is estimated according to the drag of a flow around a cylinder at high Reynolds number [1]. Lastly, the nacelle's diameter and the tower's diameter and x-position are unknown from the validation case and have been estimated from figure 3.7.

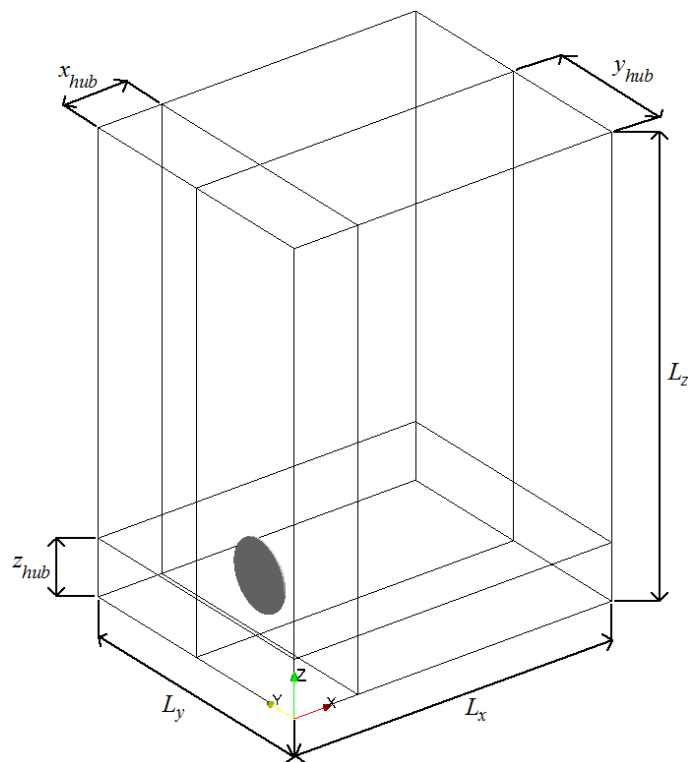


Figure 3.8: Dimensions of single domain and position of the turbine.

Table 3.2: Known wind turbine model inputs for the single domain.

Input	Symbol	Value	Unit	Source
Domain length	L_x	0.75	m	$S_x = 5D_{disk}$ [5]
Domain width	L_y	0.6	m	$S_y = 4D_{disk}$ [5]
Domain height	L_z	1.0	m	Table 3.1 + BL growth
x-position disk	x_{hub}	0.15	m	Chosen (non-sensitive)
y-position disk	y_{hub}	0.3	m	Chosen (non-sensitive)
Hub-height	z_{hub}	0.125	m	Validation [5]
x-position tower	x_{tower}	0.17	m	Chosen (weakly-sensitive)
Disk diameter	D_{disk}	0.154	m	Validation [5]
Tower diameter	D_{tower}	0.01	m	Chosen (weakly-sensitive)
Nacelle diameter	$D_{nacelle}$	0.015	m	Chosen (weakly-sensitive)
Nacelle drag coef.	$C_{d,nacelle}$	1	–	Chosen (weakly-sensitive)
Tower drag coef.	$C_{d,tower}$	0.5	–	Chosen (weakly-sensitive)
Number of blades	B	3	–	Appendix D.1
Annuli per number of disk cells	$N_a/N_{cells,disk}$	1/2	–	Appendix D.1
Blade element radius	r_a	Variable	m	Appendix D.1
Blade element chord	c_a	Variable	m	Appendix D.1
Blade element pitch	θ_a	Variable	deg	Appendix D.1
Lift coef.	C_l	Variable	–	Appendix D.2
Drag coef.	C_d	Variable	–	Appendix D.2
Rotational speed	Ω	Variable	rad/s	Appendix D.3
Viscosity	ν	1.41×10^{-5}	m^2/s	Physical constant

Table 3.3: Unknown wind turbine model inputs that require parameter estimation, see appendix E.

Input	Symbol	Value	Unit	Estimated in
Convergence time	t_{conv}	100	s	Appendix E.2
Statistical avg. period	$T_{stat,avg}$	1000	s	Appendix E.2
Reference avg. time	T	1	s	Appendix E.2
Time step	Δt	2.5×10^{-3}	s	Appendix E.2
Number of x-cells	N_x	96	–	Appendix E.1
Number of y-cells	N_y	48	–	Appendix E.1
Number of z-cells	N_z	48	–	Appendix E.1

Radial kernel	ϵ_r	0.62	–	Appendix E.1
Axial kernel	ϵ_x	0.8	–	Appendix E.1
Radial smoothing width	$N_{smooth,r}$	0	–	Appendix E.1
Axial smoothing width	$N_{smooth,x}$	2	–	Appendix E.1
Subgrid model	<i>SGM</i>	Vreman	–	Appendix E.3
Subgrid constant	C_v	0.07	–	Appendix E.3

Single domain model uncertainty

Appendix E.2 discusses the statistical averaging period, $T_{stat,avg}$, and estimates the sampling error of the performance measures of the wind turbine within the single domain. The sampling error as a result of the imposed statistical averaging period is summarized in table 3.4. For example, these errors are of relevance when comparing cases for which the solution is found by application of the model. In such situation it is necessary to know when differences between model results are significant and not the result of model uncertainties.

Additionally, the temporal and spatial discretization errors are assessed in appendix E. Temporal discretization errors are found to be negligible. A supported spatial discretization error could not be determined due to difficulty in obtaining grid convergence. However, the sensitivity of the performance measures to grid refinement was found to be minimal: <2%. Practically, this implies that any significant difference (>3%) between the model and the validation case is most likely not the result of discretization errors.

Table 3.4: Summary of quantified uncertainties.

Uncertainty	E_{P_x} [%]	$E_{\bar{u}_{ref,disk}}$ [%]	E_{C_p} [%]
Statistical avg. period	0.37	0.14	0.03

3.4.2 The infinite domain

For the infinite domain, the number of single domains (or turbines) in a column, N_{column} , and the number of single domains (or turbines) in a row, N_{row} , have to be determined. Also, all model inputs are as stated for the single domain with the exception of the convergence time and statistical averaging period. Due to a larger number of turbines, the statistical averaging period of the combined results (of all turbines within the domain) exhibit a different sampling error. Therefore, the statistical averaging period is reassessed.

To determine the number of turbines in the infinite domain, cross-correlations between the disk-averaged reference velocities: $u_{ref,disk}$, $v_{ref,disk}$ and $w_{ref,disk}$, are investigated. See appendix F for details. Table 3.5 summarizes the resulting number of columns and rows in the infinite domain. Figure 3.9 gives a graphical representation of the resulting domain.

Table 3.5: Number of columns and rows in the infinite domain.

Input	Symbol	Value	Unit	Estimated in
Number of columns	N_{column}	6	-	Appendix F
Number of rows	N_{row}	12	-	Appendix F

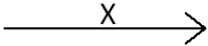
col												
6	61	62	63	64	65	66	67	68	69	70	71	72
5	49	50	51	52	53	54	55	56	57	58	59	60
4	37	38	39	40	41	42	43	44	45	46	47	48
3	25	26	27	28	29	30	31	32	33	34	35	36
2	13	14	15	16	17	18	19	20	21	22	23	24
1	1	2	3	4	5	6	7	8	9	10	11	12
row	1	2	3	4	5	6	7	8	9	10	11	12

Figure 3.9: Numbering of turbines for the second domain, row numbers and column numbers under row and col respectively.

Infinite domain temporal parameters and model uncertainty

In appendix F.2, the temporal parameters of the infinite domain are determined, as summarized in table 3.6. The temporal parameters of the infinite domain differ from the single domain. Most noticeably, the statistical averaging period is about 70% shorter than found for the single domain. It is found that time-averaged performance measures of all 72 turbines combined, exhibit a lower sampling error. Table 3.7 summarizes the resulting sampling error.

Table 3.6: Summary of estimation of all temporal parameters for the infinite domain

Input	Symbol	Value	Unit
Convergence time	t_{conv}	200	s
Statistical avg. period	$T_{stat,avg}$	300	s

Table 3.7: Summary of quantified uncertainties of all 72 turbines combined.

Uncertainty	$E_{\bar{P}_x}$ [%]	$E_{\bar{u}_{ref,disk}}$ [%]	$E_{\bar{C}_p}$ [%]
Statistical avg. period	0.49	0.22	0.02

3.4.3 Boundary conditions and initial conditions

Boundary conditions for all vertical domain walls are periodic as required for the aim of an infinite wind farm. Top and bottom boundary conditions are further detailed.

Top boundary condition

For the top, the boundary conditions stated by equations 3.29, 3.30, 3.31 and 3.32 hold (free slip).

$$\frac{\partial u}{\partial z} = 0 \quad (3.29) \quad \frac{\partial v}{\partial z} = 0 \quad (3.30)$$

$$w = 0 \quad (3.31) \quad \frac{\partial \nu_e}{\partial z} = 0 \quad (3.32)$$

Bottom boundary condition and wall-function

Bottom boundary conditions are no-slip wall, with a wall-function to suppress the need for a computationally expensive resolved grid near the wall. For the wall-normal velocity, equation 3.31 holds. The wall shear stress is computed by the Werner and Wengle [42] wall function. This wall function is valid for hydraulically smooth flows and assumes a linear-law-of-the-wall description (equation 3.33) for the wall-shear stress for $z^+ < (z_m = 11.81)$, with z_m the upper boundary of validity of the linear-law-of-the-wall. For $z^+ > z_m$, the wall function becomes a power-law description (equation 3.34)[42], yet different from the more commonly used logarithmic-law-of-the-wall. One advantage of the Werner and Wengle wall function is its ability to determine the shear without the need of iteration.

$$\frac{\tau}{\rho} = \frac{2\nu|u_{\parallel}|}{\Delta z} \quad (3.33)$$

$$\frac{\tau}{\rho} = \left[\frac{1-B}{2} A^{\frac{1+B}{1-B}} \left(\frac{\nu}{\Delta z} \right)^{1+B} + \frac{1+B}{A} \left(\frac{\nu}{\Delta z} \right)^B |u_{\parallel}| \right]^{\frac{2}{1+B}} \quad (3.34)$$

In equations 3.33 and 3.34, $|u_{\parallel}|$ is the wall parallel reference velocity, either streamwise or spanwise depending on calculated wall shear direction. Furthermore, A and B are constants with values 8.3 and 1.7, respectively. Based on the validation inflow conditions (undisturbed) as summarized in table 3.1, the flow near the wall is checked on hydraulical smoothness. The influence of wall roughness is expressed as a roughness Reynolds number, as defined by equation 3.35. For flows with $Re_{z_0} < 5$, hydraulic smoothness holds [43]. Application of the wind turbine model is expected to reduce the friction velocity near the wall, therefore, the flow is also expected to be hydraulically smooth with application of the wind turbine model.

$$Re_{z_0} = \frac{u_{\tau} z_0}{\nu} = 0.26 \quad (3.35)$$

Initial conditions

Table 3.8 gives an overview of initial conditions. All initial velocities are set spatially constant over the whole domain. The streamwise velocity is set such that the bulk velocity corresponds with the bulk velocity of the undisturbed boundary layer flow as previously defined in table 3.1.

Table 3.8: Initial conditions.

Attribute	Symbol	Value	Unit
Streamwise velocity	u	3	m/s
Spanwise velocity	v	0	m/s
Wall-normal velocity	w	0	m/s

3.4.4 Model driving force

For infinite domains, a driving force is required. In DALESURBAN the driving force is set as a pressure difference per unit length. To determine this driving force, the force balance of the model is determined. This balance can be determined by taking the domain volume integral of the converged time-averaged filtered Navier-Stokes equations. The filtered Navier-Stokes equations as applied in DALESURBAN were given by equation 2.5. Assuming convergence and applying time-averaging gives equation 3.36

$$\underbrace{\frac{\partial u_i}{\partial t}}_{=0} + \frac{\partial u_i u_j}{\partial x_j} = -\frac{\partial p_{mod}}{\partial x_i} + \frac{\partial}{\partial x_j} ((2\nu + \nu_e) S_{ij}) + \overline{M_{body}} \quad (3.36)$$

Here, M_{body} only consists of the momentum sink as imposed by the turbine, the nacelle and the tower. The streamwise force balance is then found by taking the volume integral of the streamwise component of equation 3.36. Solving this integral by application of the divergence theorem for volume integrals, results in the force balance as given by equation 3.37. Here, N_{wt} is the number of turbines in the domain. Note that this force balance is only valid for steady-state double-periodic domains with free-slip conditions for the top boundary.

$$\overline{\Delta p_{mod}} L_y L_z = \frac{1}{\rho} \sum^{N_{wt}} \overline{F_x} + (\nu + \nu_e(z=0)) \frac{\partial u}{\partial z}(z=0) L_x L_y \quad (3.37)$$

The eddy viscosity approaches zero infinitely close to a wall. Therefore, the viscous term from equation 3.37 may be rewritten to τ_x as found by application of the wall function. Reordering of terms results in equation 3.38 for the force balance. Here, the term $[\overline{\Delta p_{mod}}/L_x]$ is the pressure difference per unit length as required in DALESURBAN. Equation 3.38 can be further simplified to equation 3.39. Here, the RHS is defined as the friction velocity as commonly applied for boundary layer flows.

$$\left[\frac{\overline{\Delta p_{mod}}}{L_x} \right] L_z = \frac{1}{\rho} \left(\sum^{N_{wt}} \overline{F_x} + \overline{\tau_x} \right) \quad (3.38)$$

$$\left[\frac{\overline{\Delta p_{mod}}}{L_x} \right] L_z = u_\tau^2 \quad (3.39)$$

From equation 3.39, the importance of the set driving force on the final results is clear. For the validation inflow profile without turbines, table 3.1 gave $u_\tau^2 = 1.44 \times 10^{-2} m^2/s^2$. Application of a turbine within the same flow, results in an increase of total force on the flow. In order to match validation results it is found to be necessary to increase the pressure difference compared to the undisturbed flow. Table 3.9 gives the resulting pressure difference found by trial-and-error of matching simulation results with validation measurements.

Table 3.9: Definition of model driving force for all domains.

Input	Symbol	Value	Unit
Driving force times unit height	$\Delta(p/L_x)L_z$	0.04895	m^2/s^2

Additionally, in the current study various time related results (such as power production time-series) are presented scaled by a time-scale, δ/u_τ . This time-scale is defined according to equation 3.40 as a direct result of equation 3.39.

$$\left(\frac{\delta}{u_\tau} \right) = L_z \left(\sqrt{\frac{\overline{\Delta p_{mod}} L_z}{L_x}} \right)^{-1} \quad (3.40)$$

Chapter 4

Model verification and validation

The implemented wind turbine model is verified and validated. First, code verification is performed. Then, the calculation is verified by comparison to engineering wake solutions and Frandsen’s double-log-law theory. Lastly, the model is validated by measurements as previously introduced by the validation case, section 3.3. In line with the validation case, the domain height is set as 0.89 m [31] for all verification and validation runs only.

4.1 Code verification

The code is verified by comparing the model result with the analytic result. First, the analytic result is found for a spatially constant fixed known reference velocity: $u_{ref} = 2\text{m/s}$. Then, the model is run for one time-step, initialized by a spatially constant streamwise velocity of the same magnitude. For the analytic result, the power production is determined according to equation 4.1. Here, the force per unit mass for each blade element (annulus) is analytically defined according to equation 3.9.

$$P_{analytic} = \rho \sum_a^{N_a} \left(\frac{F_x}{\rho A} \right)_a A_{annulus,a} u_{ref} \quad (4.1)$$

For the model, the distribution of the total force is fine-tuned via the smoothing regularization kernels, ϵ_x and ϵ_r , upto an error of one ten-thousandth of a percent compared with the analytic solution. This high accuracy of fine-tuning is applied to eliminate the force distribution as a source of the resultant code error. For each blade element it is found that the relative velocity, U_a , lift coefficient and drag coefficient match with the analytic results by less than 0.01% error. Table 4.1 gives the error between the analytically defined power production, $P_{analytic}$, and the resulting power production as found by the model. Also, the code errors of the tower and nacelle are assessed in a similar manner and given in table 4.1.

Table 4.1: Overview of code errors.

	P_x	F_{tower}	$F_{nacelle}$
$E_{code} [\%]$	< 0.01	< 0.01	< 0.01

The results from table 4.1 support the following statements:

- The code error of the wind turbine model, tower and nacelle is negligible.
- Any remaining errors in the code (if any) have a negligible influence on results.
- The discretization error between continuous smoothing and discretized smoothing as discussed in section 2.5 is indeed mitigated by the distribution method, see section 3.1.2.

4.2 Calculation verification by engineering wake solutions

The NU-ADM is compared with two engineering wake solutions: the Risø WAsP model (Jensen's wake model) and the Risø analytic model.

The Risø WAsP model contains a simple wake model based on linear expansion of the wake downstream [3] and is developed for a single wind turbine. The wake velocity behind the turbine is determined according to equation 4.2. Here, k_{wake} is the wake decay constant set to 0.075 as suggested for onshore conditions.

$$u_{wake}(x) = u_{hub} \left[1 - (1 - \sqrt{1 - C_T^{loc}}) \left(\frac{D_{disk}}{D_{disk} + 2k_{wake}x} \right)^2 \right] \quad (4.2)$$

For the Risø analytic model the wake velocity behind the turbine is calculated according to equation 4.3 [3]. Here, the term A_0/A_{wake} is the swept area of the rotor over the area of the wake. The expansion of the area of the wake prior to impacting the ground, is given by equation 4.4 [3]. Here, the term β is given by equation 4.6. For α , equation 4.5 is used specifically developed for application of an infinite row of turbines [15]. Here, the term R_t is known as the turbine reduction factor and defined by equation 4.7 as the resulting hub velocity, u_{hub} , over undisturbed hub velocity, $u_{0,hub}$.

$$u_{wake}(x) = \frac{1}{2} u_{hub} + \sqrt{|0.25 - 0.5 u_{hub}^2 \frac{A_0}{A_{wake}} \frac{1}{C_T^{loc}}|} \quad (4.3)$$

$$\frac{D_{wake}}{D_0} = \frac{1}{(\beta^{3/2} + \alpha(x/D_{disk}))^{1/3}} \quad (4.4)$$

$$\alpha = \frac{1}{2} \frac{C_T^{loc}}{s_r} \frac{R_t}{1 - R_t} \quad (4.5)$$

$$\beta = \frac{1}{2} \frac{1 + \sqrt{1 - C_T^{loc}}}{\sqrt{1 - C_T^{loc}}} \quad (4.6)$$

$$R_t = \frac{u_{hub}}{u_{0,hub}} \quad (4.7)$$

Figure 4.1 compares the wake velocity of the analytic engineering solutions, with the disk averaged and time-averaged streamwise velocity of the NU-ADM as function of the normalized distance behind the turbine. A satisfying match with the Risø analytic model is found. Comparison with the WAsP model is however not as satisfying. Furthermore, for an infinite row of turbines to be in balance with the boundary layer flow, the engineering solutions should return to set hub velocity. This is only true for the Risø analytic model, specifically modified for such application [15]. Barthelmie (2006) performed a similar analysis for a single wind turbine, and found that engineering wake solutions tend towards either a high or low prediction with an average mean absolute error of 15% [3]. Therefore, performing calculation verification by engineering wake solutions is inconclusive.

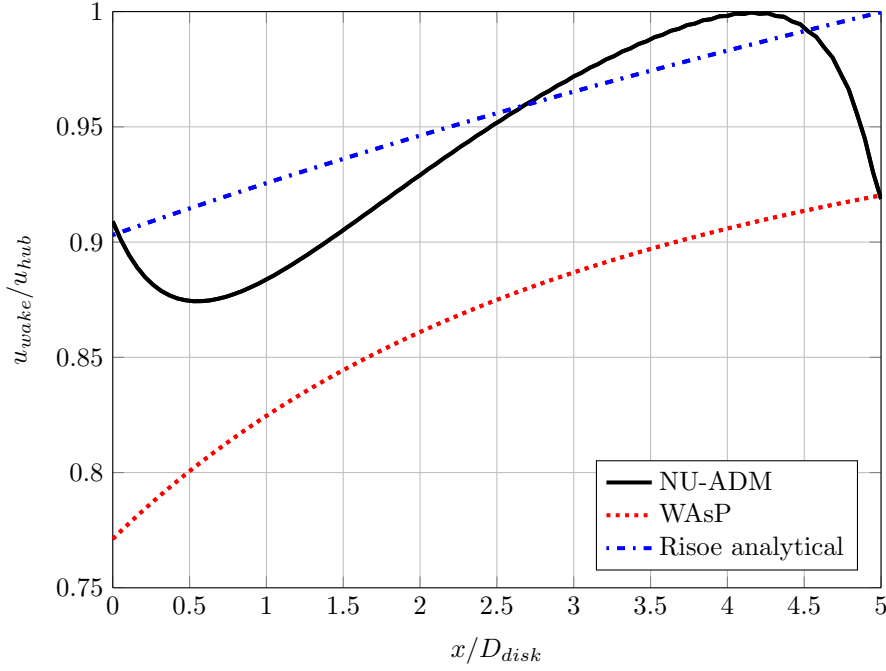


Figure 4.1: Comparison of engineering wake solutions with the NU-ADM.

4.3 Calculation verification by Frandsen’s double-log-law theory

The time and slab-averaged streamwise velocity profile of the NU-ADM is compared with the double-log-law theory. This theory considers the vertical change in the atmospheric boundary layer due to the increase in the surface roughness induced by a cluster of a large number of wind turbines [4]. The theory is originally developed by Frandsen [14], [15], while the equations shown below follow the description by Calaf (2010) [4]. The double-log-law theory models the resulting flow profile as two log layers: one below turbine hub-height, equation 4.8, and one above turbine hub-height, equation 4.9. Figure 4.2 gives a graphical representation of the two log layers and all introduced variables.

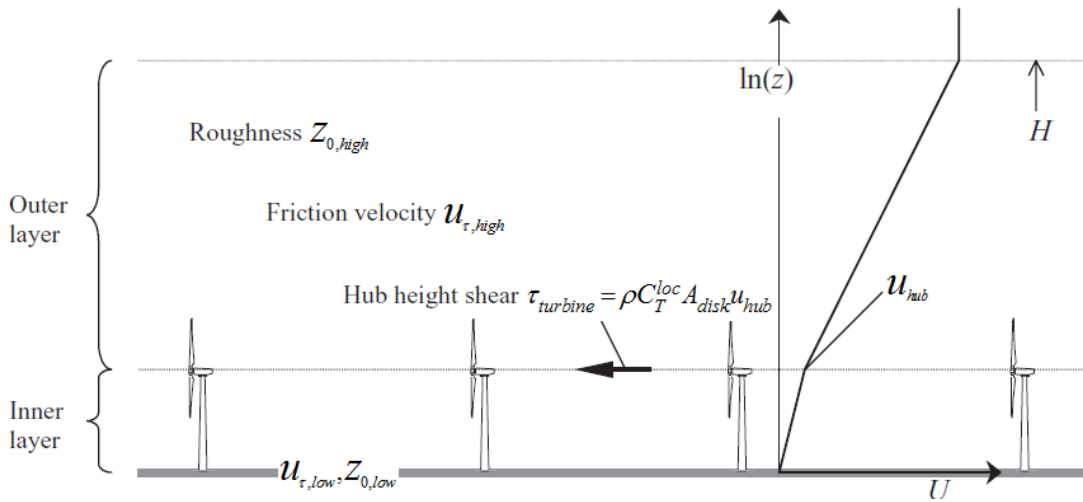


Figure 4.2: Terms and variables for the double-log-law theory (modified from [15].)

$$\langle \bar{u} \rangle_{low}(z) = \frac{u_{\tau,low}}{\kappa} \ln \left(\frac{z}{z_{0,low}} \right) \quad \text{for} \quad z_{0,low} < z \leq z_{hub} \quad (4.8)$$

$$\langle \bar{u} \rangle_{high}(z) = \frac{u_{\tau,high}}{\kappa} \ln \left(\frac{z}{z_{0,high}} \right) \quad \text{for} \quad z \geq z_{hub} \quad (4.9)$$

Both log layers depend on a characteristic friction velocity and roughness. For equation 4.8, $z_{0,low}$ is the roughness length of the wall as defined in table 3.1 and $u_{\tau,low}$ is defined by equation 4.10. Here, $\kappa = 0.41$ and is known as the von Kármán constant. For equation 4.9, $z_{0,high}$ is defined by equation 4.11 and $u_{\tau,high}$ is found by solving the sum of the total shear, equation 4.12, for $u_{\tau,high}$.

$$u_{\tau,low} = \frac{R_t \kappa u_{0,hub}}{\ln \left(\frac{z_{hub}}{z_{0,low}} \right)} \quad (4.10)$$

$$z_{0,high} = z_{hub} \exp \left(- \frac{\kappa}{\sqrt{\frac{1}{2} c_{ft} + \left[\frac{\kappa}{\ln(z_{hub}/z_{0,low})} \right]^2}} \right) \quad (4.11)$$

$$u_{\tau,high}^2 = u_{\tau,low}^2 + \frac{1}{2} C_T^{loc} \frac{A_{disk}}{L_x L_y} \left(\frac{1}{\kappa} \ln \frac{z_{hub}}{z_{0,high}} \right)^2 u_{\tau,high}^2 \quad (4.12)$$

Equation 4.12 can be simplified to equation 4.13 by definition of the turbine friction coefficient, c_{ft} as defined by equation 4.14.

$$u_{\tau,high}^2 = u_{\tau,low}^2 + \frac{1}{2} c_{ft} \left(\frac{1}{\kappa} \ln \frac{z_{hub}}{z_{0,high}} \right)^2 u_{\tau,high}^2 \quad (4.13)$$

$$c_{ft} = \frac{C_T^{loc} A_{disk}}{L_x L_y} \quad (4.14)$$

Figure 4.3 gives the time and slab averaged streamwise velocity profiles of the NU-ADM and the double-log-law theory. Differences are significant and the simulation result of the NU-ADM overestimates the double-log-law velocity profile. Largest differences are found in the outer region of the upper log-profile. For the outer region of any undisturbed boundary layer flow driven by a pressure difference, the velocity profile is known to deviate from the common log-law description according to the law of the wake [30]. In order to improve the NU-ADM's match with the double-log-law theory, equation 4.9 is modified by application of Coles' wake law [9], as found in equation 4.15.

$$\langle \bar{u} \rangle_{high}(z) = \frac{u_{\tau,high}}{\kappa} \left[\ln \left(\frac{z}{z_{0,high}} \right) + \frac{2\Pi}{\kappa} \sin^2 \left(\frac{\pi}{2} \frac{z}{\delta} \right) \right] \quad (4.15)$$

Here, Π is set as a constant of 0.55 as recommended for constant pressure driven flows [9]. Figure 4.3 indicates an improved match between the NU-ADM and the double-log-law theory. One important assumption of the double-log-law theory is: the thrust on the wind turbine rotors is concentrated at hub height [15]. This assumption is naturally untrue and could explain differences between the NU-ADM and the double-log-law theory.

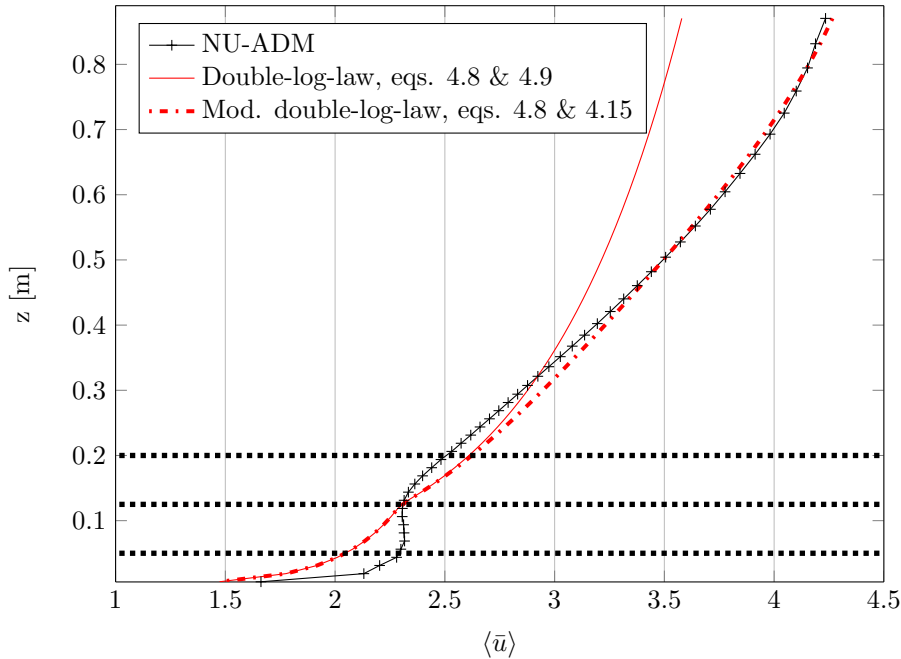


Figure 4.3: Comparison of time and slab averaged streamwise velocity profiles with (modified) double log law theory. Dotted lines indicate top-tip height, hub height and bottom-tip height.

Summarizing sections 4.2 and 4.3. The engineering wake solutions verified the calculation of the thrust coefficient and the streamwise reference velocity. Also, a good match for the wake velocity was found for the Risø analytic solution driven by the NU-ADM’s uniform equivalent thrust coefficient C_T^{loc} , see equation 3.19. From the required modification of Frandsen’s double-log-law theory, the significant influence of the pressure difference on model results has become apparent. For the validation by measurements, it is recommended to take the influence of the pressure difference in the outer region into consideration.

4.4 Validation by measurements

Validation is performed for the streamwise velocity profiles, the streamwise velocity fields in the turbine midplane and the turbulence intensity in the turbine midplane.

Figure 4.4 compares the streamwise velocity profile of the NU-ADM in the turbine midplane with the validation measurements. The velocity profiles at $x/D_{disk} = 4+$ are sampled at highest wake velocity. Sampling at $x/D_{disk} = 5$ is not possible due to the presence of the turbine at that position, see figure 4.1 for further clarification. Figure 4.4 gives a satisfactory match in streamwise velocity profile, however, there are noticeable differences. Again, an over-acceleration of the flow above top-tip height is found, likely the result of the fundamental difference between the experiment and the simulation: the application of a pressure difference to drive the flow. In order to prove this statement, the simulation results are reduced by the law of the wake as estimated by Coles’ wake law [9] by equation 4.16. This practice is only performed for validation purposes as presented in this section.

$$u_{\text{Coles}} = u_{\tau,high} \frac{2\Pi}{\kappa} \sin^2 \left(\frac{\pi z}{2 \delta} \right) \quad (4.16)$$

Here, $u_{\tau,high}$ is estimated by Frandsen’s double-log-law theory according to equation 4.13. Figure 4.5 gives the reduced simulation result and indicates a clear improvement of the match above top-tip height. Below top-tip height, Coles’ wake law does not directly hold due to the presence of the wind turbine. However, the pressure difference does influence the flow profiles resulting in a faster wake regeneration.

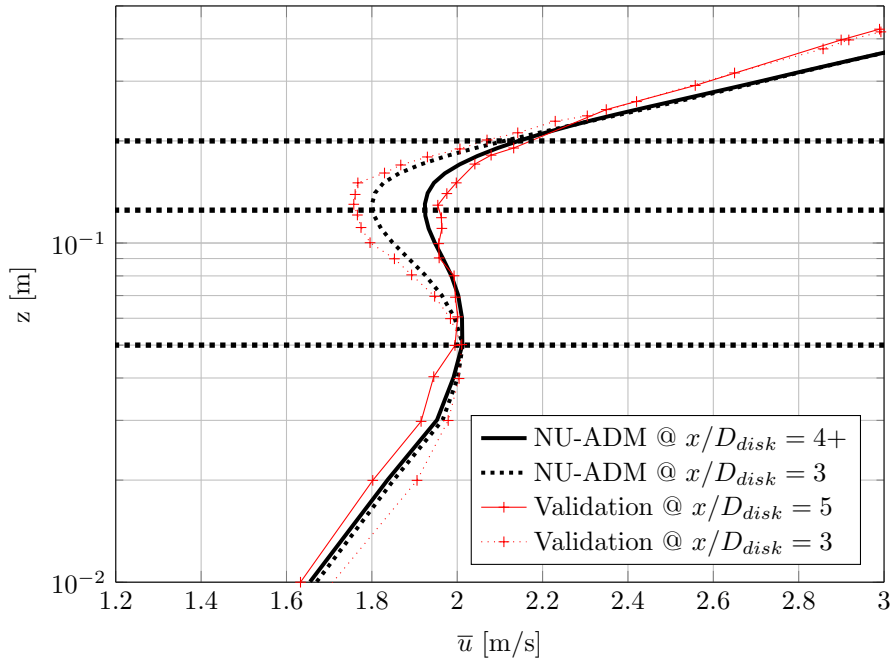


Figure 4.4: Comparison of streamwise velocity profiles at different positions behind the turbine in the turbine midplane.

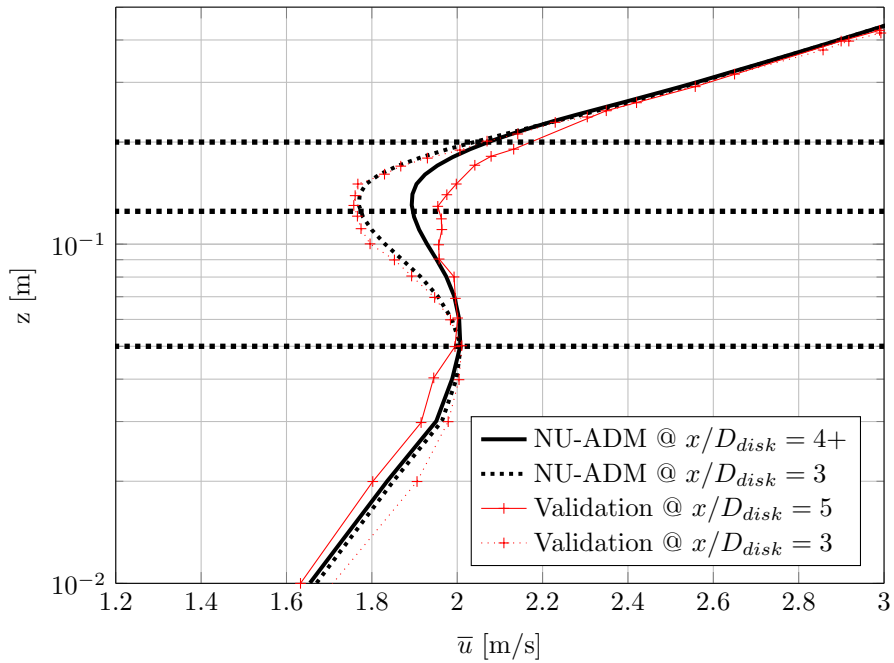


Figure 4.5: Comparison of streamwise velocity profiles at different positions behind the turbine in the turbine midplane. Simulation results are reduced by Coles' wake law for pressure driven flows.

Figures 4.6 and 4.7 compare the normalized streamwise velocity and turbulence intensity in the turbine midplane with the validation measurements. Here, the turbulence intensity is defined by equation 4.17. The hub velocity used for normalization is $u_{0,hub} = 2.4m/s$, corresponding with the undisturbed hub velocity of the validation case.

$$\frac{\sigma_u}{u_{0,hub}} = \frac{\sqrt{u'u' + \tau_{xx}}}{u_{0,hub}} \quad (4.17)$$

Figure 4.6(a) indicates a decent agreement of the streamwise velocity field. Velocities are higher overall for the simulations, again in line with expectation due to the application of a pressure difference. For the turbulence intensity, figure 4.7(a) indicates a good match. For the validation measurements, a peak in turbulence intensity is found slightly below top-tip height and between $x = 2D_{disk}$ and $x = 3D_{disk}$ behind the turbine. For the NU-ADM, this peak is found slightly below top-tip height and halfway between $x = 1D_{disk}$ and $x = 3D_{disk}$ behind the turbine. The turbulence intensity is higher overall for the simulation, especially noticeable above top-tip height. Table 4.2 gives the time-averaged performance measures and rotational speed of the NU-ADM. The latter is found as 81.7 rad/s, which is close to 78.4 rad/s as approximated from validation measurements by figure C.4. Measured values of the power production and thrust / power coefficient are unfortunately unavailable from the experiment. Therefore validation of these performance measures is not possible.

Table 4.2: Time-averaged results of the validated NU-ADM.

\bar{P}_x	$\bar{u}_{ref,disk}$	\bar{C}_P	$\bar{\Omega}$
[mW]	[m/s]	[-]	[rad/s]
35.66	1.953	0.3994	81.7

4.5 Conclusions on verification and validation

The code is verified by comparison of the analytic model with the implemented NU-ADM. It is found that any remaining errors in the code (if any) have a negligible influence on the results.

The engineering wake solutions verified the calculation of the thrust coefficient and the streamwise reference velocity. Here, a good match for the wake velocity was found for the Risø analytic solution driven by the NU-ADM's uniform equivalent thrust coefficient C_T^{loc} . From the required modification of Frandsen's double-log-law theory, the significant influence of the pressure difference on model results has become apparent.

Concluding on validation, it is stated that the implemented NU-ADM gives good results both quantitatively and qualitatively. Again, the significant influence of the pressure difference driving the flow is proven. Proper validation remains therefore difficult, not only due the fundamental difference of the application of a pressure difference, but also due to the absence of performance measures and quantified uncertainty of the measurements.

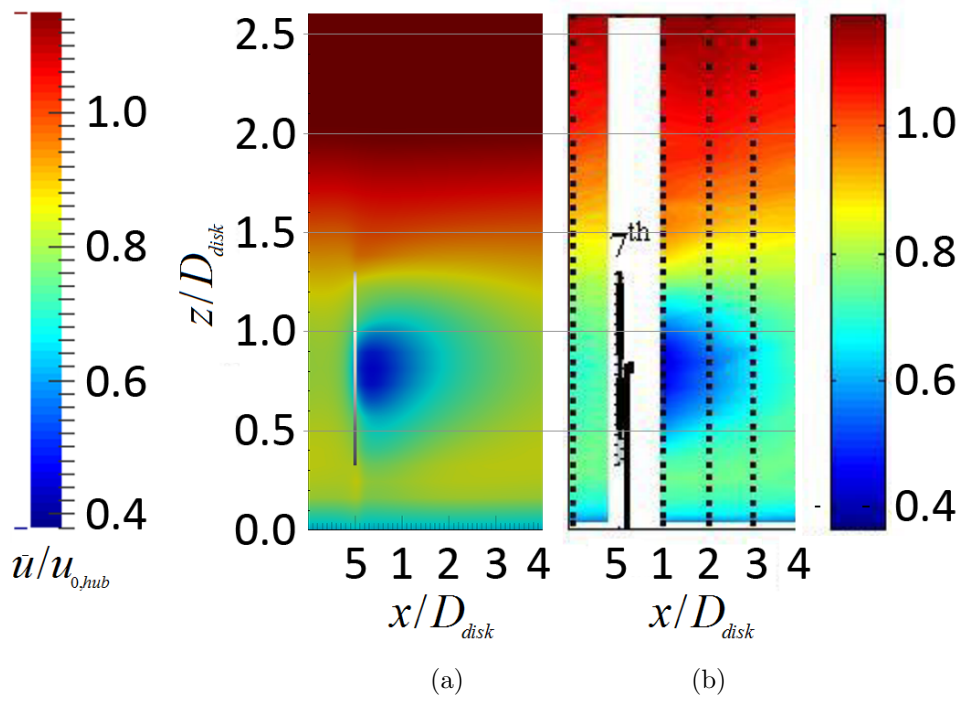


Figure 4.6: Comparison of normalized streamwise velocity over turbine midplane: (a) simulation result and (b) validation measurements. Left color bar is for simulation result and right color bar for validation measurements. The figures' aspect ratios are modified in line with available validation data.

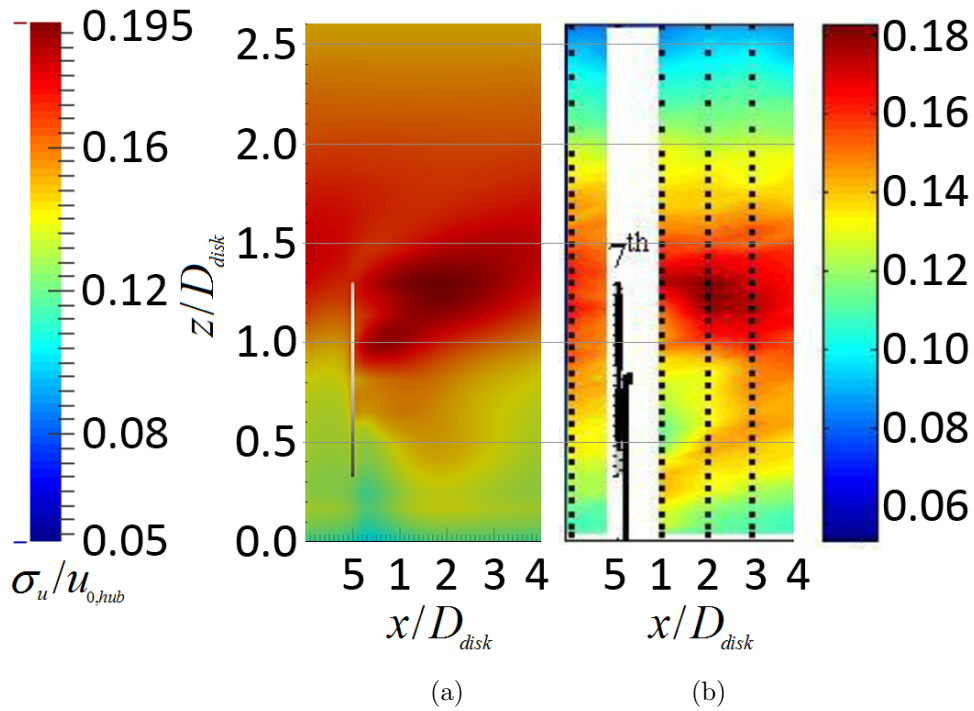


Figure 4.7: Comparison of turbulence intensity over turbine midplane: (a) simulation result and (b) validation measurements. Left color bar is for simulation result and right color bar for validation measurements. The figures' aspect ratios are modified in line with available validation data.

Chapter 5

Results and discussion for alternating tower heights

First, the tower height difference of the wind turbines is investigated and three wind farm configurations are introduced. Then, for each of these configurations the wind farm performance is discussed.

5.1 Tower height difference

In order to determine the appropriate and optimal tower height difference, runs with two consecutive single domains with differing tower height are performed. The tower height (hub-height) of the first single domain is expressed as $z_{hub,low}$ and for the second single wind turbine domain as $z_{hub,high}$. Results are compared in terms of relative surface overlap, Ψ , see figure 5.1 for a graphical representation of these terms. The following five cases are considered:

1. $z_{hub,low} = 0.125m$	$z_{hub,high} = 0.1625m$	$\Psi = 69\%$
2. $z_{hub,low} = 0.125m$	$z_{hub,high} = 0.1875m$	$\Psi = 50\%$
3. $z_{hub,low} = 0.125m$	$z_{hub,high} = 0.2125m$	$\Psi = 32\%$
4. $z_{hub,low} = 0.125m$	$z_{hub,high} = 0.2375m$	$\Psi = 16\%$
5. $z_{hub,low} = 0.125m$	$z_{hub,high} = 0.2750m$	$\Psi = 0\%$

The hub-height of the low turbine corresponds to the original turbine height as defined by the validation case for all cases. For the determination of the cases, the hub-height of the high turbine increases gradually until the overlap surface of the two swept areas is just 0%. The chosen hub-heights of the high turbines are in accordance with the single domain grid to ensure that all turbines are distributed over the grid identically. For example, if the disk center of the NU-ADM of the low turbine is located exactly at the intersection of four cells, then the disk center of the high turbine is also located exactly at the intersection of four cells (but higher). The performance of the cases with tower height alternation is compared with two high turbines at corresponding high hub-height, the latter is further referenced to as the '2h-case'. This choice of comparison is made to:

- Mitigate any economic and mechanical issues related to changing tower heights, i.e. if it is economically and mechanically feasible to position a multitude of turbines at high hub-height, then it is also economically and mechanically feasible to position half of these turbines at a lower hub-height.
- Ensure that the change in power production is the result of tower height alternation, i.e. if a case with tower height alternation is compared with the result of only low towers, then it is uncertain if the change in power production is the result of tower height alternation or the result of the fact that higher turbines generally produce more power.

A tower height difference is considered appropriate only if the physics proposed by Johnstone and Coleman (2012) apply. Recalling the physics behind a wind farm with mixed tower heights as proposed by Johnstone and Coleman (2012), the occurrence of the following is discussed:

- Decreased local and overall TKE production.
- A sawtooth curve for the Reynolds shear stress magnitude.

As any economic and mechanical issues related to changing tower heights are mitigated, only the following conditions are set for the definition of the optimal tower height difference:

- Maximum increase in power production.
- Realistic dimensions of turbine and tower heights.

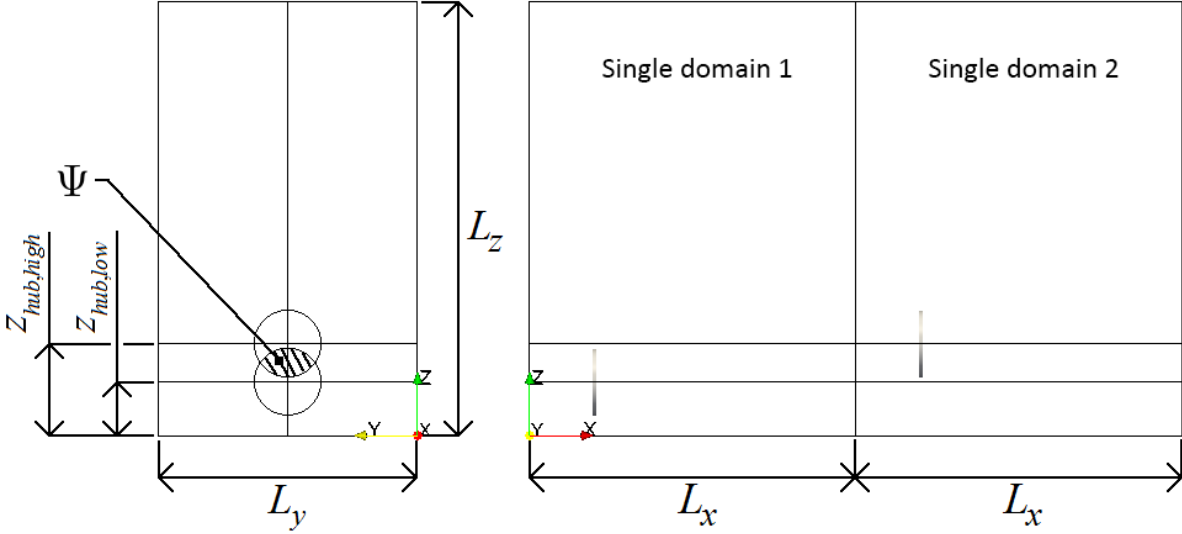


Figure 5.1: Graphical representation of different hub-heights, relative surface overlap and the two consecutive single domains.

5.1.1 Appropriateness of tower height difference

Equation 5.1 gives the domain averaged kinetic energy budget of the mean flow for any case with alternating tower heights. This budget is given in terms of the corresponding 2h-case and the change (Δ) as a result of tower height alternation. Equation 5.1 is the result of reordering equation 2.23.

$$\begin{aligned}
 \left(\iiint \bar{\epsilon}_{2h} dV + \Delta \iiint \bar{\epsilon} dV \right) = & - \left(\iiint \bar{w}_{2h} dV + \Delta \iiint \bar{w} dV \right) \\
 & - \left(\iiint \bar{\mathcal{P}}_{2h} dV + \Delta \iiint \bar{\mathcal{P}} dV \right) \\
 & - \left(\iiint E_{2h} dV + \Delta \iiint E dV \right)
 \end{aligned} \tag{5.1}$$

The term $\iiint \bar{\epsilon} dV$ can be rewritten as the sum of two terms: $\iiint \bar{\epsilon}_{eff} dV$ and $\iiint \bar{\epsilon}_{loss} dV$. Here, the first term corresponds to the effective mean kinetic energy extraction and is the energy flow potentially available for conversion to electric output. The second term is lost extraction, which is the result of the drag of the tower and nacelle. Furthermore, the TKE production term, $\iiint \bar{\mathcal{P}} dV$ can be rewritten as the sum of two terms: $\iiint \bar{\mathcal{P}}_{wall} dV$ and $\iiint \bar{\mathcal{P}}_{red} dV$. Here, the first term is an expression of the TKE production due to viscous wall shear and the second term is the

remainder. Equation 5.2 gives the expression of the TKE production due to viscous wall shear, note that this equation does not fully satisfy the rules of Reynolds averaging and is therefore intended as an estimation to quantify the influence of the wall. Furthermore, in equation 5.2, $\bar{\tau}$ is the time-averaged shear near the wall. Determination of this term is performed according to the Werner and Wengle wall function (equations 3.33 and 3.34) with $|u_{\parallel}|$ the spatial-average of the time-averaged streamwise velocity of the slab of cells closest to the wall.

$$\iiint \mathcal{P}_{wall} dV = \iint \left. \frac{\bar{\tau} \partial u}{\rho \partial z} \right|_{wall} dA \approx \iint \left. \frac{\bar{\tau} \partial u}{\rho \partial z} \right|_{wall} dA \quad (5.2)$$

Subtracting the term $\iiint \bar{\mathcal{E}}_{2h} dV$ from both sides of equation 5.1 gives an expression for the kinetic energy budget change due to application of tower height alternation. Application of the split of the extraction and TKE production terms, correction of the sign of the work and division of all terms by the total effective extraction of the corresponding 2h-case, $\iiint \bar{\mathcal{E}}_{eff,2h} dV$, results in equation 5.3.

$$\begin{aligned} \frac{\Delta \iiint \bar{\mathcal{E}}_{eff} dV}{\iiint \bar{\mathcal{E}}_{2h,eff} dV} = & - \frac{\Delta \iiint \bar{\mathcal{E}}_{loss} dV}{\iiint \bar{\mathcal{E}}_{2h,eff} dV} + \frac{\Delta \iiint \bar{W} dV}{\iiint \bar{\mathcal{E}}_{2h,eff} dV} - \frac{\Delta \iiint \bar{\mathcal{P}}_{red} dV}{\iiint \bar{\mathcal{E}}_{2h,eff} dV} \\ & - \frac{\Delta \iiint \bar{\mathcal{P}}_{wall} dV}{\iiint \bar{\mathcal{E}}_{2h,eff} dV} - \frac{\Delta \iiint E dV}{\iiint \bar{\mathcal{E}}_{2h,eff} dV} \end{aligned} \quad (5.3)$$

The intention of equation 5.3 is to give an indication of the source of the relative change of effective extraction. In words: the change of effective extraction is the result of:

- a change in the extraction losses due to the tower and nacelle.
- a change in the resultant pressure work.
- a change in the TKE production (minus viscous effect at the wall).
- a change in the energy dissipation due to viscous effects at wall.
- a change in the budget error, see equation 2.24.

Table 5.1 gives the change of the effective extraction and the magnitude of the components driving this change.

Table 5.1: Change of the effective extraction and the magnitude of the components driving this change due to tower height alternation.

Surface overlap	$\frac{\Delta \iiint \bar{\mathcal{E}}_{eff} dV}{\iiint \bar{\mathcal{E}}_{eff,2h} dV}$	$\frac{\Delta \iiint \bar{\mathcal{E}}_{loss} dV}{\iiint \bar{\mathcal{E}}_{eff,2h} dV}$	$\frac{\Delta \iiint \bar{W} dV}{\iiint \bar{\mathcal{E}}_{eff,2h} dV}$	$\frac{\Delta \iiint \bar{\mathcal{P}}_{red} dV}{\iiint \bar{\mathcal{E}}_{eff,2h} dV}$	$\frac{\Delta \iiint \bar{\mathcal{P}}_{wall} dV}{\iiint \bar{\mathcal{E}}_{eff,2h} dV}$	$\frac{\Delta \iiint E dV}{\iiint \bar{\mathcal{E}}_{eff,2h} dV}$
%	%	%	%	%	%	%
69	+1.611	-1.791	+5.755	+5.134	+0.436	+0.370
50	+2.545	-3.161	+9.313	+8.722	+0.331	+0.877
32	+5.119	-4.614	+6.973	+6.698	+0.546	-0.774
16	+5.632	-6.240	+7.443	+6.467	+0.973	+0.612
0	+10.763	-9.165	+7.742	+6.918	+0.419	-1.214

The results from table 5.1 support the following statements:

- Effective extraction increases with decreasing surface overlap, i.e. increasing tower height difference increases effective extraction. Increased effective extraction greatly surpasses the single domain sampling error for all cases.
- Extraction losses (due to tower and nacelle) decrease due to tower height alternation. The larger the tower height difference, the larger this decrease.
- Pressure work changes accordingly: any change in total extraction and TKE production results in a change in total pressure work due to balancing of bulk velocity.
- TKE production increases due to tower height alternation, indicating a larger undesired loss of mean kinetic energy to TKE.
- The energy dissipation due to viscous effects at the wall increases slightly, but its effect on the total effective power production is minor (<5% on the total absolute sum of change components). This increase of energy dissipation due to viscous effects at the wall appears not to be in line with expectations: i.e. it may be expected that positioning a turbine closer to the wall would result in a reduced streamwise velocity near the wall and thus a decreased energy dissipation due to viscous effects at the wall.
- The effect of the budget error on the effective extraction is null. The source of the budget error is not in the effective extraction term, $\bar{\mathcal{E}}_{eff}$, but in all other terms. The effective extraction is defined by taking the statistical time-average of an instantaneous signal corresponding with effective extraction. The error (uncertainty) of this signal has been found to be small, $\ll 1\%$, as summarized in section 3.4.1.
- There is a strong indication that the majority of increased power production is the result of the decrease in extraction losses, i.e. reduced tower drag surface.

Regarding the last statement, table 5.2 gives the change in effective extraction and the magnitude of the components driving this change due to tower height alternation for the case with 32% overlap without the application of towers.

Table 5.2: Change of the effective extraction and the magnitude of the components driving this change due to tower height alternation for the case with 32% surface overlap without the application of towers.

Surface overlap	$\frac{\Delta \iiint \bar{\mathcal{E}}_{eff} dV}{\iiint \bar{\mathcal{E}}_{eff, 2h} dV}$	$\frac{\Delta \iiint \bar{\mathcal{E}}_{loss} dV}{\iiint \bar{\mathcal{E}}_{eff, 2h} dV}$	$\frac{\Delta \iiint \mathcal{W} dV}{\iiint \bar{\mathcal{E}}_{eff, 2h} dV}$	$\frac{\Delta \iiint \bar{\mathcal{P}}_{red} dV}{\iiint \bar{\mathcal{E}}_{eff, 2h} dV}$	$\frac{\Delta \iiint \bar{\mathcal{P}}_{wall} dV}{\iiint \bar{\mathcal{E}}_{eff, 2h} dV}$	$\frac{\Delta \iiint E dV}{\iiint \bar{\mathcal{E}}_{eff, 2h} dV}$
%	%	%	%	%	%	%
32NT	+0.017	+0.460	+1.658	+3.453	-1.295	-0.977

The results from table 5.2 support the following statements:

- Increase of effective extraction is now, contrary to the case with application of towers, insignificant.
- Extraction losses increase and only comprehend drag losses over the nacelles.
- Total TKE production again increases due to tower height alternation, indicating a larger undesired overall loss of mean kinetic energy to TKE.
- The energy dissipation due to viscous effects at the wall decreases, contrary to the case with application of towers. This result is now in line with expectations.
- For the 32% surface overlap case, the majority of increased power production is indeed the result of the decrease in extraction losses due to reduced tower drag surface.

Figures 5.2 and 5.3 give the slab averaged mean kinetic energy profiles for the 32% surface overlap with and without application of towers, respectively. Tables 5.1 and 5.2 show an overall increase in TKE production by tower height alternation for both cases. The same result is found in figures 5.2 and 5.3, furthermore, the increase in TKE production is mainly concentrated near the surface overlap between turbines. Figure 5.4 gives the slab averaged mean shear stress magnitude, τ_{SSM} , which is defined by equation 5.4, note that subgrid contribution is included.

$$\tau_{SSM} = \sqrt{\langle u'w' \rangle + \bar{\tau}_{xz} + \langle v'w' \rangle + \bar{\tau}_{yz}} \quad (5.4)$$

As given in equation 2.18, the transport of mean kinetic energy due to Reynolds stresses is dependent on the gradient of these stresses. Lower gradients (see figure 5.4) indeed result in a lower transport as found in figures 5.2 and 5.3. TKE production due to Reynolds stresses is dependent on the absolute value of these stresses, as given in equation 2.19. Figure 5.4 gives an increase in Reynolds stresses due to tower height alternation. From figures 5.2 and 5.3, a higher TKE production is indeed found. From the results as presented in figures 5.2 and 5.3 and figure 5.4, it is found that:

- Local and overall TKE production increases due to tower height alternation.
- A sawtooth curve for the Reynolds stresses is not found for the 32% surface overlap. Figure 5.5 gives the normalized shear stress magnitude for the largest tower height difference with 0% surface overlap. Here, a sawtooth curve begins to form, however, for a sawtooth with two near identical teeth, a far larger tower height difference would be required.
- Additionally, an increased power extraction is found, however only for the case with the application of towers. There is strong evidence that increase in power production due to tower height alternation is only the result of decreased tower drag surface.

5.1.2 Optimal tower height difference

None of the tower height alternation cases are appropriate with respect to the physics as proposed by Coleman and Johnstone (2012) [18]. Also, the proposed physics cannot be confirmed to be valid for tower height alternation. Therefore, a non-optimal choice of tower height difference based on the optimization conditions is made for further advancements.

Table 5.3 gives the tower height to diameter ratio for the high turbine of each investigated case. The tower height to turbine diameter ratio of common wind turbines is about 0.75 to 1x turbine diameter. Furthermore, table 5.1 gave a maximum increase in effective extraction for the largest tower height difference. Therefore, the 32% surface overlap case is chosen as a midway between sufficient increase in effective extraction and realistic tower heights: $z_{hub,low} = 0.125m$ and $z_{hub,high} = 0.2125m$.

Table 5.3: Ratio of high turbine height to turbine diameter for each of the five surface overlap cases.

Surface overlap	$\frac{z_{hub}}{D_{disk}}$
%	-
69	1.06
50	1.22
32	1.38
16	1.54
0	1.78

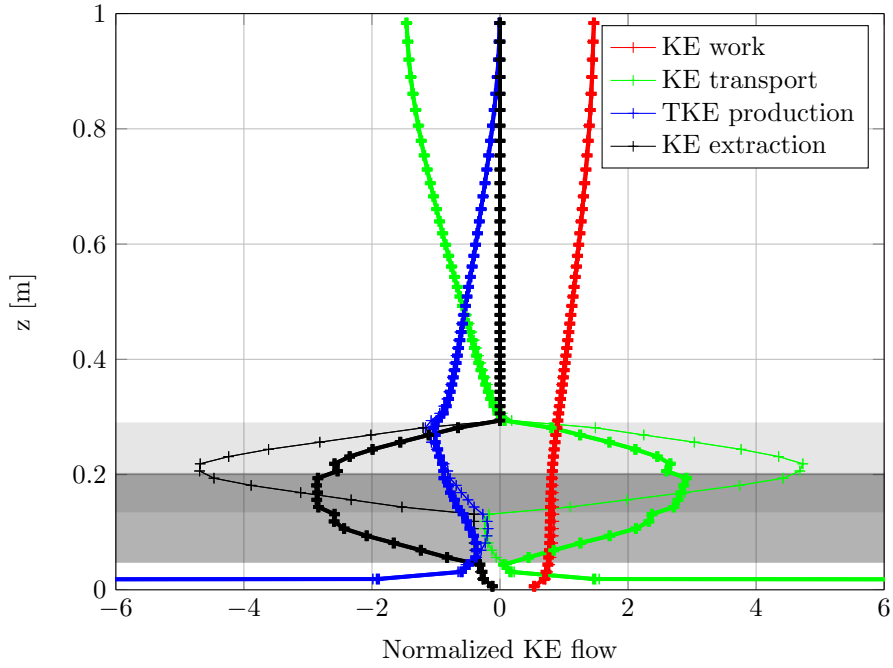


Figure 5.2: Thin line is the 2h-case, thick line is for tower height alternation. Slab averaged mean kinetic energy profiles for 32% surface overlap with application of towers, normalized with total pressure work $(\bar{u}_{bulk} \left[\frac{\Delta p_{mod}}{L_x} \right] L_z)$. (Backgrounds: darkest grey is surface overlap, lightest grey is the remaining swept area of the high turbine and medium-dark grey is the remaining swept area of the low turbine.)

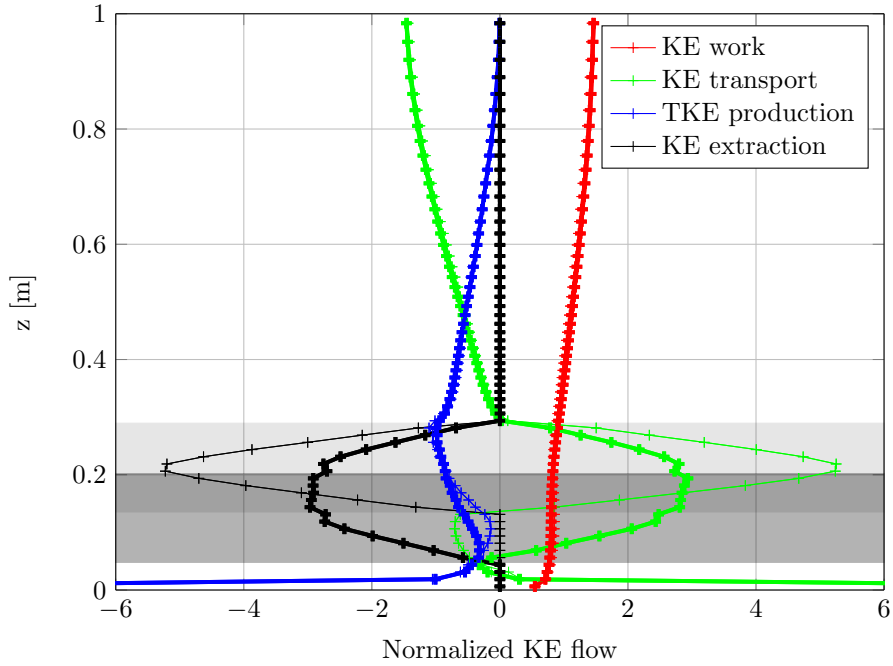


Figure 5.3: Thin line is the 2h-case, thick line is for tower height alternation. Slab averaged mean kinetic energy profiles for 32% surface overlap without application of towers, normalized with total pressure work $(\bar{u}_{bulk} \left[\frac{\Delta p_{mod}}{L_x} \right] L_z)$. (Backgrounds: darkest grey is surface overlap, lightest grey is the remaining swept area of the high turbine and medium-dark grey is the remaining swept area of the low turbine.)

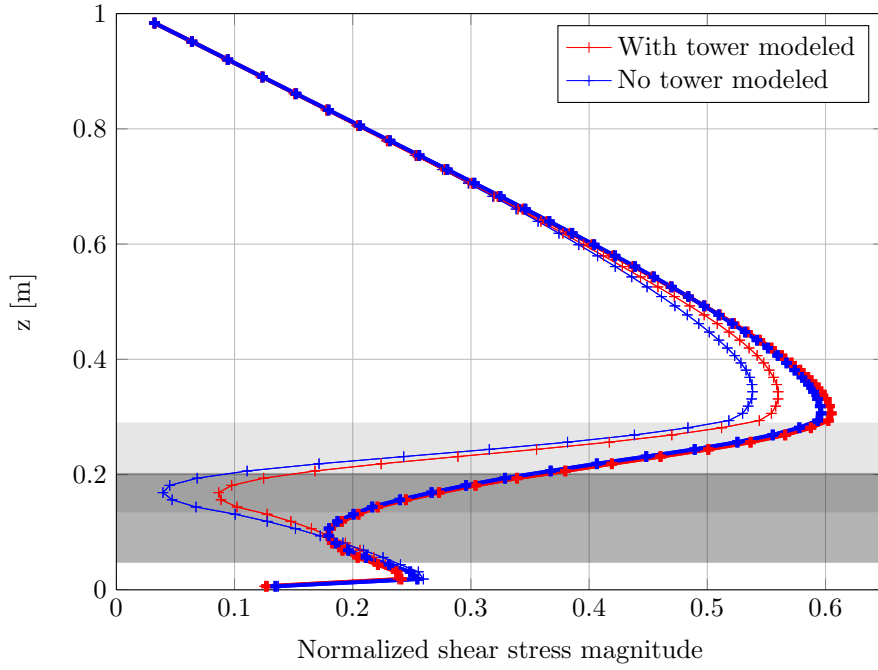


Figure 5.4: Thin line is the 2h-case, thick line is for tower height alternation. Slab averaged mean shear stress magnitude for 32% surface overlap with and without application of towers, normalized with $\left(\left[\frac{\Delta p_{mod}}{L_x}\right] L_z\right)$. (Backgrounds: darkest grey is surface overlap, lightest grey is the remaining swept area of the high turbine and medium-dark grey is the remaining swept area of the low turbine.)

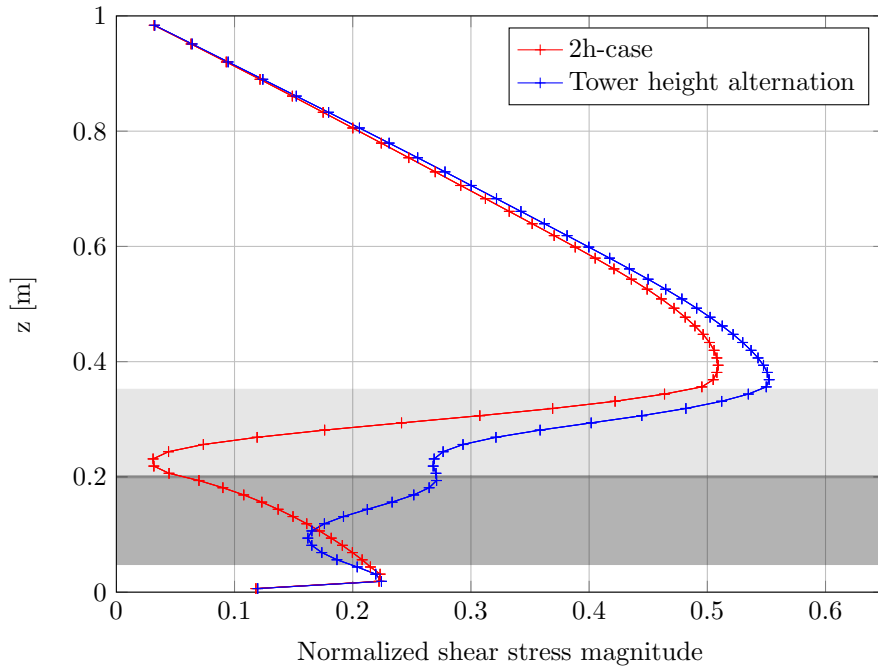


Figure 5.5: Slab averaged mean shear stress magnitude for 0% surface overlap, normalized with $\left(\left[\frac{\Delta p_{mod}}{L_x}\right] L_z\right)$. (Backgrounds: lightest grey is the swept area of the high turbine and medium-dark grey is the swept area of the low turbine.)

5.2 Introduction of wind farm configurations

All wind farm configurations are row configurations. The following wind farm alternation configurations (z-spatial) are considered:

1. High turbines only (2h), figure 3.9.
2. Tower heights alternating in row configuration (RA), figure 5.6.
3. Tower heights alternating in staggered configuration (SA), figure 5.7.

For the understanding of the remainder of this study it is important to understand the difference between a column and a row in a wind farm. Columns follow the direction of the bulk flow and rows are perpendicular to the direction of the bulk flow.

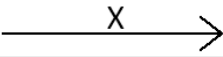
col												
6	61	62	63	64	65	66	67	68	69	70	71	72
5	49	50	51	52	53	54	55	56	57	58	59	60
4	37	38	39	40	41	42	43	44	45	46	47	48
3	25	26	27	28	29	30	31	32	33	34	35	36
2	13	14	15	16	17	18	19	20	21	22	23	24
1	1	2	3	4	5	6	7	8	9	10	11	12
row	1	2	3	4	5	6	7	8	9	10	11	12

Figure 5.6: Wind farm configuration in row alternation (RA). Grey turbine numbers are low tower turbines, black turbine numbers are high tower turbines.

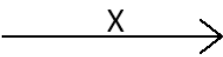
col												
6	61	62	63	64	65	66	67	68	69	70	71	72
5	49	50	51	52	53	54	55	56	57	58	59	60
4	37	38	39	40	41	42	43	44	45	46	47	48
3	25	26	27	28	29	30	31	32	33	34	35	36
2	13	14	15	16	17	18	19	20	21	22	23	24
1	1	2	3	4	5	6	7	8	9	10	11	12
row	1	2	3	4	5	6	7	8	9	10	11	12

Figure 5.7: Wind farm configuration in staggered alternation (SA). Grey turbine numbers are low tower turbines, black turbine numbers are high tower turbines.

5.3 Power production and mean kinetic energy profiles

In this section the sum of the mean production of all 72 turbines combined is considered. Equation 5.5 gives the relation between effective extraction and total power production.

$$\iiint \bar{\mathcal{E}}_{eff} dV = \frac{1}{\rho} \sum^{N_{wt}} \bar{P}_x \quad (5.5)$$

Table 5.4 gives the change in effective extraction due to tower height alternation relative to the 2h-case. Here, the magnitude of the components driving this change is given in terms of equation 5.3. For both RA and SA configurations, an increase in total mean power production is found. Furthermore, a decrease in extraction losses due to the tower and nacelle is found, while an undesired increase in TKE production is present. Similar to the results in section 5.1, there is a strong indication that the increase in effective extraction is mainly the result of a decrease in extraction losses due to the decrease of total tower drag surface.

Table 5.4: Change of the effective extraction and the magnitude of the components driving this change due to tower height alternation relative to the 2h-case.

Spatial config.	$\frac{\Delta \iiint \bar{\mathcal{E}}_{eff} dV}{\iiint \bar{\mathcal{E}}_{eff,2h} dV}$	$\frac{\Delta \iiint \bar{\mathcal{E}}_{loss} dV}{\iiint \bar{\mathcal{E}}_{eff,2h} dV}$	$\frac{\Delta \iiint \bar{W} dV}{\iiint \bar{\mathcal{E}}_{eff,2h} dV}$	$\frac{\Delta \iiint \bar{P}_{red} dV}{\iiint \bar{\mathcal{E}}_{eff,2h} dV}$	$\frac{\Delta \iiint \bar{P}_{wall} dV}{\iiint \bar{\mathcal{E}}_{eff,2h} dV}$	$\frac{\Delta \iiint E dV}{\iiint \bar{\mathcal{E}}_{eff,2h} dV}$
	[%]	[%]	[%]	[%]	[%]	[%]
RA	+4.658	-3.927	+3.501	+2.872	+0.731	-0.838
SA	+4.692	-3.569	+4.068	+3.641	+0.726	-1.429

When comparing the RA and SA configurations, the results from table 5.4 support the following statements:

- The SA configuration shows a greater increase in power production. This increase is however less than 1% larger than the increase of the RA configuration. Based on the expected sampling error of about 0.5% for the time-averaged results (as summarized in 3.4.2), the difference is insignificant.
- TKE production is higher for the SA configuration. It can thus be expected that the SA configuration is more turbulent (higher Reynolds stresses) and the gradient of the wake shear layers larger.

Figures 5.8 and 5.9 compare the slab averaged kinetic energy flow profiles of the RA and SA configurations with the 2h-case. The (normalized) profiles of the RA and SA configurations are near identical. For both alternation configurations the following statements hold regarding the slab averaged kinetic energy flow profiles:

- The KE transport profiles of the 2h-case indicate an entrainment of kinetic energy from the flow below the turbines. Application of tower height alternation suppresses this transport mechanism.
- Locally, the TKE production only increases at heights with surface overlap between turbines. Contrary to the profiles as presented in figure 5.2 a (slab averaged) decrease in TKE production is found near top-tip height of the high turbines.

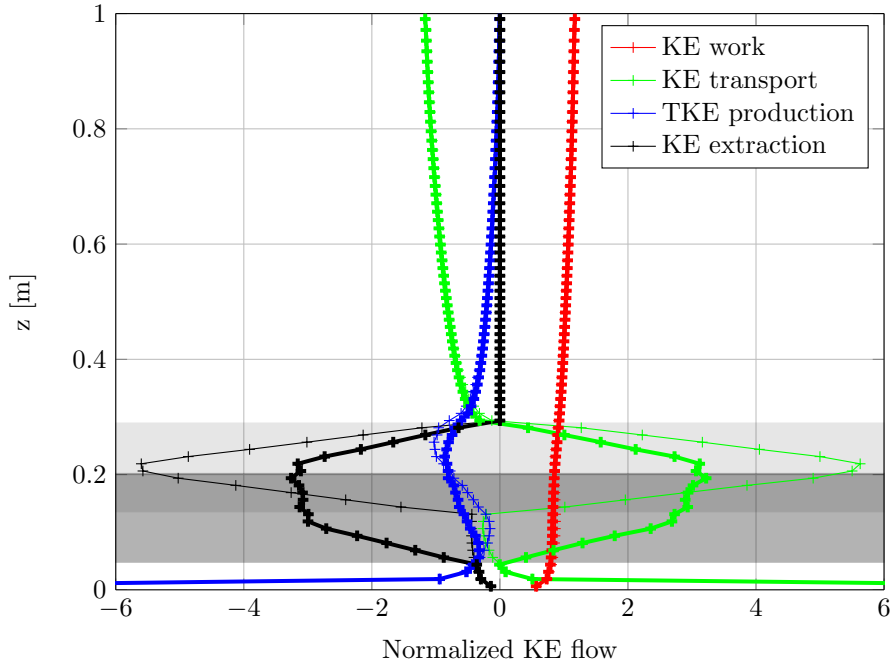


Figure 5.8: Thin line is the 2h-case, thick line is for RA. Slab averaged mean kinetic energy profiles for row alternation (RA), normalized with total pressure work $\left(\bar{u}_{bulk} \left[\frac{\Delta p_{mod}}{L_x}\right] L_z\right)$. (Backgrounds: darkest grey is surface overlap, lightest grey is the remaining swept area of the high turbines, medium-dark grey is the remaining swept area of the low turbines.)

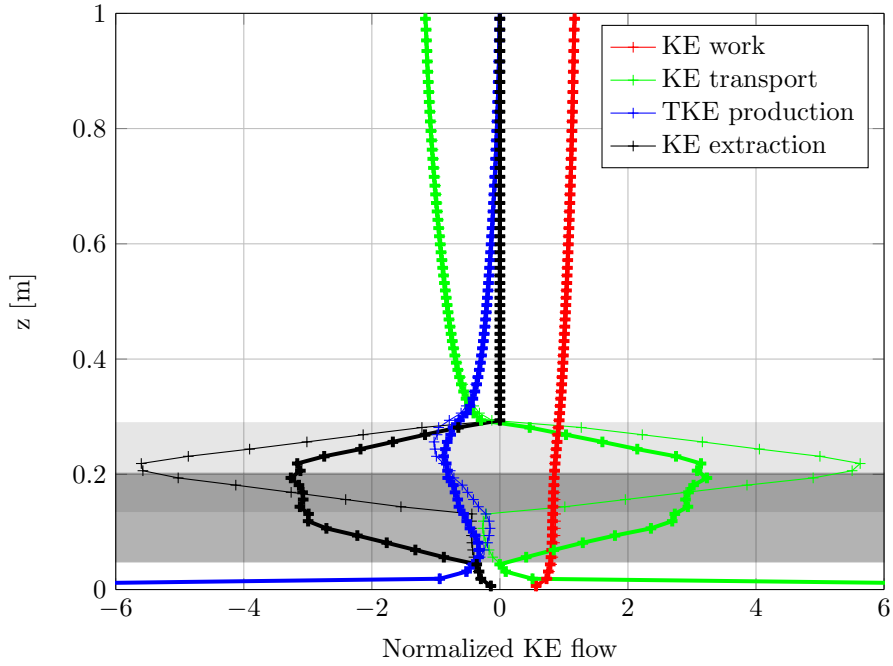


Figure 5.9: Thin line is the 2h-case, thick line is for SA. Slab averaged mean kinetic energy profiles for staggered alternation (SA), normalized with total pressure work $\left(\bar{u}_{bulk} \left[\frac{\Delta p_{mod}}{L_x}\right] L_z\right)$. (Backgrounds: darkest grey is surface overlap, lightest grey is the remaining swept area of the high turbines, medium-dark grey is the remaining swept area of the low turbines.)

5.4 Local fluctuation of power production

Figure 5.10 gives the time-series for the power production of four centrally located turbines: turbine 29, 30, 41 and 42 for each of the three configurations. For the 2h-case, figure 5.10(a), it is found that turbines in the same column, i.e. turbines 29 and 30, and, 41 and 42, produce approximately the same amount of power over the whole time-series. For the other two configurations, turbines in the same column follow the same trend in power production while the low turbines always give a lower production than the high turbines. For the alternation configurations, the power production of two separate columns appear to be following a weakly identical trend, an observation absent in the 2h-case. For the SA configuration, figure 5.10(c), there appears to be a stronger relation between the power production of two columns than in any other of the two configurations. Table 5.5 firstly compares the largest cross-correlation coefficients between two turbines in the same column but on different rows (CC row) for the two alternating configurations with the 2h-case. Secondly, the largest cross-correlation coefficients between two turbines on different columns (CC column) are compared.

Table 5.5: Comparison of cross-correlation coefficients and standard deviations of time-series of power production between the 2h-case and the two alternating configurations. All bold values of the standard deviations correspond to high turbines.

Spatial config.	CC row	CC column	$\sigma_{P_x}(T29)$	$\sigma_{P_x}(T30)$	$\sigma_{P_x}(T41)$	$\sigma_{P_x}(T42)$
	[-]	[-]	[mW]	[mW]	[mW]	[mW]
2h	0.41	0.15	5.0	5.0	4.8	4.8
RA	-9.1%	-5.3%	-4.7%	+5.6%	+4.4%	+34%
SA	-11%	+9.3%	+5.0%	+32%	+19%	-1.7%

Table 5.5 shows for both alternation configurations a decrease of about 10% for the cross-correlation coefficient between two turbines on the same column but on different rows (CC row). Therefore, not only is there a difference in absolute power production between two consecutive turbines in a column, they are also less strongly correlated to each other. This result is to be expected, as wakes only partly overlap in the alternation configurations. Furthermore, table 5.5 indeed gives the highest cross-correlation coefficient between two turbines in different columns (CC column) for the SA configuration. Simultaneously, this cross-correlation coefficient (CC column) decreases compared with the 2h-case for the RA configuration. To explain this observation, the following is considered:

- Explaining the decrease of CC column for the RA configuration, figure 5.10 (b). The wake of turbine 29 is obstructed by the wake of turbine 41 more or less identical to the 2h-case (same heights). Furthermore, turbine 29 is at a different height than turbine 42 (partial overlap), resulting in a lower CC column compared to the 2h-case.
- Explaining the increase of CC column for the SA configuration, figure 5.10 (c). The wake of turbine 29 is less obstructed by the wake of turbine 41 due to a difference in heights. Therefore, compared to the 2h-case, the wake of turbine 29 can more easily influence turbine 42 and thus CC column is higher.

For each of the four turbines the standard deviation of the power production is determined over the statistical time-averaging period, $T_{stat,avg}$. Table 5.5 gives for the high turbines of both alternation configurations an increase of the standard deviation of the power production by about 5 to 34%. Simultaneously, the standard deviation of the low turbines remain approximately the same compared with the same high turbine in the 2h-case. Therefore, there is a strong indication that the local fluctuation in power production increases for all high turbines within the alternation configurations.

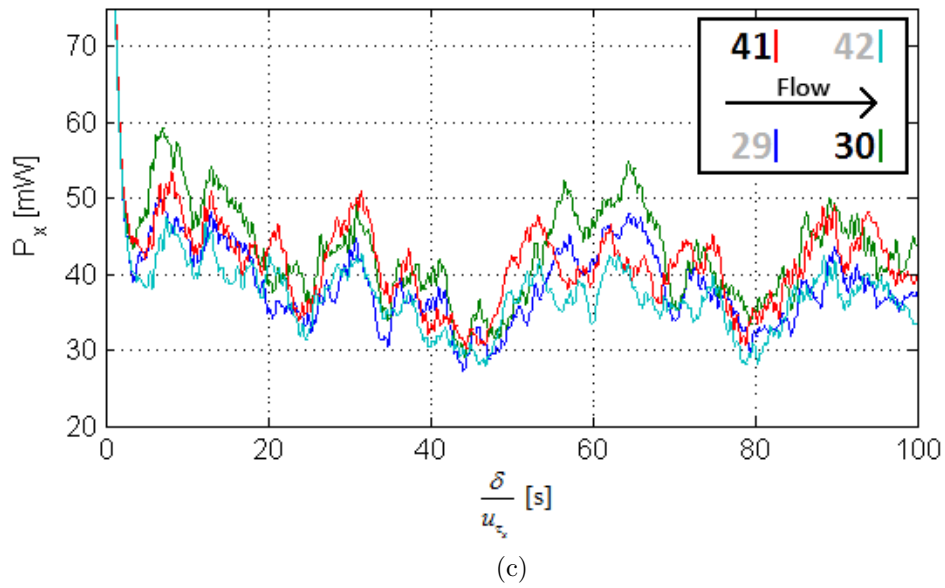
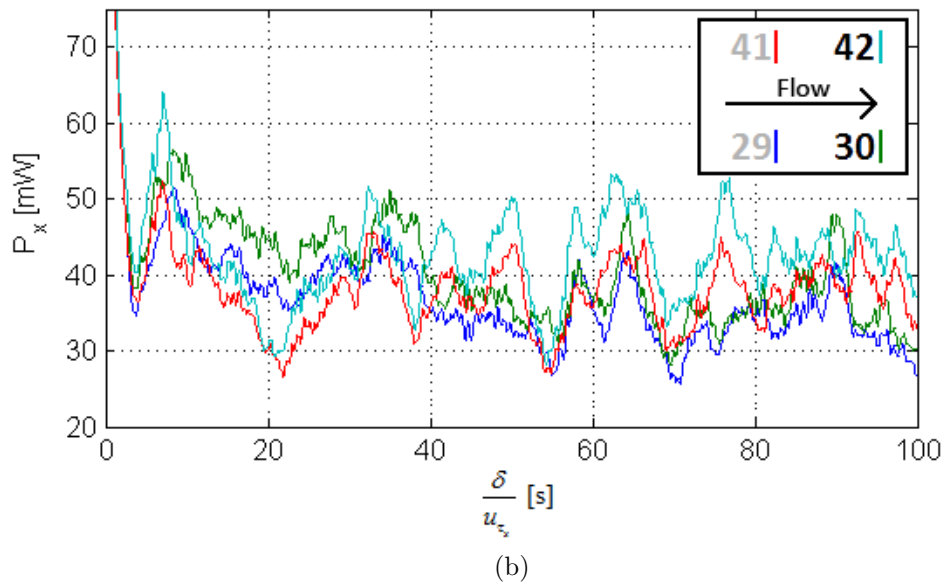
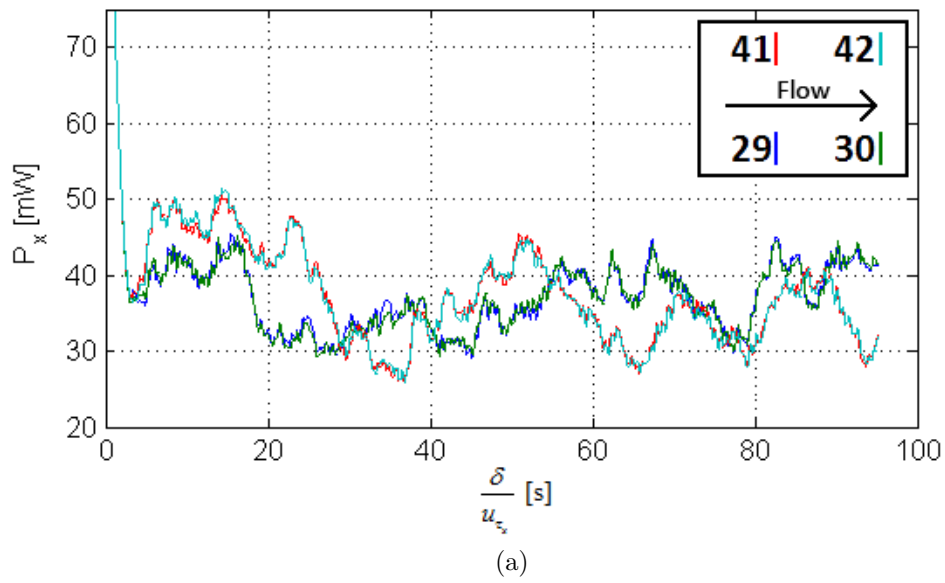


Figure 5.10: Time-series of power production for four centrally located turbines: 29, 30, 41 and 42. (a) High turbines only (2h), (b) Row alternation (RA), (c) Staggered alternation (SA).

5.5 Fatigue and flow fields

To give an indication of the change in fatigue life due to tower height alternation various flow fields are presented. Firstly, links to moving instantaneous flow fields are given. Secondly, the instantaneous flow fields of the streamwise velocity are given, and various structures and phenomena are identified qualitatively. Lastly, the time-averaged flow fields of the streamwise velocity and the $\overline{u'u'}$ Reynolds stress are presented.

Moving instantaneous flow fields

The following movies of the flow fields through the horizontal plane at $z = z_{hub,high}$ and the midplane of the sixth column of turbines are available:

- Streamwise velocity for 2h: <http://bit.ly/1XFqioZ>
- Streamwise velocity for RA: <http://bit.ly/1FvkL9h>
- Streamwise velocity for SA: <http://bit.ly/1Lh3QsV>
- Comparison in the turbine mid-plane: <http://bit.ly/1g6T2VO>

Instantaneous fields

Figure 5.11 gives the instantaneous flow field of the streamwise velocity over the horizontal plane at $z = z_{hub,high}$ for all three configurations. Turbines are located at the intersection of the grid lines. For the RA and SA configurations the low turbines are not as distinctly recognizable, which is the result of the set height of the horizontal plane section. Behind the turbines, the wakes exhibits a meandering structure for all three configurations. Directly behind the turbines, some back-flow is found for some of the turbines. This might be an indication of the formation of temporary vortices (non-coherent) close to the wind turbine which are quickly perturbed by the semi-permeable character of the actuator disks. Between adjacent columns, the velocity is generally higher and large structures of increased velocity are present. From the moving instantaneous fields it is found that these structures exhibit Lagrangian coherency over multiple domain pass-throughs. Figure 5.12 gives the instantaneous flow field of the streamwise velocity at the turbine midplanes of the third and fourth column. Again, wake meandering and local back-flow is found. No distinct differences between the alternation configurations in the wake meandering process can be identified based on figure 5.12. Further analyses of wake meandering, such as its frequency and amplitude, is however considered out of scope.

Time-averaged fields

Figure 5.13 gives the time-averaged flow field of the streamwise velocity at the turbine midplanes of the third and fourth column. Overall velocities are slightly higher for the row and staggered alternation configurations, figures 5.13(c) and (d) and 5.13(e) and (f) respectively. These overall higher velocities (i.e. bulk velocity) are in line with the increased power production and the overall increased mean kinetic energy work, $\iiint \bar{W} dV$, as found in table 5.4. Furthermore, no back-flow is present giving an indication that any vortices directly behind the turbines are not coherent. Figure 5.14 gives the time-averaged $\overline{u'u'}$ Reynolds stress (including sub-grid contribution) at the midplanes of the third and fourth column. Production of $\overline{u'u'}$ is strongest near top-tip height of the turbines. For the alternation configurations, the high turbines exhibit an increased production of $\overline{u'u'}$ due to the increased gradient of the shear layer present at top-tip height. The low turbines in the alternation configurations produce less $\overline{u'u'}$ compared with the same high turbine of the 2h-case as the gradient of the shear layer near top-tip of the low turbines is less strong. Directly in front of the turbines, the $\overline{u'u'}$ Reynolds stress for both alternation configurations is smaller than for the 2h-case. Furthermore, the Reynolds stresses of the SA configuration are higher than for the RA configuration. Therefore, the TKE production may be expected to be higher, as verified by table 5.4.

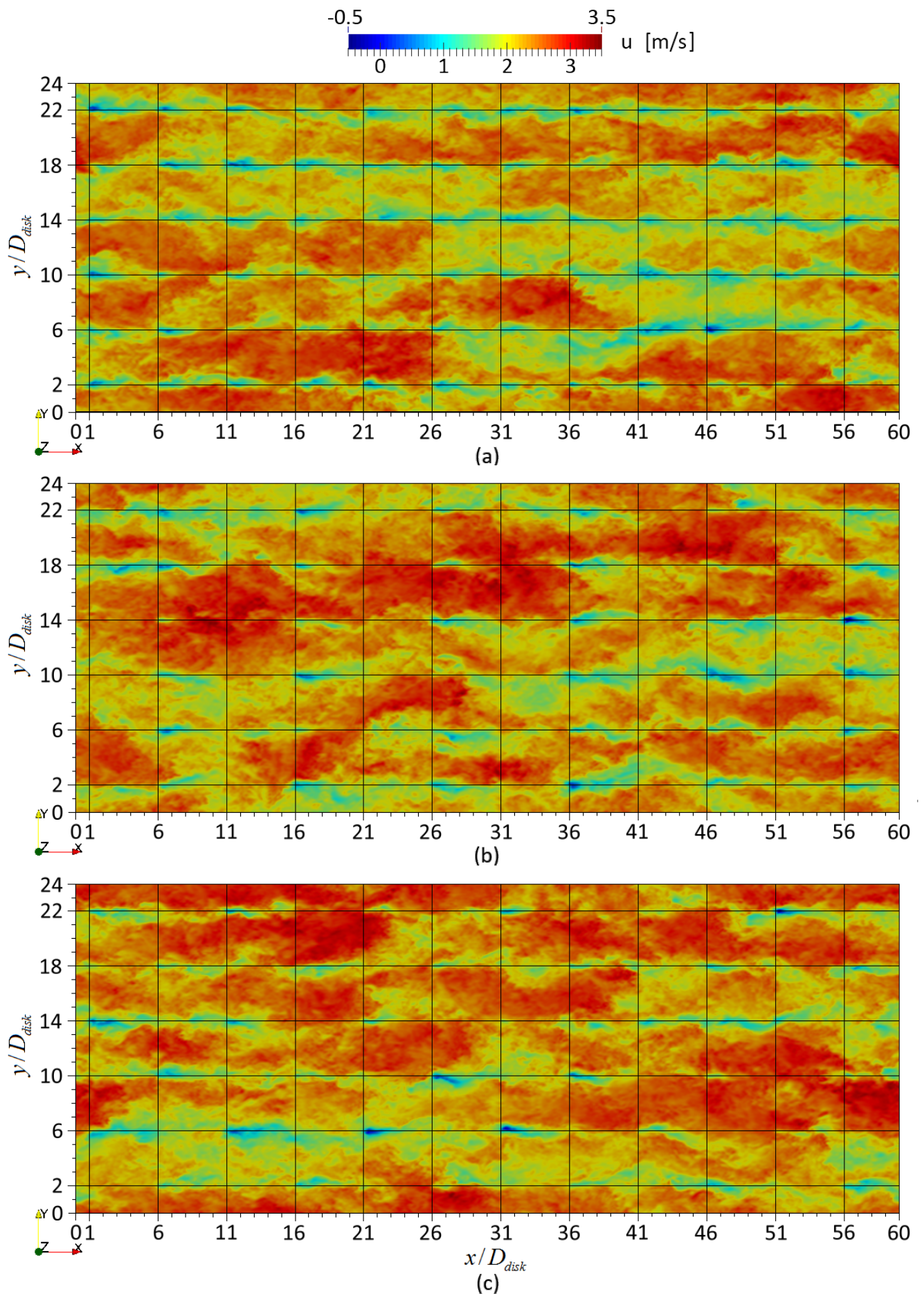


Figure 5.11: Instantaneous flow-field of streamwise velocity, top view at $z = z_{hub,high}$. (a) high turbines only (2h), (b) row alternation (RA), (c) staggered alternation (SA).

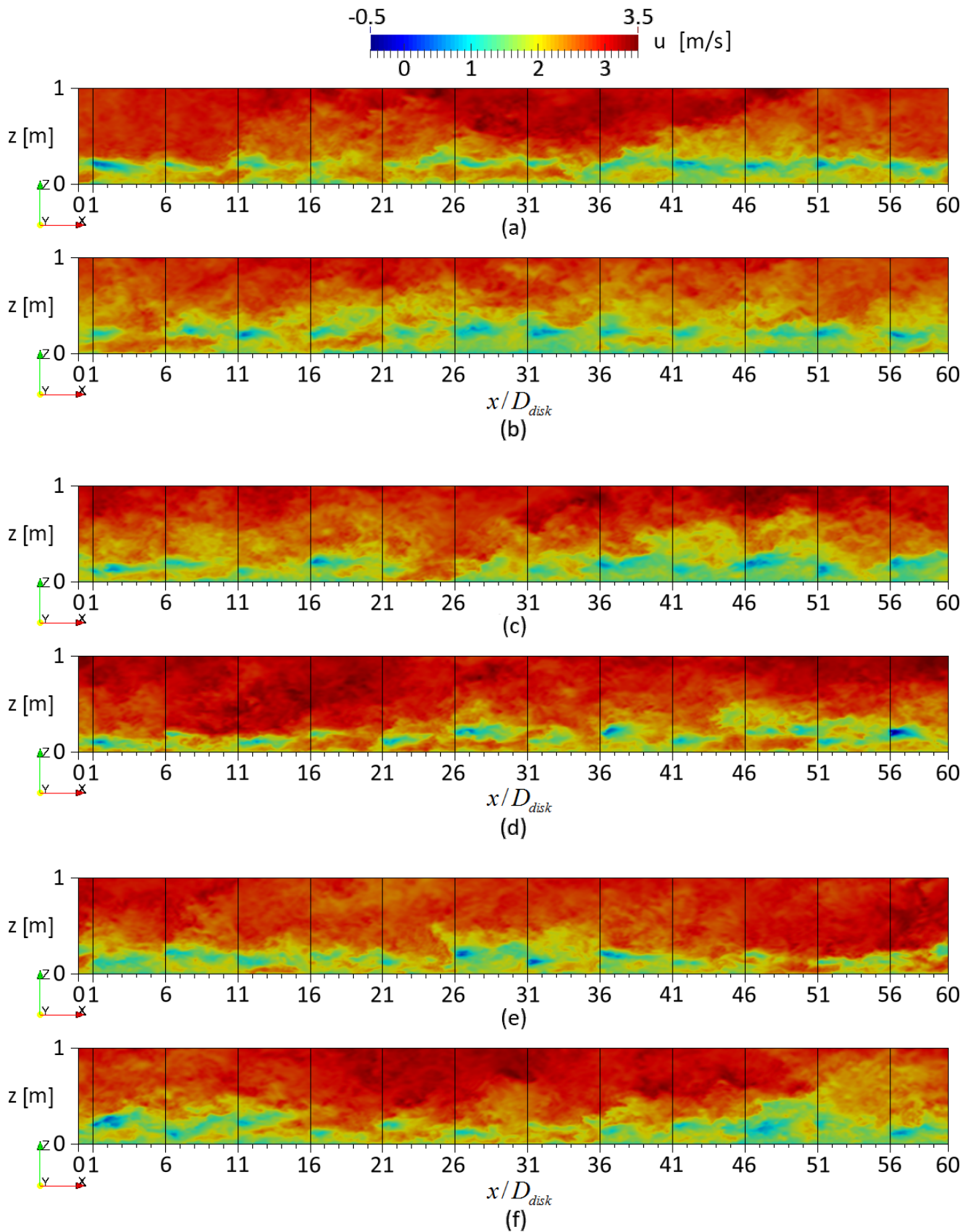


Figure 5.12: Instantaneous flow-field of streamwise velocity, xz -section in the turbine midplane.
 (a) 2h at column 3, (b) 2h at column 4, (c) RA at column 3, (d) RA at column 4, (e) SA at column 3, (f) SA at column 4.

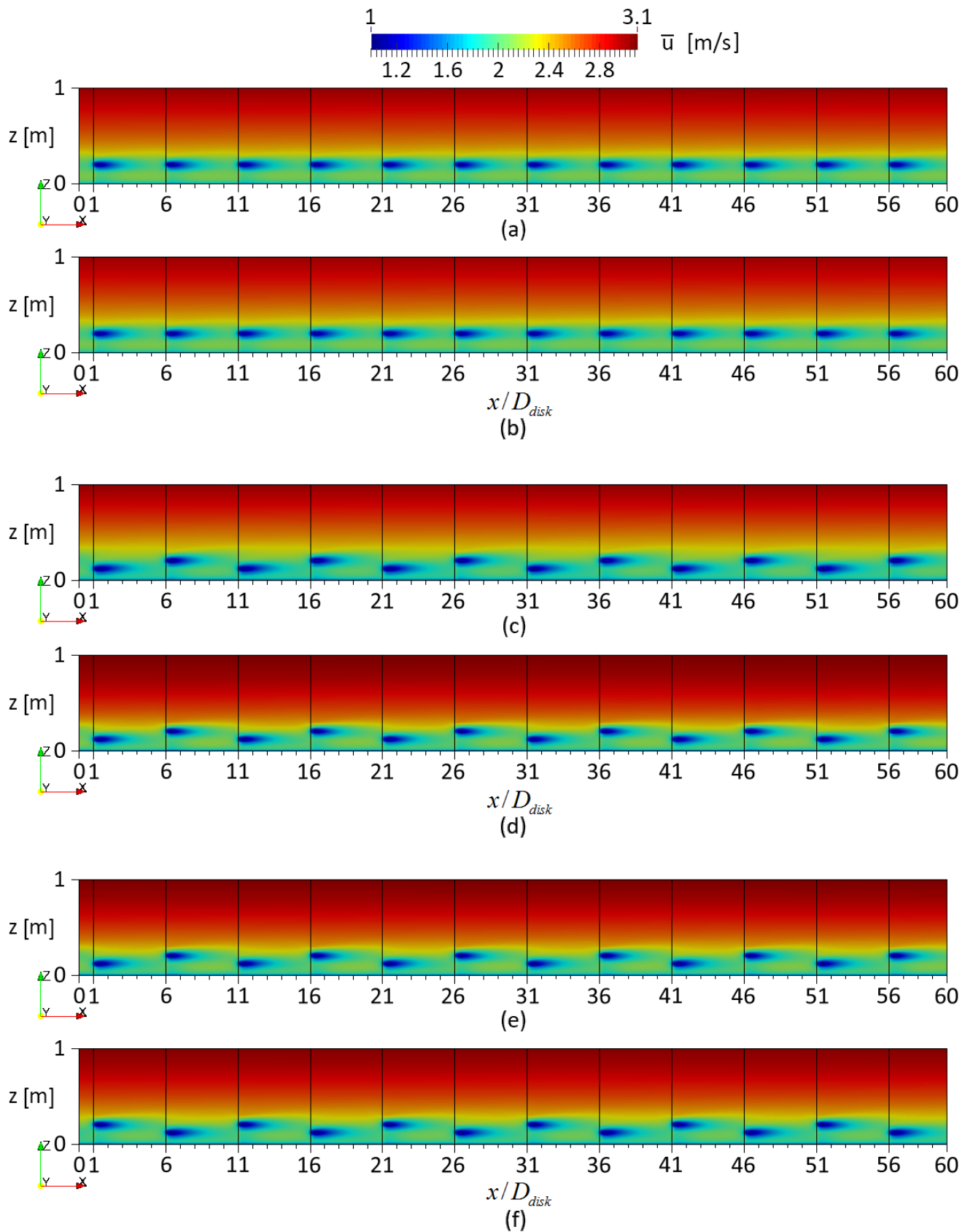


Figure 5.13: Time-averaged flow-field of streamwise velocity, xz -section in the turbine midplane. (a) 2h at column 3, (b) 2h at column 4, (c) RA at column 3, (d) RA at column 4, (e) SA at column 3, (f) SA at column 4.

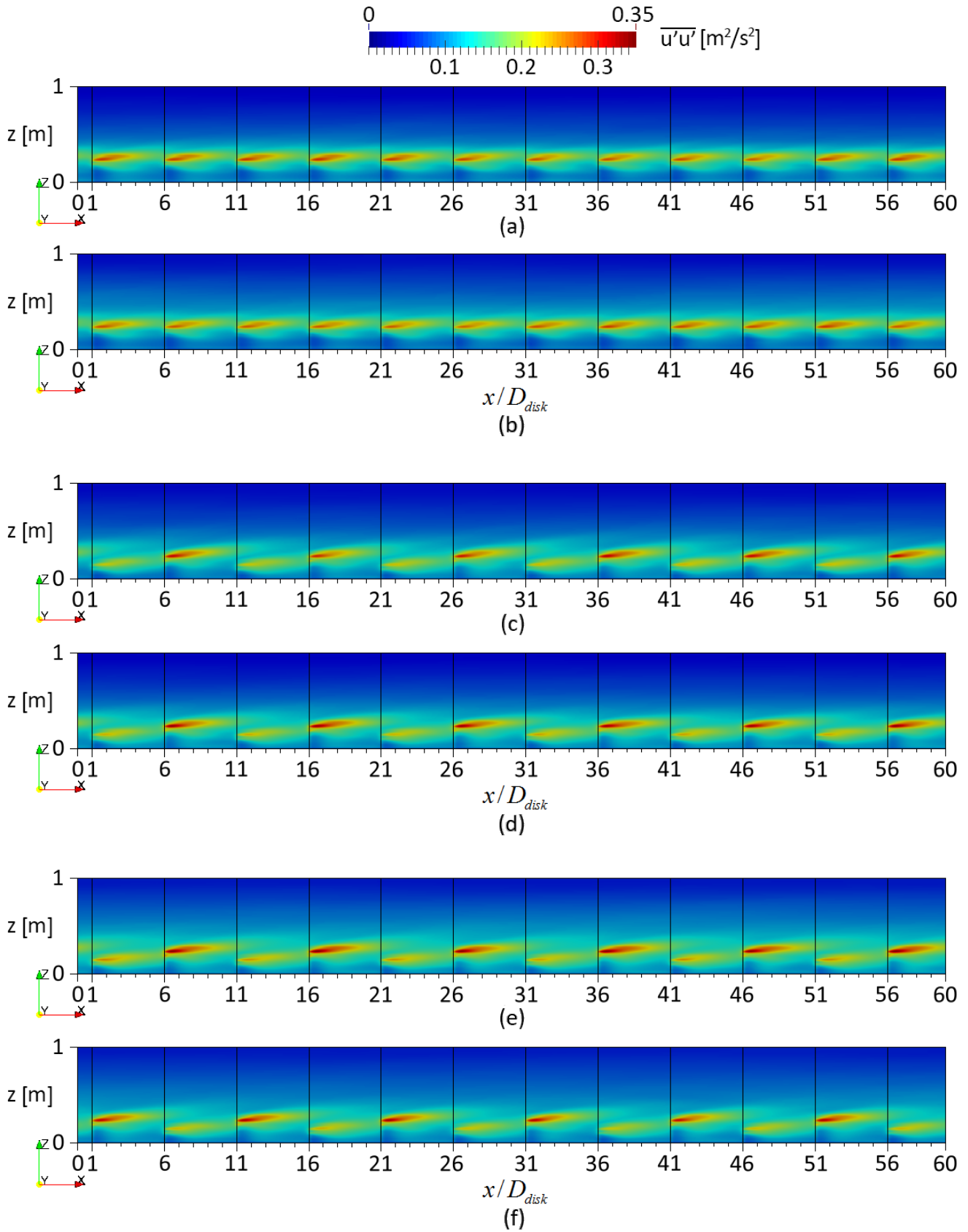


Figure 5.14: Time-averaged flow-field of Reynolds stress $\overline{u'u'}$, xz -section in the turbine midplane. (a) 2h at column 3, (b) 2h at column 4, (c) RA at column 3, (d) RA at column 4, (e) SA at column 3, (f) SA at column 4.

Chapter 6

Conclusions

Recalling the main research question and its sub questions as defined in the introduction:

How is the power production, the fluctuation of power production and the fatigue life affected by application of tower height alternation for an infinite wind farm imposed by a neutrally stratified half-channel boundary layer?

Sub questions:

- *What tower height difference is appropriate and optimal?*
- *What wind farm configurations to consider and is there a performance difference between configurations?*
- *Are the physics as proposed by Johnstone and Coleman (2012) valid for such application?*

Regarding the physics as proposed by Johnstone and Coleman (2012), the occurrence of the following is discussed: local and overall TKE production and a sawtooth curve for the Reynolds shear stress magnitude.

A LES approach was selected by application of DALESURBAN. To model wind turbines, the non-uniform actuator disk model (NU-ADM) was selected and its implementation into DALESURBAN described. The NU-ADM is verified and validated within an infinite (double-periodic) and neutrally stratified half-channel boundary layer. Here, the pressure difference driving the simulation was proven to have a significant effect when comparing results with experimental measurements. Nevertheless, good agreement with validation measurements from literature was found.

To determine the appropriate and optimal tower height difference, two wind turbines with varying tower heights were placed behind each other within an infinite (double-periodic) domain and imposed by a neutrally stratified half-channel boundary layer. Simulating a multitude of varying tower height differences gave no conclusive optimum, while the physics as proposed by Johnstone and Coleman (2012) [18] could not be verified for any of the considered cases. One tower height difference was selected for further advancements, corresponding to $z_{hub,low} = 0.125m$ and $z_{hub,high} = 0.2125m$. Furthermore, three wind farm configurations were considered:

1. High turbines only (2h).
2. Tower heights alternating in row configuration (RA) (figure 5.6).
3. Tower heights alternating in staggered configuration (SA) (figure 5.7).

Each wind farm configuration consisted of 12 turbines in a column and 6 turbines in a row, resulting in a domain length of $60D_{disk}$ and a domain width of $30D_{disk}$. To conclude on the performance difference between wind farm configurations, the results for the power production, the fluctuation of power production and the fatigue life are summarized.

An increase in power production of about 4.658% to 4.692% compared with the 2h-case for the RA and SA configuration was found, respectively. Contrary to what is expected from the physics as proposed by Johnstone and Coleman (2012), the local and overall TKE production increases and no sawtooth curve for the Reynolds stress is found. Furthermore, any increase in power production appeared to be mainly caused by the decrease in tower drag surface. On the fluctuation of power production, an increase of the standard deviation of about 5 to 34% for all high turbines in the alternating configurations relative to the 2h-case was found. For the low turbines, the fluctuation of power production remained approximately unchanged. Furthermore, it was found that the SA configuration experienced a larger increase in fluctuation than the RA configuration. Regarding cross-correlations between turbines a decrease in the correlation between turbines in the same column but in a different row was found. Only for the SA configuration, an increase in the correlation between turbines in different columns was found. Regarding fatigue, when comparing the alternation configurations with the 2h-case various results are relevant:

- The increase in fluctuation of power production of the high turbines.
- Increased TKE production and thus overall, the flow is more turbulent (higher Reynolds stresses).
- Flow fields gave a decreased $\overline{u'u'}$ Reynolds stress directly in front of each turbine (low and high). Simultaneously, an increased production of $\overline{u'u'}$ Reynolds stress near the actuator disk edge for the high turbines was found.

Although the turbulence directly in front of each turbine is lower, other statements (of the above) point to a decrease in fatigue life for high turbines in the alternation configurations. Furthermore, for the low turbines in the alternation configurations there is not enough evidence of any improvement compared with the high turbines in the 2h-case. This result also indicates a difference in the fatigue life of the high and low turbines.

To finally conclude on the sub questions:

- An appropriate tower height difference could not be determined as the proposed physics by Johnstone and Coleman (2012) [18] could not be verified for any of the considered cases. Therefore, definition of an optimal tower height remains inconclusive.
- The difference in power production between the two alternation configurations was found to be insignificant. Furthermore, the SA configuration experienced a stronger fluctuation of the power production and correlations between turbines were stronger overall when compared to the RA configuration. Regarding fatigue, there is weak evidence of a shorter fatigue life for the SA configuration compared to the RA configuration. This is based on the slightly higher TKE production, fluctuation of power production and $\overline{u'u'}$ Reynolds stress for the SA configuration.
- The physics proposed by Johnstone and Coleman (2012) [18] have been found to be incorrect for infinite wind farms with alternating tower heights imposed by a neutrally stratified half-channel boundary layer.

To finally conclude on the main research question: although an increased power production for the alternation configurations is found, the source for this increase is primarily the decrease of overall tower drag surface. The quantified increase is of the order of 4% to 5%, however due to simplistic modeling of the tower and its unexpected large influence, the found increase is highly uncertain and is most likely not of such significant magnitude. Furthermore, the fluctuation of the power production increases and the fatigue lives of the high turbines is expected to decrease. Additionally, as an undesirable side-effect, in the alternation configurations the fatigue life for the high turbines is found to be shorter than for the low turbines.

Chapter 7

Recommendations and future research

Equation 7.1 recalls the force balance as derived in section 3.4.4 and is only valid for steady-state double-periodic domains with free-slip conditions for the top boundary. Here, F_x contains the turbine force, tower drag force and nacelle drag force on the flow.

$$\left[\frac{\Delta p_{mod}}{L_x} \right] L_z = \frac{1}{\rho} \left(\sum^{N_{wt}} \overline{F_x} + \overline{\tau_x} \right) \quad (7.1)$$

The force balance indicates a strong relation between the pressure difference and the resulting forces of the turbine. Produced power is related to turbine force by the reference velocity as found in equation 3.18 and simultaneously, the turbine force is related to the reference velocity. An increase of the power production thus requires an increase in the turbine force. Due to a fixed pressure difference driving the flow, there are a limited number of ways to achieve this:

- Decrease in tower drag.
- Decrease in nacelle drag.
- Decrease in shear near the wall, τ_x

In hindsight it is thus not surprising that the increase in power production due to tower height alternation is mainly caused by a decrease in tower drag surface. Additionally as a result thereof, the physics proposed by Johnstone and Coleman (2012) [18] are not applicable for infinite wind farms.

For future research it is therefore recommended to use an inflow-outflow model description. In such model description the inflow is undisturbed by wind turbines and thus all developmental effects occurring within the wind farm are taken into account. Furthermore, the outflow is not returned to the inflow as was the case for the infinite wind farm and the pressure difference is set at zero (or some physical low). Therefore, the produced power is not dependent on the set pressure difference. Rather, the dependency of the produced power is on the ability of the boundary layer to transfer kinetic energy to the wind turbines. For the inflow-outflow model description it is thus interesting to re-investigate the validity of the physics proposed by Johnstone and Coleman (2012) [18]. Additionally, it is interesting to repeat the investigation into the optimal tower height difference for the inflow-outflow model description. For this investigation a larger domain than applied in the current study is however recommended due to developmental effects.

Bibliography

- [1] E. Achenbach. Distribution of local pressure and skin friction around a circular cylinder in cross-flow up to $Re = 5e6$. *Journal of Fluid Mechanics*, 34:625–639, 1968.
- [2] International Energy Agency. Long-term research and development needs for wind energy for the time frame 2000 to 2020. *Ad Hoc Group Report to the Executive Committee*, 2001.
- [3] R.J. Barthelmie, L. Folkerts, G.C. Larsen, K. Rados, S.C. Pryor, and S.T. Frandsen. Comparison of wake model simulations with offshore wind turbine wake profiles measured by sodar. *Journal of Atmospheric and Oceanic Technology*, 23:888–901, 2006.
- [4] M. Calaf, C. Meneveau, and J. Meyers. Large eddy simulation study of fully developed wind-turbine array boundary layers. *Physics of Fluids*, 22, 2010.
- [5] L.P. Chamorro and F. Porté-Agel. Flow characterization of wind-turbine wake(s) developed in a boundary layer flow with different thermal stratifications: A wind-tunnel study, 2010.
- [6] P.K. Chaviaropoulos and M.O.L. Hansen. Investigating three-dimensional and rotational effects on wind turbine blades by means of a quasi-3d navier-stokes solver. *Journal of Fluids Engineering*, 122(June 2000):330–336, 2000.
- [7] Ying Chen, Hua Li, Kai Jin, and Y. Elkassabgi. Investigating the possibility of using different hub height wind turbines in a wind farm. *International Journal of Sustainable Energy*, 2015.
- [8] Ying Chen, Hua Li, Kai Jin, and Qing Song. Wind farm layout optimization using genetic algorithm with different hub height wind turbines. *Energy Conversion and Management*, 70:56–65, 2013.
- [9] D. Coles. The law of the wake in the turbulent boundary layer. *Journal of Fluid Mechanics*, 1:191–226, 1956.
- [10] Global Wind Energy Council. Global statistics, 2014.
- [11] M. Drela. Xfoil: An analysis and design system of low reynolds number airfoils. *Conference on low Reynolds number airfoil aerodynamics*, 1989.
- [12] S. Emeis. A simple analytical wind park model considering atmospheric stability. *Wind Energy*, 13(5):459–469, 2010.
- [13] J.H. Ferziger and M. Perić. *Computational Methods for Fluid Dynamics*. Springer, 2002.
- [14] S. Frandsen. On the wind speed reduction in the center of large clusters of wind turbines. *Journal of Wind Engineering and Industrial Aerodynamics*, 39(13):251–265, 1992.
- [15] S.T. Frandsen, RR Barthelmie, S.C. Pryor, O. Rathmann, S. Larsen, J. Højstrup, and M. Thøgersen. Analytical modelling of wind speed deficit in large offshore wind farms. *Wind Energy*, 9(1-2):39–53, 2006.
- [16] G. Gross. A simple analytical wind park model considering atmospheric stability. *Meteorologische Zeitschrift*, 19(1):91–99, 2010.

- [17] J.F. Herbert-Acero, J.R. Franco-Acevedo, M. Valenzuela-Rendón, and O. Probst-Oleszewski. Linear wind farm layout optimization through computational intelligence. In *MICAI 2009: Advances in Artificial Intelligence*, volume 5845 of *Lecture Notes in Computer Science*, pages 692–703. Springer Berlin Heidelberg, 2009.
- [18] R. Johnstone and G.N. Coleman. The turbulent ekman boundary layer over an infinite wind-turbine array. *Journal of Wind Engineering and Industrial Aerodynamics*, 100(1):46–57, 2012.
- [19] I. Katic, J. Hojstrup, and N.O. Jensen. A simple model for cluster efficiency. *European Wind Energy Association Conference and Exhibitions*, pages 407–410, 1986.
- [20] London Array LTD. The london array project, 2015.
- [21] T.S. Lund, X Wu, and K.D. Squires. Generation of turbulent inflow data for spatially-developing boundary layer simulations. *Journal of Computational Physics*, 140(2):233–258, 1998.
- [22] J.F. Manwell, G.J. McGowan, and A.L. Rogers. *Wind Energy Explained, theory, design and application*. John Wiley & Sons LTD., 2002.
- [23] P.J. Mason and N.S. Callen. On the magnitude of the subgrid-scale eddy coefficient in large-eddy simulations of turbulent channel flow. *Journal of Fluid Mechanics*, 162:439 – 462, 1986.
- [24] D. Medici and P. H. Alfredsson. Measurements on a wind turbine wake: 3d effects and bluff body vortex shedding. *Wind Energy*, 9(3):219–236, 2006.
- [25] D. Medici and P. H. Alfredsson. Measurements behind model wind turbines: further evidence of wake meandering. *Wind Energy*, 11(2):211–217, 2008.
- [26] D. Mehta, A.H. van Zuijlen, B. Koren, J.G. Holierhoek, and H. Bijl. Large eddy simulation of wind farm aerodynamics: A review. *Journal of Wind Engineering and Industrial Aerodynamics*, 133:1 – 17, 2014.
- [27] F. Menter. Cfd best practice guidelines for cfd code validation for reactor-safety applications. *European Commission: 5th Euratom framework programme*, pages 11–27, 2002.
- [28] R Mikkelsen. *Actuator disk methods applied to wind turbines*. PhD thesis, Technical University of Denmark, 2003.
- [29] A. Miller, B. Chang, R. Issa, and G. Chen. Review of computer-aided numerical simulation in wind energy. *Renewable and Sustainable Energy Reviews*, 25:122–134, 2013.
- [30] F.T.M Nieuwstadt. *Turbulentie, inleiding in de theorie en toepassingen van turbulente stromingen*. Epsilon Uitgaven, Utrecht, 1992.
- [31] F. Porté-Agel, Hao Lu, and Yu-Ting Wu. Interaction between large wind farms and the atmospheric boundary layer. *Procedia {IUTAM}*, 10(0):307 – 318, 2014.
- [32] F. Port-Agel, Yu-Ting Wu, Hao Lu, and J.R. Conzemius. Large-eddy simulation of atmospheric boundary layer flow through wind turbines and wind farms. *Journal of Wind Engineering and Industrial Aerodynamics*, 99(4):154–168, 2011. The Fifth International Symposium on Computational Wind Engineering.
- [33] P.E. Réthoré. *Wind turbine wake in atmospheric turbulence*. PhD thesis, Aalborg University, 2009.
- [34] B. Sanderse, S.P. van der Pijl, and B. Koren. Review of computational fluid dynamics for wind turbine wake aerodynamics. *Wind Energy*, 14:799–819, 2011.
- [35] A. Scotti, C. Meneveau, and D.K. Lilly. Generalized smagorinsky model for anisotropic grids. *Physics of Fluids A: Fluid Dynamics (1989-1993)*, 16(9):2306–2308, 1993.

- [36] W.Z. Shen, J.H. Zhang, and J.N. Sørensen. The actuator-surface model: a new navier-stokes based model for rotor computations. *Journal of Solar Energy Engineering*, 131(1), 2009.
- [37] J.N. Sørensen and C.W. Kock. A model for unsteady rotor aerodynamics. *Journal of Wind Engineering and Industrial Aerodynamics*, 58(3):259–275, 1995.
- [38] B.H. Thacker, S.W. Doeblinkg, F.M. Hemez, M.C Anderson, J.E. Pepin, and E.A Rodriquez. *Concepts of Model Verification and Validation*. Los Alamos National Laboratory, 2004.
- [39] L.J. Vermeer, J.N. Sørensen, and A. Crespo. Wind turbine wake aerodynamics. *Progress in Aerospace Sciences*, 39:467–510, 2003.
- [40] A.W. Vreman. An eddy-viscosity subgrid-scale model for turbulent shear flow: Algebraic theory and applications. *Physics of Fluids*, 16:3670–3681, 2004.
- [41] A.W. Vreman. Subgrid modeling in large-eddy simulation of complex flow. *ITI Conference on Turbulence*, 2006.
- [42] H. Werner and H. Wengle. Large-eddy simulation of turbulent flow over and around a cube in a plate channel. *Eighth symposium on turbulent shear flows*, 1991.
- [43] M.F. White. *Fluid Mechanics*. McGRAW-HILL International Editions, 1999.
- [44] Yu-Ting Wu and F. Port-Agel. Large-eddy simulation of wind-turbine wakes: Evaluation of turbine parametrisations. *Boundary-Layer Meteorology*, 138(3):345–366, 2011.
- [45] Y. Zhou, Md. Mahbub Alam, H.X. Yang, H. Guo, and D.H. Wood. Fluid forces on a very low reynolds number airfoil and their prediction. *International Journal of Heat and Fluid Flow*, 32(1):329–339, 2011.

Appendix A

List of Symbols

Symbol	Dimension	Explanation
a	–	Axial induction factor
A	m^2	Area
ARC	–	Asymptotic Range of Convergence
B	–	Number of blades
c	–	Blade chord
C	–	Coefficient
d	–	Distance
D	m	Diameter
DIM	-	Spatial dimension
e	m^2/s^2	Energy
\mathbf{e}	–	Directional unit vectors
E	–	Any error
\mathcal{E}	m^2/s^3	Kinetic energy extraction
EV	–	Expected value
f	m^2/s^2	Skin friction
F	N	Cartesian force vector
\mathcal{F}	m^2/s^2	Smoothed turbine force
G	–	Guassian filter-kernel
GCI	–	Grid convergence index
h	–	Grid spacing in any direction
k	–	Wake decay constant
L	m	Length
M	m/s^2	Momentum
n	–	Blade element
N	–	Number of..
p	Pa	Pressure

P	W	Power
\mathcal{P}	m^2/s^3	Turbulent kinetic energy production
Pe	—	Peclet number
q	—	Order of convergence
Q	—	Rotation matrix
r	—	Local radius
R	—	Ratio
Re	—	Reynolds number
Rem	m/s^2	Collective term for remaining Navier-Stokes terms
s	%	Sensitivity
S	$1/s$	Fluid strain
SGS	m^2/s^2	Subgrid-scale energy
$SGSE$	%	Subgrid-scale energy percentage
$STAT$	—	Stationarity
t	s	Time
T	s	Period
\mathcal{T}	m^2/s^3	Kinetic energy transport or some time-scale (s)
u	m/s	Streamwise velocity
U	m/s	Relative velocity to blade
v	m/s	Spanwise velocity
V	m^3	Volume
w	m/s	Wall-normal velocity
\mathcal{W}	m^2/s^3	Kinetic energy work
x	m	Streamwise position
y	m	Spanwise position
z	m	Wall-normal position

Greek

Symbol	Dimension	Explanation
α	<i>radians</i>	Angle of attack
β	<i>radians</i>	Angle of cell on actuator disk to horizontal reference through disk center
γ	—	Area-factor
δ	m	Boundary layer height or Kronecker delta
ϵ	—	Regularization kernel
ζ	—	Efficiency
η	—	Regularization filter
θ	<i>radians</i>	Pitch angle

κ	–	Von Karman constant
λ	–	Tipspeed-ratio
μ	–	Mean
ν	m^2/s	Kinematic viscosity
Π	–	Coles' wake law parameter
ρ	kg/m^3	Density
σ	–	Standard deviation
τ	m/s^2	Shear (subgrid)
ϕ	<i>radians</i>	Angle of relative wind
χ	–	Some arbitrary term, undefined
Ψ	–	Relative surface overlap
Ω	<i>rad/s</i>	Rotational speed

Subscripts

Symbol	Dimension	Explanation
0	–	Roughness
2D	–	Two-dimensional
3D	–	Three-dimensional
2h	–	High hub-height only
<i>a</i>	–	Blade element index
<i>alt</i>	–	Alternating
<i>d</i>	–	Drag
<i>distr</i>	–	Distribution
δ	–	To boundary layer
<i>e</i>	–	Eddie
<i>eff</i>	–	Effective
ϵ	–	Regularized by regularization kernel
<i>f</i>	–	Friction
<i>gen</i>	–	Generator
<i>i</i>	–	(Cell-integer of) streamwise direction
<i>j</i>	–	(Cell-integer of) spanwise direction
<i>k</i>	–	(Cell-integer of) wall-normal direction
<i>l</i>	–	Lift
<i>mod</i>	–	Modified
<i>p</i>	–	Pressure
<i>P</i>	–	Power
\perp	–	Perpendicular

\parallel	—	Parallel
r	—	Radial
red	—	Reduced
ref	—	Reference
rel	—	Relative
SSM	—	Shear stress magnitude
s	—	Smagorinsky
sgs	—	Subgrid
$stat, avg$	—	Statistical averaging
t	—	Turbine
T	—	Thrust
τ	—	Shear
v	—	Vreman
wc	—	Wall-clock
ω	—	To pitch
x	—	Streamwise direction
y	—	Spanwise direction
z	—	Wall-normal direction

Superscripts

Symbol	Dimension	Explanation
'	—	Fluctuation (Reynolds stress)
*	—	Prediction
c	—	Closest
loc	—	Local
m	—	Full time-step
n	—	Any Runge-Kutta time-step
r	—	Radial
$RK1$	—	Runge-Kutta time-step 1
$RK2$	—	Runge-Kutta time-step 2
RK	—	Runge-Kutta time-step
x	—	Axial

Others

Symbol	Dimension	Explanation
-	—	Time-averaged
$\langle \quad \rangle$	—	Spatially-averaged
\sim	—	Correction

Appendix B

Mixed tower height wind farms

Three publications on mixed tower height wind farms are known. A short description of the methods and results of these publications is further given.

Acero et al. (2009)

Acero et al. (2009) [17] performed a linear wind farm layout optimization for an in-outflow model with inflow conditions defined by the logarithmic law. For the optimization, a genetic algorithm is applied and the wind turbines are analytically modeled by Jensen's wake model [19] parameterized for a Repower MD77 turbine. The objective is to optimize the layout of a single column of turbines within a fixed length, whereas the free parameters for the optimization objective are: the number of turbines, the distances between the wind turbines and the wind turbine tower heights.

Two of the presented cases in Acero et al. (2009) [17] are relevant:

1. Constant tower height with equal turbine spacing.
2. Fully optimized configuration with mixed tower heights.

For the first case the tower height is set at 85m. For the second case an optimization is performed for a mixture of two tower heights: $z_{hub,low} = 50\text{m}$ and $z_{hub,high} = 85\text{m}$. Figure B.1 gives the optimized wind farm layout for the west-to-east direction for this case. The optimized configuration from figure B.1 does not show a consistent pattern and distance between turbines is unconventionally small at about 2 turbine diameters. Resulting power output of this optimized configuration of 7 turbines is about 10.4% higher than the configuration of case 1 with 6 turbines and equal spacing. A second mixed tower height optimization is performed with $z_{hub,low} = 85\text{m}$ and $z_{hub,high} = 120\text{m}$. Instead of positioning turbines lower than case 1, turbines are set higher. Also, the number of turbines to optimize is now limited to 6 to ensure an equal number of turbines as in case 1. An increase of 24.2% in power production is found compared with case 1.

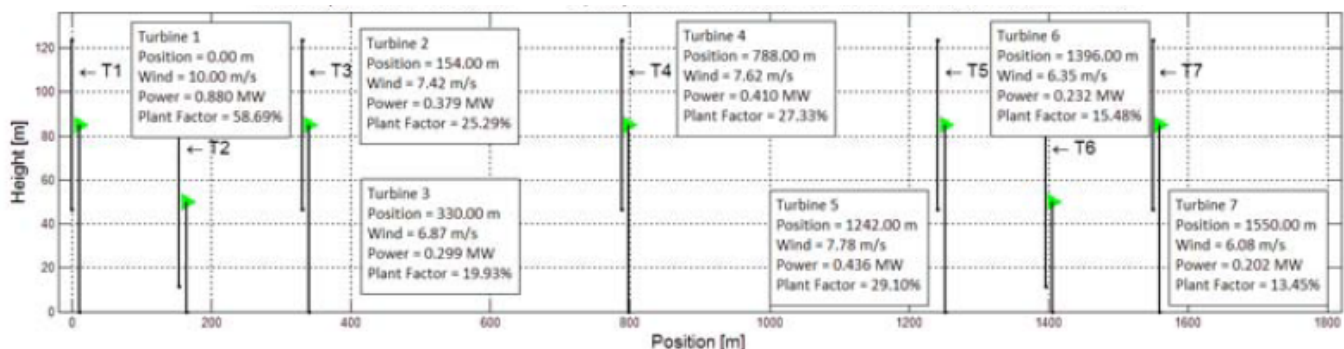


Figure B.1: Optimized wind farm layout for a mixture of two tower heights for the west-to-east regime (modified from [17]).

Ying Chen et al. (2015)

Ying Chen et al. (2013) [8] and Ying Chen et al. (2015) [7] also investigated the wind farm optimization by application of the genetic algorithm. Again, the wind turbines are modeled by Jensen's wake model [19] and inflow conditions are driven by the logarithmic law while no turbulence is considered. In Ying chen et al. (2015) [7] a 1D wind farm optimization is performed over a length of 2km for two cases:

1. Genetic algorithm on a grid of 200mx200m
2. Genetic algorithm on a grid of 25mx200m

A finer grid results in an improved freedom of optimization for the genetic algorithm. Two different tower heights are considered: $z_{hub,low} = 50\text{m}$ and $z_{hub,high} = 85\text{m}$. Power production of the optimized mixed tower height layout is 6% higher, while the number of turbines is significantly larger (8 to 6). For case 2, an increase in produced power is 12.4%, however some turbines are located within 25m (about 0.3 turbine diameters) behind each other.

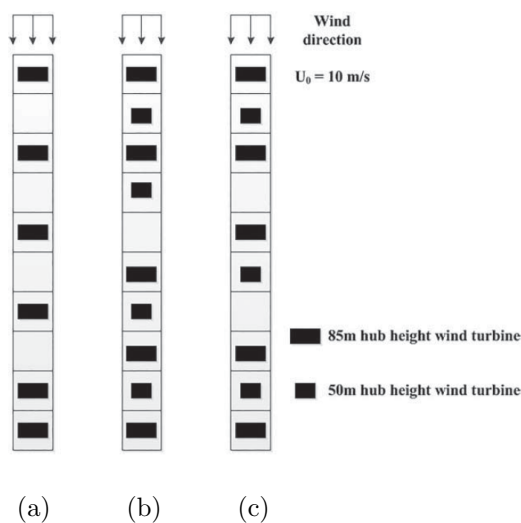


Figure B.2: Optimized wind farm layout for a mixture of two hub-eights for case 1 (modified from [7]). (a) High tower height only, (b) Optimal mixture of tower heights, (c) Optimal when minimal number of wind turbines is set as main driver.

Ying Chen et al. (2013)

In Ying Chen et al. (2013) [8] a 2D wind farm optimization is performed within a area of 500m and three cases are discussed:

1. Constant wind speed and direction
2. Constant wind speed and various directions
3. Various wind speeds and direction

Two tower heights are considered: $z_{tower,low} = 50\text{m}$ and $z_{tower,high} = 78\text{m}$. For the first case, compared with the optimized wind farm layout with only high turbines, an increase of 4% in power production was found by optimization for two different tower height turbines. Surprisingly, the number of low turbines was optimized as 5, to 20 high turbines. Furthermore, the optimized layout with only high towers contained 24 turbines, one less than the optimized layout with two different tower heights. For the second case the number of turbines for the optimized layouts is the same, while an increase of 7.3% is found due to the application of different tower heights. For the third case, an increase of 6.7% was found for the same number of turbines within the set area.

Appendix C

Validation measurements

The wind turbine model is validated based on the measurements performed by Chamorro and Porté -Agel [5]. Figure C.1 shows the normalized stream-wise velocity and figure C.2 shows the normalized turbulence intensity as defined by equation C.1, both measured over the midplane of the middle-row of the turbine array. The normalization value, u_{hub} , is defined as the stream-wise hub-velocity of the undisturbed flow, found to be 2.4 m/s.

$$\frac{\sigma_u}{u_{hub}} = \frac{\sqrt{u'u'}}{\bar{u}_{hub}} \quad (C.1)$$

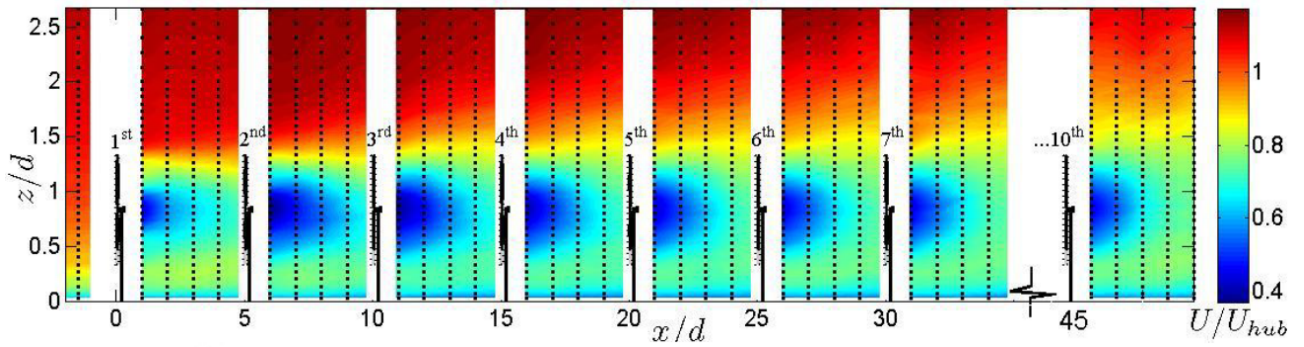


Figure C.1: Normalized stream-wise velocity [5].

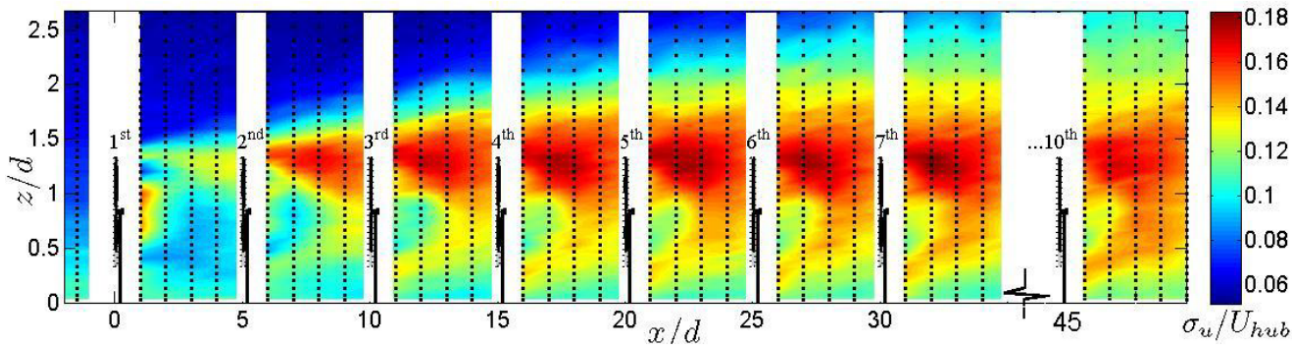


Figure C.2: Normalized turbulence intensity [5].

Figure C.3 shows multiple velocity profiles behind turbines downstream, these profiles will be thoroughly used for further validation of the model.

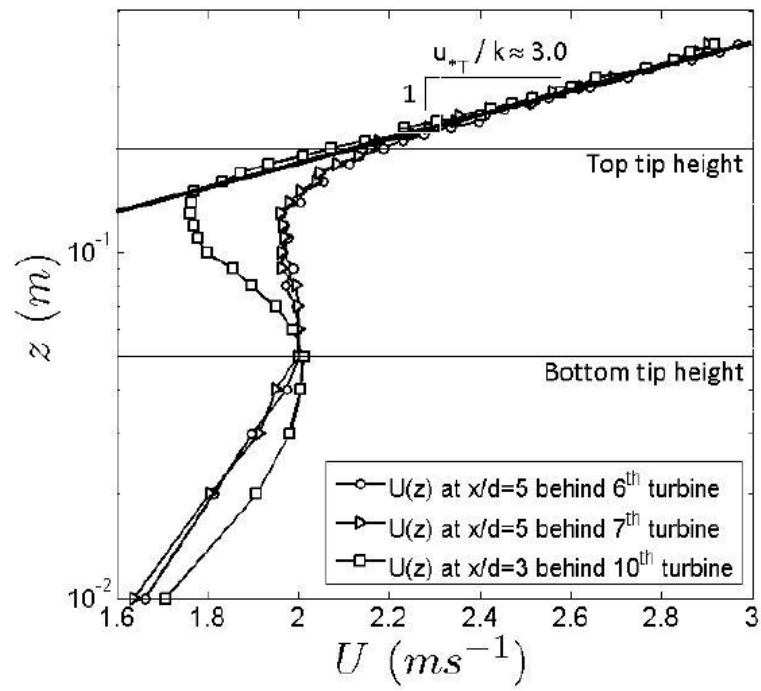


Figure C.3: Velocity profiles behind turbines in the near developed regime [5].

Figure C.4 gives the mean rotational speed of each turbine in the middle column.

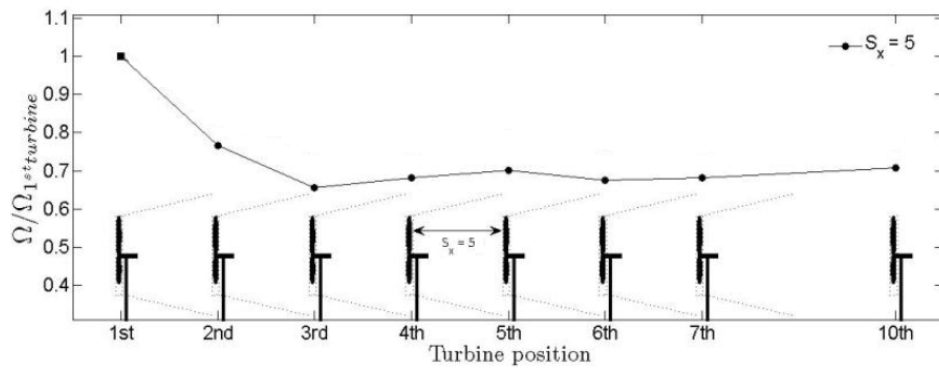


Figure C.4: Relative rotational speed (modified from [5]).

Appendix D

Known model inputs

The required model inputs regarding the blade geometry, the lift and drag coefficients and rotational speed are discussed. A summary of resulting model inputs is given in table 3.2.

D.1 Blade geometry

All turbines from the validation case are fitted with a GWS/EP-6030x3 propeller. In order to define the required blade geometric inputs for the determination of the lift and drag coefficients, geometric measurements on a two-bladed GWS/EP-6030 propeller were performed. Required measurements are the blade-element chord and pitch at different blade-element radii, all dependent on the chosen number of blade elements.

D.1.1 Number of blade elements (or annuli)

In order to ensure smoothness of the flow field, the number of blade elements is required to be grid dependent. It is found that coupling the number of blade elements with half the number of cells over the disk diameter, $N_{cells,disk}$, is an appropriate estimation. Figure D.1 compares the DALESURBAN result of the $\overline{u'u'}$ field of two simulations in the turbine midplane, (a) with $N_a/N_{cells,disk} = 3/24$ and (b) with $N_a/N_{cells,disk} = 12/24$. In (a) three shear layers corresponding with the three blade elements are clearly visible, while these disappear in (b) by increasing the number of blade elements.

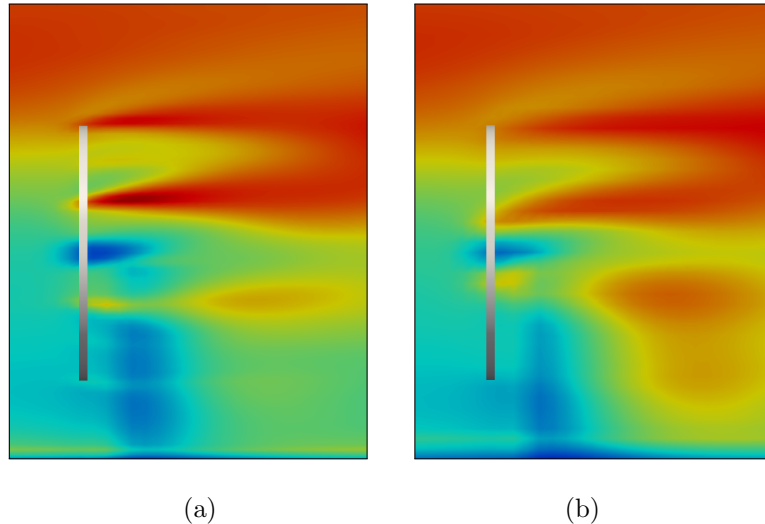


Figure D.1: $\overline{u'u'}$ field for:
(a) Low number of blade elements over a fine grid: $N_a/N_{cells,disk} = 3/24$
(b) High number of blade elements over a fine grid: $N_a/N_{cells,disk} = 12/24$

D.1.2 Blade measurements

The blade is cut at four measurements positions, painted orange and photographed, as found in figure D.2. Measurements are then performed on these photographs with the help of PTC Pro/Engineer Wildfire. Results of these measurements are found in table D.1.

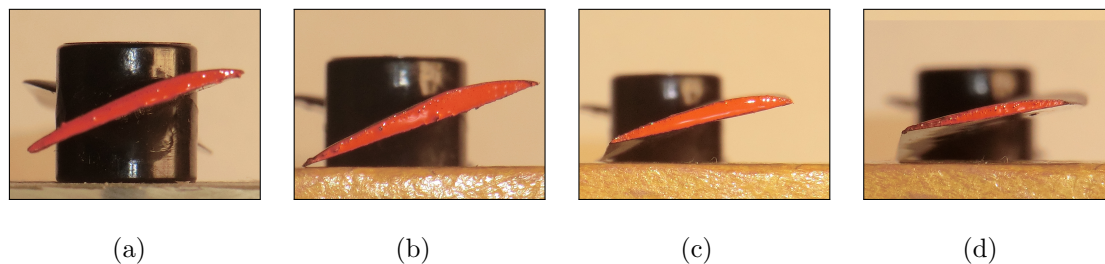


Figure D.2: Cross-sections of GWS/EP-6030 blade, note: figures not to scale, (a) Cross-section at BE-radius 17.0mm, (b) Cross-section at BE-radius 30.4mm, (c) Cross-section at BE-radius 50.8mm, (d) Cross-section at BE-radius 69.7mm

Table D.1: Blade geometry measurements.

BE-radius [mm]	BE-chord [mm]	BE-pitch [deg]
17.0	14.9	20.2
30.4	15.0	19.3
50.8	13.2	12.4
69.7	10.5	10.1

Measurements presented in figure D.2 and table D.1 are for a blade consisting of four blade elements only. As stated, the number of blade elements is set coupled to half the number of cells over the disk diameter. Therefore, the number of blade elements is grid dependent and the above measurements should be performed for each simulation using a unique number of blade elements. To suppress the need for a large number of blades to cut to determine these inputs, the blade is modeled as a surfaced 3D model using PTC Pro/Engineer Wildfire based on presented measurements. This model assumes one single cross-section, changing in all dimensions relative to chord length and following a pitch angle approximately linearly interpolated in between measured positions. The cross-section is based on the photographed section at a blade element radius of 30.4mm as found in figure D.2(b). Figure D.4 gives more detail of this model, while figure D.3 gives the main dimensions of the blade cross-section. The assumption of constant cross-section has been chosen for two reasons: first of all 3D modeling is easier, and secondly, this allows for one data-set of lift and drag coefficients valid for all blade elements.

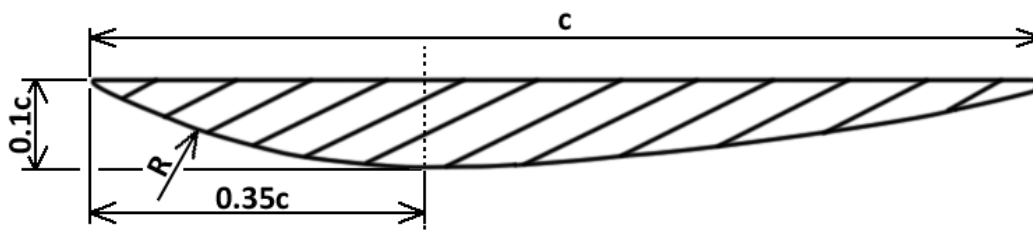


Figure D.3: Assumed constant cross-section of turbine blade.

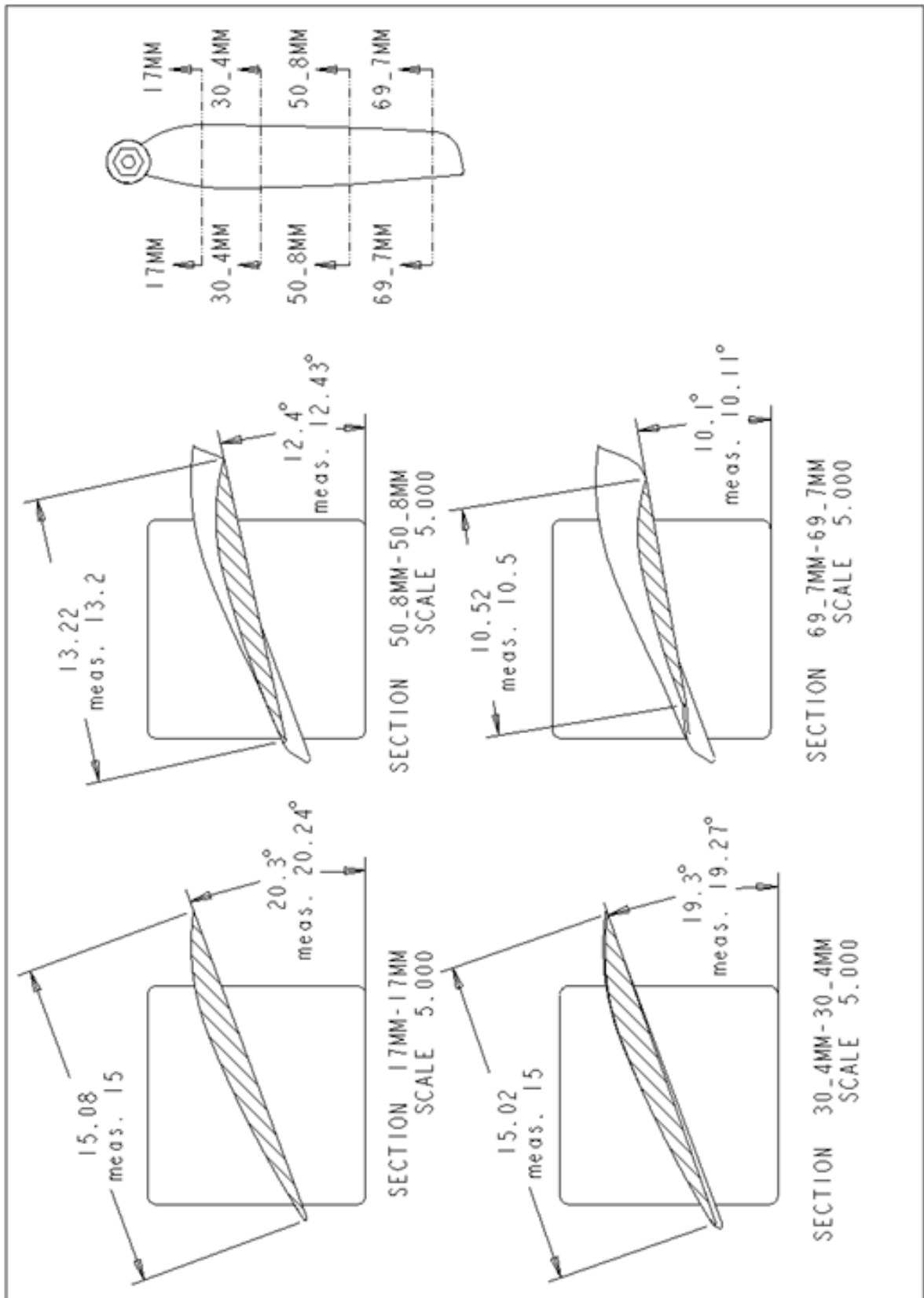


Figure D.4: Drawing of GWS/EP-6030 blade from PTC Pro/Engineer Wildfire 3D model.

D.2 Lift and drag coefficients

The lift and drag coefficients are part of the import data of the wind turbine model. Initially, lift and drag coefficients are found by XFOIL in a 2D environment. XFOIL is developed for the design and analysis of subsonic isolated airfoils to determine airfoil characteristics, and is based on a panel method. For more detail on the method of XFOIL, refer to the XFOIL methodology [11]. To correct for 3D effects such as rotation of the blade, the method of Chaviaropoulos and Hansen [6] is applied as described in equations D.1 and D.2.

$$C_{l,3D}(Re, \alpha) = C_{l,2D}(Re, \alpha) + 2.2 \left(\frac{c_a}{r_{disk}} \right) \cos^4(\theta_a) (C_{l,inv}(Re, \alpha) - C_{l,2D}(Re, \alpha)) \quad (D.1)$$

$$C_{d,3D}(Re, \alpha) = C_{d,2D}(Re, \alpha) + 2.2 \left(\frac{c_a}{r_{disk}} \right) \cos^4(\theta_a) (C_{d,2D}(Re, \alpha) - C_{d,2D}(Re, 0)) \quad (D.2)$$

The method of Chaviaropoulos and Hansen requires three inputs as function of the chord Reynolds number and angle of attack: the 2D lift coefficient $C_{l,2D}$, the 2D inviscid lift coefficient $C_{l,inv}$ and the 2D drag coefficient $C_{d,2D}$. These coefficients are imported as a look-up table for each combination and equidistant tick within a set range of Reynolds numbers and angles of attack. The wind turbine model then estimates the required 2D coefficients by means of two-sided linear interpolation over the four closest datasets available within this look-up table. The required range and set look-up table ticks are summarized in table D.2.

Table D.2: Estimated range of Reynolds numbers and angles of attack for determination of lift and drag coefficients.

	Unit	Min	Max	Tick
Reynolds number	-	0	10000	1000
Angle of attack	deg	-20	80	2

Within XFOIL, the cross-section as previously defined by figure D.3, is imported as custom profile by means of point data. This imported cross-section is slightly modified to optimize the number of panels and panel-angle by application of a rounded leading edge and an open trailing edge. The profile is paneled into a total of 400 panels with a maximum panel-angle of 34.6 degrees, as shown in figure D.5. The dark green line in figure D.5 represents the chord. The angle of attack is positive downwards and relative to this chord. For every calculated value, the pressure distribution is checked on smoothness to ensure proper calculation of the resulting 2D coefficients.

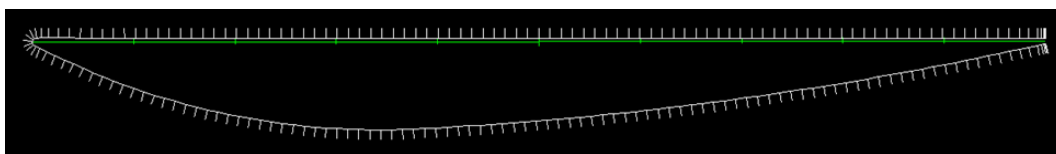


Figure D.5: Paneled cross-section used in XFOIL.

As the used profile is a custom profile, no validation measurements are available. Furthermore, XFOIL is not validated for low Reynolds numbers, let alone high numbers of angle of attack [11]. Measurements of any airfoil at such low Reynolds numbers and high angles of attack are scarce. One example is the experimental work by Y. Zhou [45] on a symmetric NACA0012 airfoil at $Re_c = 5300$ and an angle of attack ranging from 0 to 90 degrees. These measurements are used to assess XFOIL's error for these conditions. Figure D.6(a) gives a comparison of the lift coefficient between Zhou's measurements and XFOIL results of a NACA0012 airfoil and figure D.6(b) gives the XFOIL results for the custom profile at $Re_c = 5000$ and an angle of attack ranging from 0 to 80 degrees. Figures D.7(a) and D.7(b) give the same results for the drag coefficient.

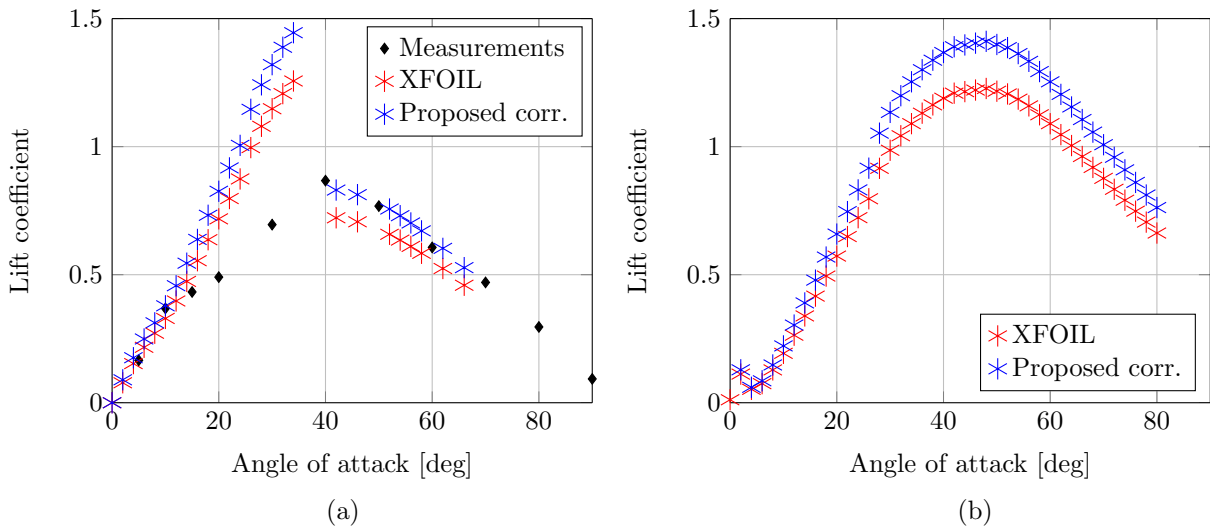


Figure D.6: (a) NACA0012 lift coefficients; XFOIL compared with measurements and proposed correction, (b) Custom profile lift coefficients from XFOIL and proposed correction.

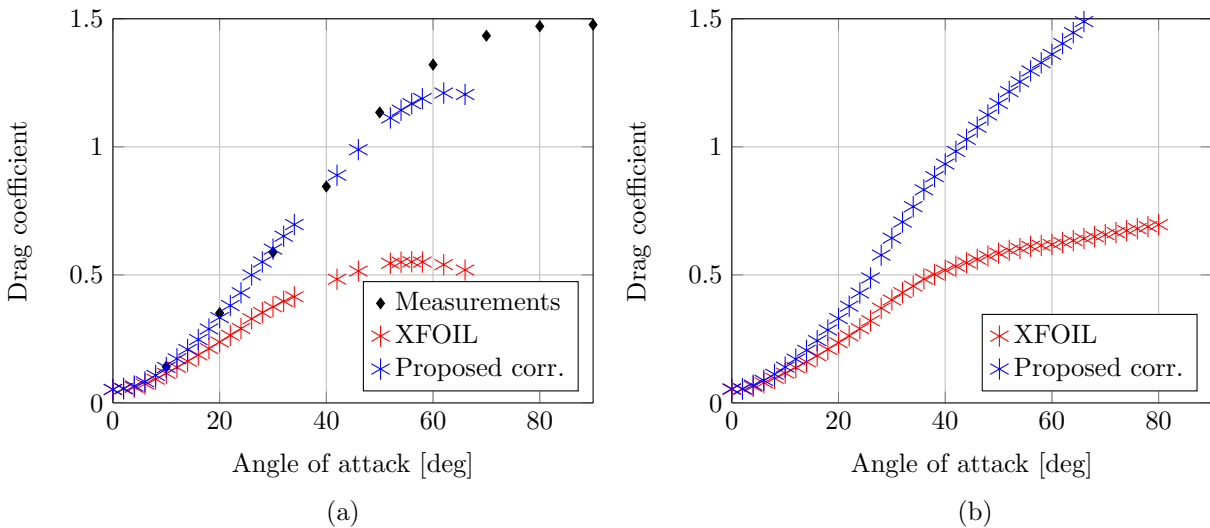


Figure D.7: (a) NACA0012 drag coefficients; XFOIL compared with measurements and proposed correction, (b) Custom profile drag coefficients from XFOIL and proposed correction.

For the NACA0012 profile, the measurements as shown in figure D.6(a) indicate a minor stall effect at a stall-angle of about 12 degrees. XFOIL overestimates the stall effect and the stall-angle, resulting in a large overestimation of the lift coefficient between 12 and 37 degrees of angle of attack. Past stall, the XFOIL results underestimate the lift coefficient by about 15%. The XFOIL results for the custom profile, as found in figure D.6(b), indicate a minor stall effect at a stall-angle of approximately 3 degrees. The custom profile is fully flat on one side resulting in a smaller stall angle due to increased leading edge separation. As overestimation of the stall angle appears not to be an issue with the custom profile, a fixed relative correction of +15% is proposed to compensate for XFOIL errors. Figure D.6(a) and (b) both show this proposed correction. For the drag coefficients, figure D.7(a) indicates a XFOIL underestimation increasing with the angle of attack. The XFOIL drag coefficient of the custom profile largely follows the same trend as the drag coefficients for the NACA0012 profile, as found in figure D.7(b). Assuming for the custom profile an identical error as for the NACA0012 profile, an empirical drag correction is proposed according to equation D.3.

$$C_{d,2D,corr} = C_{d,2D} \left(\frac{1}{50} \alpha + 1 \right) \quad (\text{D.3})$$

Lift and drag coefficient sensitivity

Three different cases are introduced to assess the model sensitivity to lift- and drag coefficients:

1. Using 2D lift and drag coefficients directly from XFOIL without any correction.
2. Using 2D lift and drag coefficients directly from XFOIL with 3D correction by method of Chaviaropoulos and Hansen [6].
3. Using 2D lift and drag coefficients from XFOIL with proposed corrections for 2D lift and drag coefficients and with 3D correction by method of Chaviaropoulos and Hansen [6].

All cases are run based on fully verified inputs. Table D.3 gives the time-averaged mean power production, reference velocity and power coefficient, each compared with case 1.

Table D.3: Time-averaged results of lift and drag sensitivity.

Case	\bar{P}_x [mW]	$\bar{u}_{ref,disk}$ [m/s]	\bar{C}_P [-]
1	24.69	2.031	0.244
2	-3.38%	-14.1%	+51.8%
3	-2.10%	-15.4%	+61.0%

Table D.3 indicates minor sensitivity to changes in lift and drag coefficients on power production, while reference velocity and power coefficients increase significantly. The first may be expected as power production is mainly dependent on set pressure difference as supported by the force balance from equation 3.38. Therefore, a more appropriate performance measures on the effect of the lift and drag coefficients is the power coefficient and it is stated that:

- The 3D correction method of Chaviaropoulos and Hansen has a significant influence on the performance of the turbine.
- The proposed XFOIL error correction increases the performance further, while its effect is minor relatively to the 3D correction method (+5.7% between case 2 and case 3).
- Therewith concluding: the 3D correction method of Chaviaropoulos and Hansen is applied for all cases, while the sensitivity to the proposed XFOIL error correction is too small to support further application.

D.3 Rotational speed

The rotational speed of the first turbine in the validation case is set at tip-speed ratio, λ , of 4 [31]. From the hub-velocity in front of the first turbine as given in appendix C, an estimation is made of the resulting rotational speed for the first turbine according to equation D.4.

$$\Omega_{1^{st}turbine} = \frac{\lambda u_{hub}}{2D_{disk}} \approx 112[\text{rad/s}] \quad (\text{D.4})$$

Figure C.4 gave an asymptote of about 0.65 relative rotation speed, or or 72.8 rad/s. Physically, the rotational speed is coupled with power production according to equation D.5.

$$\Omega = \frac{\zeta P_x}{\rho T_{gen}} \quad (D.5)$$

In equation D.5, ζ is the mechanical efficiency and T_{gen} is the generator torque corresponding to the rotational speed. As both P_x and T_{gen} are unknown from validation measurements, it is not possible to develop a dynamic function for Ω based on equation D.5. From available validation measurements, only the rotational speed as function of the stream-wise hub velocity can be approximated. Two sets can be approximated: $(u_{ref,disk}, \Omega) = (1.8, 72.8)$ and $(2.4, 112)$. Additionally, one set can be assumed based on the stream-wise reference velocity being zero, the rotational speed is zero: $(u_{ref,disk}, \Omega) = (0, 0)$

Based on these three sets a function is developed coupling the rotational speed with the reference velocity. First, the proportionality of this function is estimated. The generator is known to be a DC type for which $T_{gen} \propto \Omega$ holds for the greater part, i.e. torque increases linearly with rotational speed. Simultaneously, produced power on the generator side is directly proportional with Ω^2 , as $P_{gen} = T_{gen}(\Omega)\Omega$. Under the assumption of a constant thrust coefficient, the produced power on the turbine side is directly proportional to $u_{ref,disk}^3$, as $P_x = \frac{1}{2}\rho A_{disk}u_{ref,disk}^3 C_T^{loc}$. Assuming constant mechanical efficiency, equation D.6 holds.

$$P_x(u_{ref,disk}^3) \propto P_{gen}(\Omega^2) \quad (D.6)$$

Therefore, $\Omega^2 \propto u_{ref,disk}^3$, and thus the proportionality of the function coupling the rotational speed with the reference velocity may be estimated as $\Omega \propto u_{ref,disk}^{3/2}$. Equation D.7 gives the final function coupling the rotational speed with the reference velocity, found by fitting the defined proportionality with the approximated points. Figure D.8 plots the fit of equation D.7 through the approximated sets.

$$\Omega = 30u_{ref,disk}^{3/2} \quad (D.7)$$

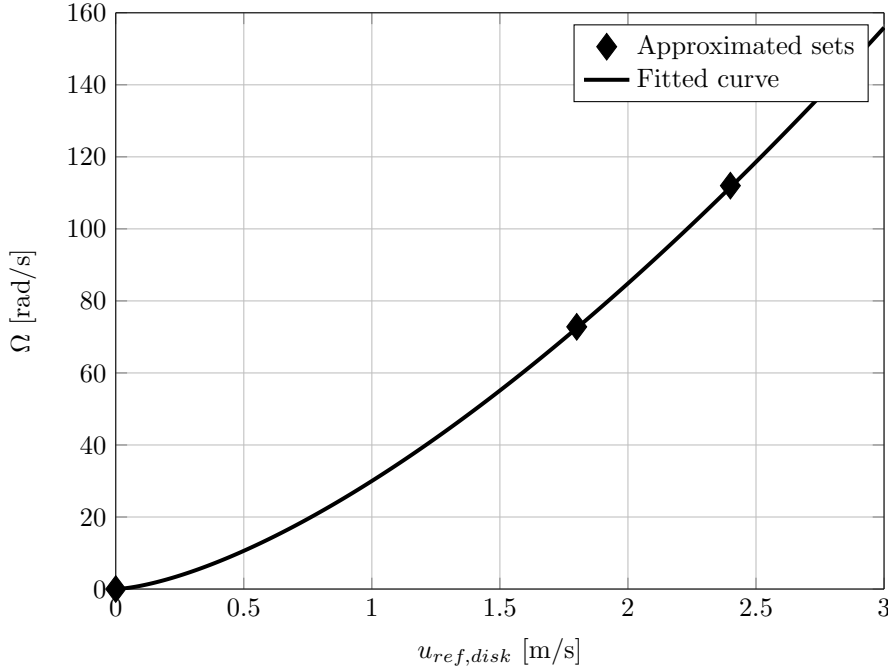


Figure D.8: Plot of fit through approximated sets.

Appendix E

Parameter estimation

The unknown model inputs are determined with respect to the selected validation case. Among others, the grid resolution is discussed by grid convergence study, all temporal parameters are defined and the subgrid model is chosen by comparison.

E.1 Grid convergence and sensitivity and smoothing

A study on grid sensitivity with respect to the NU-ADM has been performed by Porté-Agel (2011) [32]. Here, it was revealed that the NU-ADM can be used by placing no more than 5 to 7 grid points on the disk along the spanwise and wall-normal directions, while placing more points does not improve the results significantly. In the current study, grid convergence is performed in two steps to give control over the resulting time-step and magnitude of 2dx-waves:

1. x-grid convergence and sensitivity on the NU-ADM.
2. yz-grid convergence and sensitivity on the NU-ADM.

From the results of the first step, an x-grid is chosen for further advancement. Performance parameters are the spatial discretization error, the estimated wall-clock time and the magnitude of 2dx-waves. The second step assesses the proportional refinement of the y-grid and z-grid. For the mean power production, streamwise reference velocity and thrust / power coefficient, the spatial discretization error is determined by comparing simulation results with the 'exact' solution. This 'exact' solution is found according to Richardson extrapolation, as defined by E.1 [27]. Here, $R_{\text{effective}}$ is the effective grid refinement ratio as defined by equation E.2 with N total number of grid cells and DIM the number of dimensions in which grid refinement is performed. Furthermore, q is the order of convergence as defined by equation E.3. Finally, the relative solution error is defined by equation E.4. All numerical subscripts indicate a certain simulation number, with lower numbers corresponding to a finer grid. Furthermore, at least three different grids are required to estimate the exact solution by Richardson extrapolation.

$$\bar{P}_{x,exact} = \bar{P}_{x,1} + \frac{\bar{P}_{x,1} - \bar{P}_{x,2}}{R_{\text{effective}}^q - 1} \quad (\text{E.1})$$

$$R_{\text{effective}} = \left(\frac{N_1}{N_2} \right)^{1/DIM} \quad (\text{E.2})$$

$$q = \frac{\ln((\bar{P}_{x,3} - \bar{P}_{x,2}) / (\bar{P}_{x,2} - \bar{P}_{x,1}))}{\ln(R_{\text{effective}})} \quad (\text{E.3})$$

$$E = \frac{100 * (\bar{P}_{x,simulation} - \bar{P}_{x,exact})}{\bar{P}_{x,exact}} \quad (\text{E.4})$$

To determine whether or not the results exhibit convergence, the asymptotic range of convergence, ARC, is determined according to equation E.5, whereas convergence is achieved only if ARC approaches 1. Here, the GCI are the grid convergence indices which are determined using equations E.6 and E.7 [27]. Furthermore, the maximum sensitivity of the performance measure is defined according to equation E.8. This gives an indication of the maximum difference between the performance measures normalized by the normalized grid spacing, NGS. Here, a and b are levels of grid refinement with b always larger than a.

$$ARC = \frac{GCI_{23}}{R_{\text{effective}}^q GCI_{12}} \quad (\text{E.5})$$

$$GCI_{12} = \frac{1.25|(\bar{P}_{x,2} - \bar{P}_{x,1})/\bar{P}_{x,1}|}{(R_{\text{effective}}^q - 1)} \quad (\text{E.6})$$

$$GCI_{23} = \frac{1.25|(\bar{P}_{x,3} - \bar{P}_{x,2})/\bar{P}_{x,2}|}{(R_{\text{effective}}^q - 1)} \quad (\text{E.7})$$

$$s = \max\left(\frac{\bar{P}_{x,a} - \bar{P}_{x,b}}{\bar{P}_{x,\min(a,b)}} \frac{NGS_a}{NGS_b}\right) * 100 \quad (\text{E.8})$$

E.1.1 x-grid convergence and sensitivity

The following three grids are used to determine x-grid discretization error and sensitivity. Grids are chosen in accordance with an effective grid refinement ratio of 2 and the local subgrid energy of the coarsest grid is below 20% except for the near-wall region:

- $NGS(x) = 1$ $N_x = 192$ $N_y = 48$ $N_z = 48$ $N_{\text{cells,disk}} = 12$
- $NGS(x) = 2$ $N_x = 96$ $N_y = 48$ $N_z = 48$ $N_{\text{cells,disk}} = 12$
- $NGS(x) = 4$ $N_x = 48$ $N_y = 48$ $N_z = 48$ $N_{\text{cells,disk}} = 12$

All inputs are further set as previously defined by table 3.2. Furthermore, smoothing occurs only in the radial direction, with a width of zero, i.e. $N_{\text{smooth},r} = 0$; number of blade elements set as six; and all further unknown inputs as summarized in table 3.3. Table E.1 gives an overview of the exact solutions as found by Richardson extrapolation ($NGS(x)=0$), the x-grid discretization errors induced by each grid for each performance measure and an estimation of the wall-clock time relative to the finest grid, t_{wc} . Figure E.1 gives a graphical representation of the x-grid convergence.

Table E.1: x-grid discretization errors.

NGS(x)	\bar{P}_x	$\bar{u}_{ref,disk}$	\bar{C}_P	$t_{wc}/t_{wc,1}$
	[mW]	[m/s]	[-]	[-]
0	24.11	1.760	0.3684	-
1	-0.36%	-0.409%	-0.102%	1
2	-1.05%	-0.614%	-0.292%	1/4
4	-3.06%	-0.920%	-0.835%	1/16

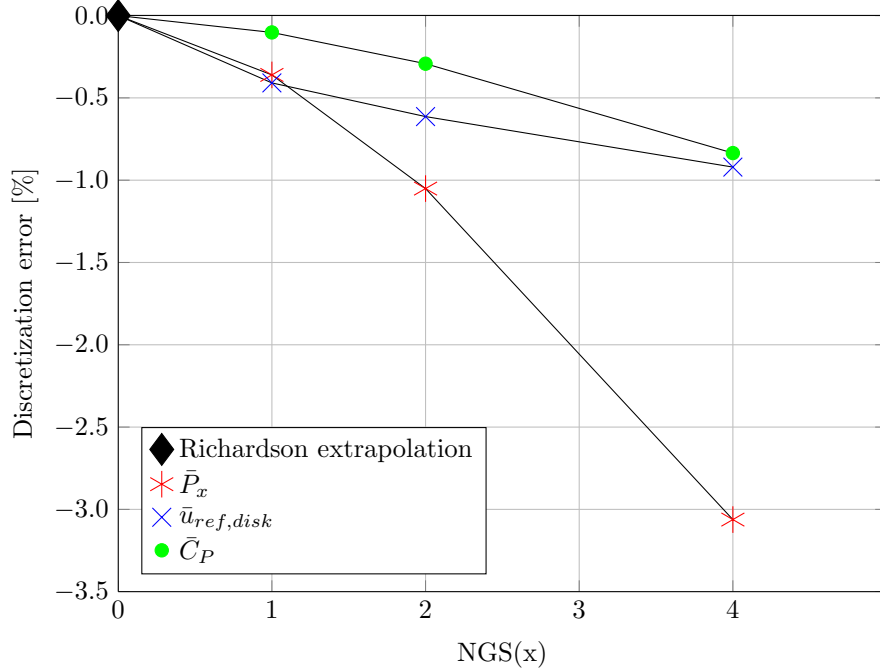


Figure E.1: Discretization errors as function of normalized grid spacing over x-grid refinement.

Figure E.1 exhibits grid convergence for the power production and the power coefficient, however, the convergence of the streamwise reference velocity appears unsatisfactory. Table E.2 gives the asymptotic ranges of convergence for the power production. Indeed, for the power production and power coefficient the asymptotic range of convergence approaches 1 and thus convergence is verified, while the streamwise reference velocity is not within the asymptotic range of convergence.

Table E.2: Asymptotic range of convergence and sensitivity of mean performance measures with respect to x-grid variation.

	\bar{P}_x	$\bar{u}_{ref,disk}$	\bar{C}_P
ARC	1.01	0.53	1.00
s	1.04%	0.155%	0.274%

Table E.2 also gives the sensitivity of the performance measures as a result of grid variation. Although no clear discretization error can be defined for the streamwise reference velocity, its sensitivity to grid variation is the smallest. Therefore, it is fair to assume that the discretization error of the streamwise reference velocity is always smaller than the discretization error of the produced power. The definition of the final x-grid is therefore only based on the discretization error of the produced power and the required wall-clock time.

The discretization error of the NGS(x)=4 grid for the produced power surpasses 3%, yet this is acceptable. Regarding wall-clock time, the NGS(x)=4 grid performs naturally optimal, however, coarseness of the NGS(x)=4 grid increases the magnitude of the 2dx-waves. Suppression of these waves is desired for the quality of the flow fields, while simultaneously, the NGS(x)=4 grid is too coarse to allow for suppression of 2dx-waves by axial smoothing of the wind turbine momentum sink. Therefore, the NGS(x)=2 grid is chosen for further advancements as this grid has an acceptable error, an acceptable wall-clock time and allows for 2dx-wave suppression by axial smoothing. See chapter E.1.3 for more details on axial smoothing.

E.1.2 yz-grid convergence and sensitivity

Three grids are introduced to determine yz-grid discretization error and sensitivity. Grids are chosen in accordance with an effective grid refinement ratio of 2 and the local relative subgrid energy of the coarsest grid is below 20% except for the near-wall region. The coarsest grid also corresponds with 6 cells over the disk diameter comparable to the statement by Porté-Agel (2011) on the number of required grid points on the disk [32]. The following grids are introduced:

- $NGS(y, z) = 1$ $N_x = 96$ $N_y = 96$ $N_z = 96$ $N_{cells,disk} = 24$
- $NGS(y, z) = 2$ $N_x = 96$ $N_y = 48$ $N_z = 48$ $N_{cells,disk} = 12$
- $NGS(y, z) = 4$ $N_x = 96$ $N_y = 24$ $N_z = 24$ $N_{cells,disk} = 6$

All inputs are set as previously defined by tables 3.2 and 3.3, however no axial smoothing is applied and for radial smoothing $N_{smooth,r} = 0$. Table E.3 gives the exact solutions as found by Richardson extrapolation ($NGS(y,z)=0$), the yz-grid discretization errors induced by each grid for each mean performance measure and an estimation of the wall-clock time relative to the finest yz-grid. Figure E.2 gives a graphical representation of the yz-grid convergence.

Table E.3: yz-grid discretization errors.

NGS(y,z)	\bar{P}_x	$\bar{u}_{ref,disk}$	\bar{C}_P	$t_{wc}/t_{wc,1}$
	[mW]	[m/s]	[-]	[-]
0	22.77	1.739	0.3825	-
1	+2.84%	+0.057%	-4.18%	1
2	+4.78%	+0.299%	-3.19%	1/4
4	+1.52%	-0.977%	-2.43%	1/16

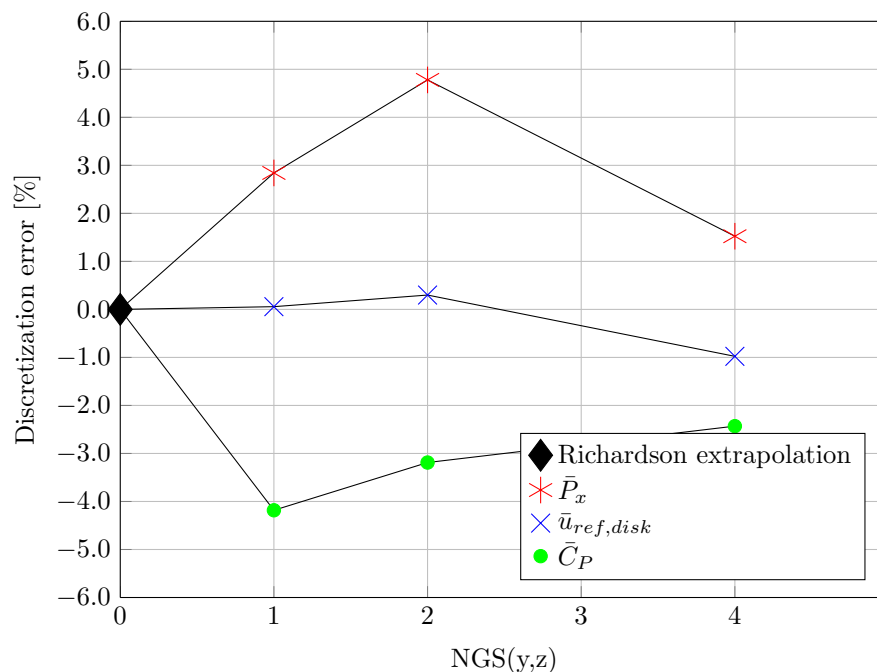


Figure E.2: Discretization errors as function of normalized grid spacing over y-grid and z-grid refinement.

From figure E.2 it is clear that neither performance measure exhibits grid convergence. Therefore, the resulting exact solutions by Richardson extrapolation are inaccurate and the found discretization errors not representative. Due to the absence of convergence, there is a strong indication that the performance measures are not exclusively grid-dependent while varying the yz-grid. The following issues are noted as possible sources for this result:

- For the yz-grid convergence the number of blade elements (annuli) varies according to half the number of cells over the disk.
- The regularization kernels are manually fine-tuned and thus not identical for each grid. Although the regularization kernels are fine-tuned down to 0.1% deviation between each grid, cell-local forcing per unit mass may differ.

Omitting these issues by keeping the number of blade elements and the regularization kernels constant for each grid in order to define a discretization error is not a proper approach. Even if a discretization error is found, the error would only hold for model applications that deviate from recommended practice.

Table E.4 gives the sensitivity of the performance measures with respect to yz-grid variation. Comparable with the x-grid convergence, the sensitivity to the grid variation is the largest for the power production. For all performance measures, the sensitivity is overall larger than for the x-grid convergence. Therefore, it may be expected that the discretization error for the yz-grid variation is larger than the discretization error for the x-grid variation, however, a supported quantification cannot be made. Figure E.3 gives the time-averaged streamwise flow profiles over turbine mid-plane at various distances behind the turbine for various yz-grids.

Table E.4: Sensitivity of performance measures with respect to yz-grid variation.

	\bar{P}_x	$\bar{u}_{ref,disk}$	\bar{C}_P
s	1.60%	0.645%	0.513%

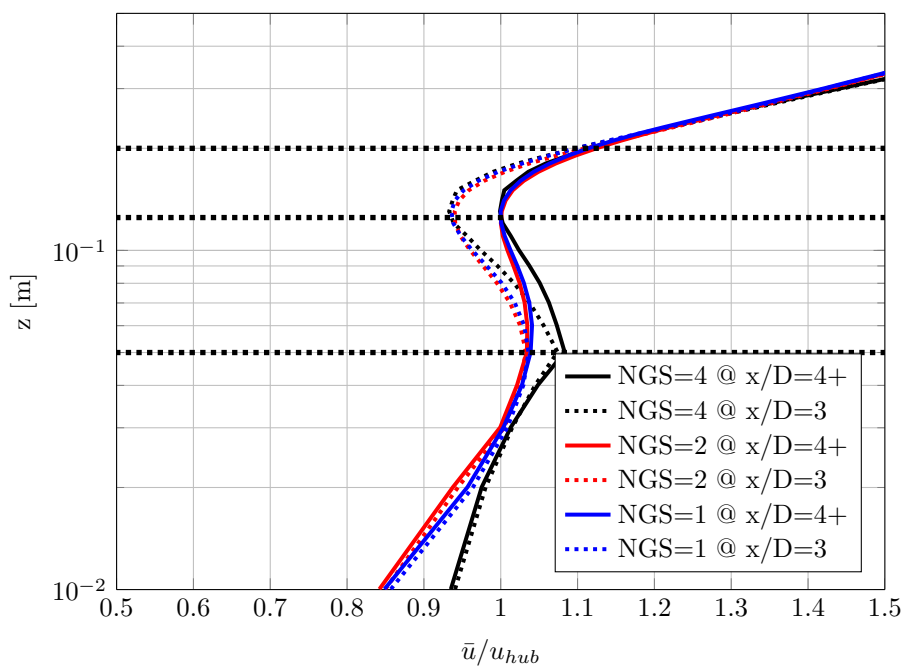


Figure E.3: Resulting time-averaged streamwise flow profiles over turbine mid-plane at various distances behind the turbine for various yz-grids. Dotted horizontal lines indicate the top tip height, hub-height and bottom-tip height.

In figure E.3, the coarsest (NGS(y,z)=4) yz-grid exhibits a strong deviation of the profile compared with the finer grids. The NGS(x,y)=4 grid is therefore considered inappropriate, deviating from the statement of grid requirement by Porté-Agel (2011). The difference in time-averaged streamwise flow profiles is the largest near the wall. It is fair to expect strong errors near the wall as a result of application of a coarser grid. Porté-Agel’s (2011) statement of 5 to 7 grid point on the disk is thus not necessarily incorrect. The wall-clock time of the NGS(x,y)=2 grid is approximately a factor four shorter than the NGS(x,y)=1 grid, while the sensitivity of the performance measures to xy-grid variation is relatively small. Therefore, the NGS(x,y)=2 grid is chosen as the final grid for all further advancements.

E.1.3 Smoothing and 2dx-waves suppression

During the study into grid convergence, both axial and radial smoothing widths, $N_{smooth,x}$ and $N_{smooth,r}$, were set to zero. With these settings, clear numerical errors were exhibited in the form of 2dx-waves for the spanwise and wall-normal flow fields. Such 2dx-waves are characteristic for central differential schemes as applied in DALESURBAN. In order to suppress these waves, upstream axial smoothing is further investigated.

2dx-waves are purely the result of numerical errors and their source is found at/near sudden changes in velocity. To fully suppress these waves the cell Peclet number should be smaller than 2 for each cell. Here, the cell Peclet number is defined by equation E.9 [13].

$$Pe_{cell} = \frac{u\Delta x}{(\nu_e + \nu)} \quad (E.9)$$

Assuming ν_e to approach zero for an infinitely fine grid, the theoretically required number of streamwise cells to fully suppress 2dx-waves is approximately 1.3×10^5 for a single domain. Such fine grid is unfeasible regarding wall-clock times on the currently available computational resources. A secondary option to reduce 2dx-waves is by reducing the intensity of the sudden change in velocity, which is already implemented within the wind turbine model by axial smoothing of the wind turbine momentum sink.

For axial smoothing, two additional parameters are required to be set: the axial smoothing width, $N_{smooth,x}$ and the axial regularization kernel, ϵ_x . To assess the influence of axial smoothing, the first is set to $N_{smooth,x} = 2$ and the second is set to $\epsilon_x = 0.8$. Figure E.4 gives the time-average spanwise and wall-normal velocities near turbine top-tip and bottom-tip for one case without axial smoothing and one case with axial smoothing. Here, the turbine is located at $x/D_{disk} = 1$. The applied axial smoothing resulted in a clear reduction of 2dx-waves, however full suppression can not be claimed. Table E.5 gives an overview of the performance measures of one case without axial smoothing and one case with axial smoothing. Differences are minor, therefore, no further optimization on axial smoothing parameters has been performed. Nevertheless, axial smoothing will be applied in all further runs as the intensity of 2dx-waves are reduced, improving the quality of the flow fields. Simultaneously, it is not expected that radial smoothing will result in any improvement in the magnitude of the 2dx-waves, while no clear singular behavior or other numerical errors near the radial edges of the disk are found. Therefore, the radial smoothing width is kept at zero while no further investigation is performed on its effect.

Table E.5: Time-averaged mean results on influence 2dx-waves and axial smoothing.

Case	\bar{P}_x [mW]	$\bar{u}_{ref,disk}$ [m/s]	\tilde{C}_P [-]
Without axial smoothing	23.85	1.7445	0.3703
with axial smoothing	-0.02 %	-0.28%	+0.81%

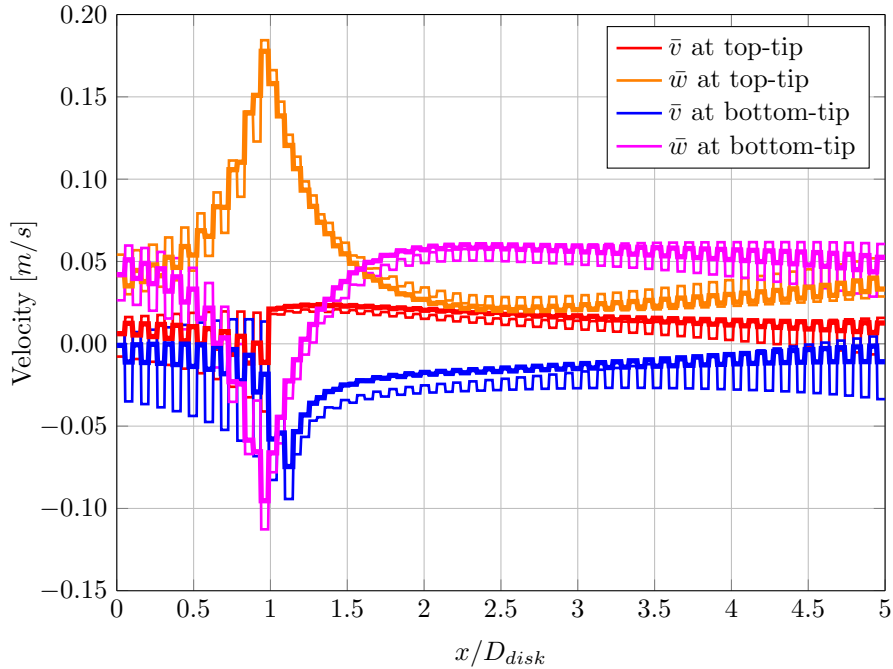


Figure E.4: Time-averaged spanwise and wall-normal velocities near top-tip and bottom-tip assessing the effect of axial smoothing; thin line is without smoothing, thick line is with smoothing.

E.2 Single domain temporal analysis

In order to estimate the required convergence time and statistical averaging period, comparisons are made with undisturbed channel flows. For these flows, time is usually scaled by $\frac{\delta}{u_\tau}$.

E.2.1 Convergence time

An initial estimation for the convergence time is based on the work on LES of turbulent channel flows by Mason and Callen (1986) [23]. Here, convergence was found at $t_{conv} \approx 20 \frac{\delta}{u_\tau}$. Figure E.5 gives the development of the sum of the wall and turbine induced shear, normalized with the imposed pressure difference. In accordance with equation 3.38, convergence to a stationary constant attractor of 1 occurs.

Trend-stationarity is verified by Kwiatkowski-Phillips-Schmidt-Shin (KPSS) test, where the null-hypothesis of trend-stationarity is rejected for a p-value below 0.05. For the expected value of a trend-stationary process, EV , equation E.10 holds, while, but not necessarily for all trend-stationary cases, $\mu_1 = 0$ is desired for this application.

$$EV \rightarrow \mu + \mu_1 t \quad \text{for} \quad t \rightarrow \infty \quad (\text{E.10})$$

From figure E.5 and KPSS tests, convergence is indeed found for $t_{conv} \geq 20 \frac{\delta}{u_\tau}$ s. Additionally, the streamwise bulk velocity and the power production, P_x , have been checked for convergence in a similar manner. Also for these variables, convergence is found for $t_{conv} \geq 20 \frac{\delta}{u_\tau}$ s.

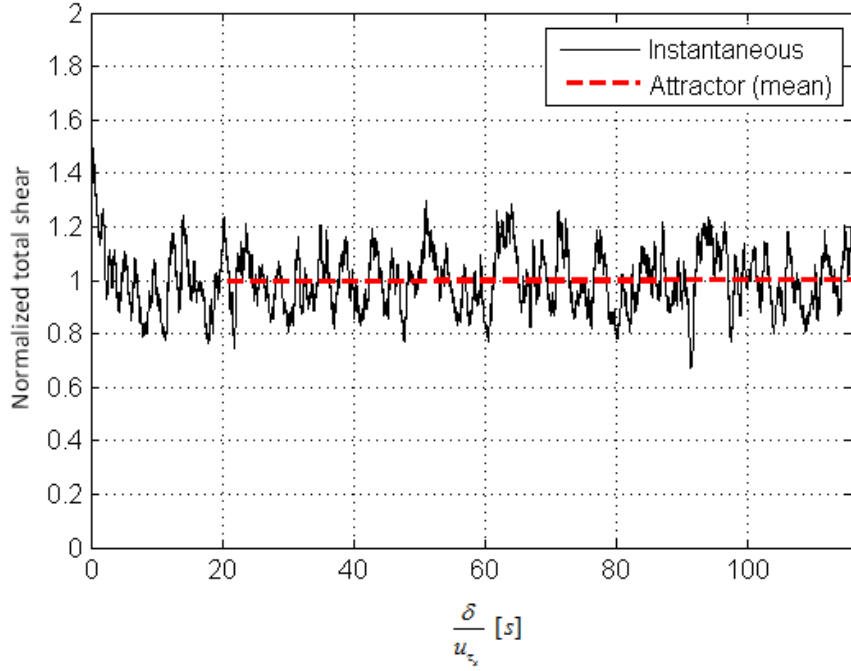


Figure E.5: Convergence of normalized total shear.

E.2.2 Statistical averaging period

The statistical averaging period is the period over which mean performance measures and mean fields are defined. The lower time boundary is immediately set after convergence is achieved and steady-state conditions are met: $t_{\text{stat,avg,low}} = 20 \frac{\delta}{u_\tau}$ s. To determine the appropriateness of the statistical averaging period, the following should hold as a result of steady-state conditions:

- Mean turbine performance measures approaching real mean, minimize sampling error.
- Full stationarity.
- Field symmetry for symmetric fields.

Sampling errors of performance measures

Over the instantaneous signals of the performance measures, P_x , $u_{ref,disk}$ and C_p , the means are determined for three consecutive time-averaging periods of a certain defined length. The resulting values are compared with each-other and with the 'real mean', hereby defined as the resulting mean over a time-averaging period of $T_{\text{stat,avg,real}} = 240 \frac{\delta}{u_\tau}$ s. Table E.6 gives the sampling errors compared with the 'real mean' for each of these three consecutive time-averaging periods. For $T_{\text{stat,avg}} = 120 \frac{\delta}{u_\tau}$ s only two consecutive periods are compared, while for $T_{\text{stat,avg}} = 200 \frac{\delta}{u_\tau}$ s only one period is given. Figure E.6 plots the development of the largest absolute sampling error of the three consecutive periods for each wind turbine performance measure as function of the number of samples. When comparing sampling errors of consecutive time-averaging periods with each-other: table E.6 indicates a decrease of difference in sampling error between each consecutive sampling period with increasing number of samples. Furthermore, the sampling error compared to the 'real mean' is found to decrease as function of the number of samples according to equation E.11. This function is plotted for each performance measure as the expected error in figure E.6.

$$E_{\text{sampling,expected}} = \frac{E_{\text{sampling}}(N_{\text{samples}} = 20640)}{(N_{\text{samples}}/20640)} = \frac{E_{\text{sampling}}(T_{\text{stat,avg}} = 10 \frac{\delta}{u_\tau})}{(T_{\text{stat,avg}}/10 \frac{\delta}{u_\tau})} \quad (\text{E.11})$$

Table E.6: Sampling errors of three consecutive time-averaging periods.

$t_{avg,stat}$	$N_{samples}$	Period	$E_{\bar{P}_x}$ [%]	$E_{\bar{u}_{ref,disk}}$ [%]	$E_{\bar{C}_p}$ [%]
$10 \frac{\delta}{u_\tau}$	20640	1	7.40	2.73	-0.15
		2	-0.38	0.03	0.56
		3	6.77	2.20	-0.15
$20 \frac{\delta}{u_\tau}$	41280	1	3.58	1.37	0.20
		2	-0.11	-0.15	0.12
		3	2.54	1.02	-0.10
$40 \frac{\delta}{u_\tau}$	82560	1	1.73	0.60	0.15
		2	-1.43	-0.46	-0.02
		3	0.49	0.14	0.02
$80 \frac{\delta}{u_\tau}$	165120	1	0.15	0.07	0.05
		2	-0.73	-0.25	-0.02
		3	0.58	0.18	-0.05
$120 \frac{\delta}{u_\tau}$	247680	1	0.26	0.09	0.05
		2	-0.26	-0.09	-0.05
$200 \frac{\delta}{u_\tau}$	412800	1	-0.35	-0.12	-0.04

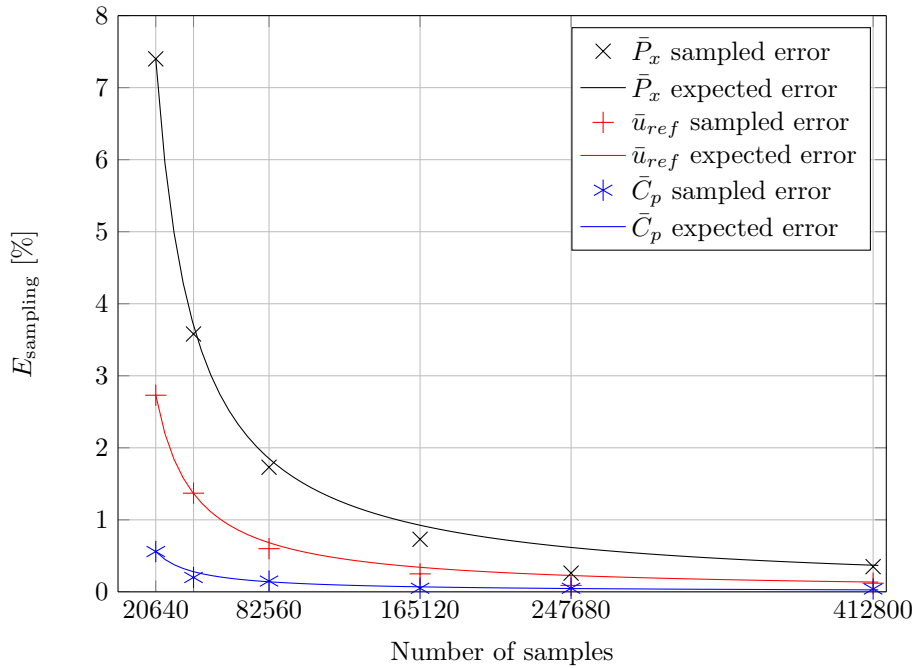


Figure E.6: Maximum absolute sampling error as function of number of samples for each wind turbine performance value. Both sampled and expected sampling error shown.

The sampling error is a simple error to suppress, the only limitation is wall-clock time. With a time-averaging period of $T_{stat,avg} = 200 \frac{\delta}{u_\tau}$ s, the required wall-clock time is approximately half a day for an fully resourced Intel Xeon E5-2643V2 @ 3.50GHz. By equation E.11, this results in an expected sampling error of 0.37% for the produced power and even lower errors for the other performance measures. For the single domain in this current application, it is therefore not necessary to optimize the sampling error versus the wall-clock time. To conclude, the final chosen time-averaging period is $T_{stat,avg} = 200 \frac{\delta}{u_\tau}$ s, resulting in $t_{stat,avg,low} = 20 \frac{\delta}{u_\tau}$ s and $t_{stat,avg,high} = 220 \frac{\delta}{u_\tau}$ s.

Stationarity and field symmetry

As previously stated in equation E.10, μ_1 should approach zero for a full stationary process indicating neither an average increase nor decrease in expected value. Defining stationarity according to equation E.12, table E.7 gives the stationarity of various instantaneous variables averaged over a set statistical averaging period. Additionally, flow fields that may be expected symmetric exhibit symmetry after averaging over a set statistical averaging period of $T_{stat,avg} = 220 \frac{\delta}{u_\tau}$, see appendix G for detailed time-averaged flow fields. Therefore, the chosen statistical averaging period is additionally proven appropriate.

$$STAT = 100 * \left(1 - \frac{|\mu_1|}{\mu} \right) \quad (E.12)$$

Table E.7: Stationarity of selected variables.

	\bar{P}_x	$\bar{u}_{ref,disk}$	\bar{C}_P	Total shear
STAT [%]	96.5	98.9	99.6	98.6

E.2.3 Wind turbine reference velocities averaging time

Equation E.13 repeats the method for time-averaging of the wind turbine reference velocities. Equation E.13 requires one fixed input: the reference velocity averaging time, T .

$$\langle \bar{u} \rangle_a = \frac{\Delta t_{RK}}{T} \langle u \rangle_a^{n-1} + \left(1 - \frac{\Delta t_{RK}}{T} \right) \langle \bar{u} \rangle_a^{n-1} \quad (E.13)$$

To determine the reference velocities averaging time, the instantaneous reference velocities are transformed by Fast Fourier Transform into a single-sided amplitude spectrum to determine the frequency of the small time-scale fluctuations as shown in figure E.7. All reference velocities show increased amplitudes at about 2.5 Hz and 5 Hz and every other multitude of 2.5 Hz with reduced amplitude. This 2.5 Hz small time-scale fluctuation frequency corresponds with the average domain flow-through time at wind turbine height. Therefore, the small time-scale fluctuations are dependent on the domain length and are therefore considered non-physical and the result of periodic contamination occurring for a single domain. Time-averaging of the wind turbine reference velocities is thus recommended to suppress response to this contamination error. For a single domain, T is set at 1s, approximately a multitude of 4 small time-scale fluctuations, i.e. domain length flow-throughs.

The John Hopkins University and KU Leuven applications also apply a time-averaging of the reference velocities, see chapter 2.5. Translating the time-averaging time-scale as previously defined for these applications by equation 2.35 to the current study, a time-averaging time of 1.4s and 3.1s would result respectively. Applied reference velocity averaging time is thus shorter than found in literature, while the definitions found in literature are not based on the number of flow-through times.

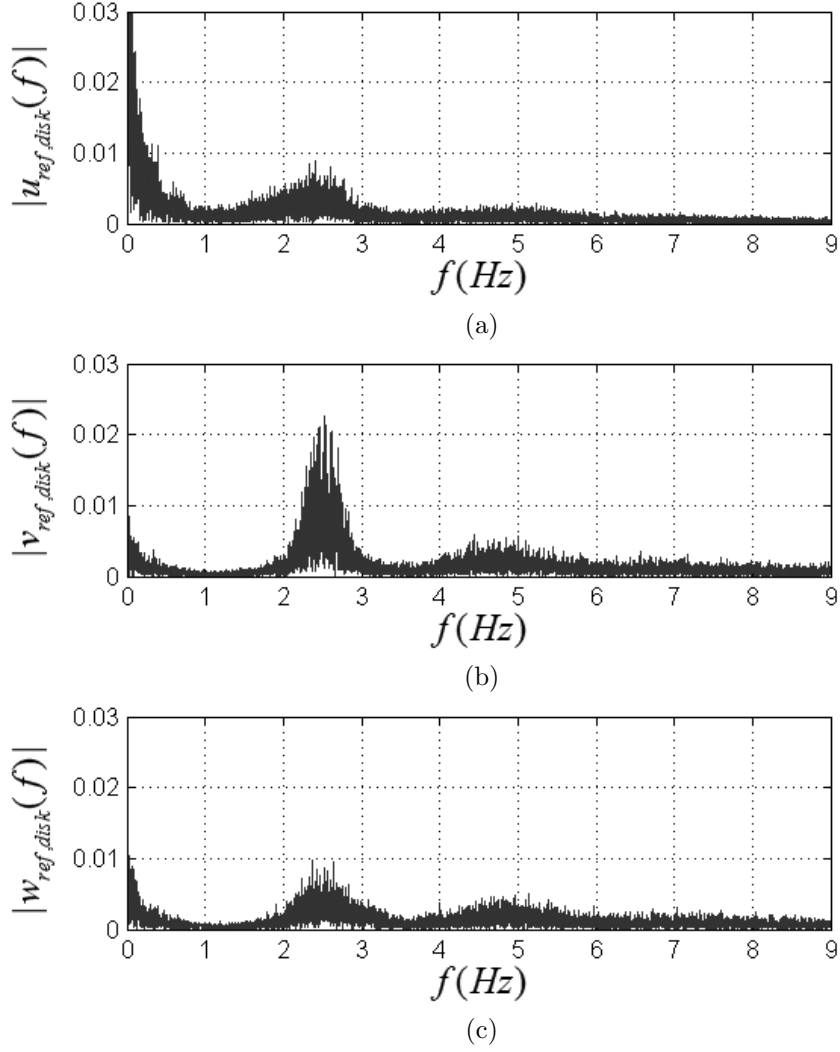


Figure E.7: Single sided amplitude spectra. (a) of instantaneous $u_{ref,disk}$, (b) of instantaneous $v_{ref,disk}$ and (c) of instantaneous $w_{ref,disk}$

E.2.4 Time-step and temporal discretization error

In DALESURBAN temporal discretization is dynamic during convergence to a steady state and limited by Courant-Friedrichs-Lewy criterion according to equation E.14, where CFL_{max} is chosen based on the applied advection scheme.

$$\max \left(\frac{u}{\Delta x} + \frac{v}{\Delta y} + \frac{w}{\Delta z} \right) \Delta t \leq CFL_{max} \quad (\text{E.14})$$

During the time-averaging period, the time-step is taken constant allowing for direct application of various post-processing methods such as Fast Fourier Transforms. To determine the temporal discretization error, three different runs with different time-steps during the time-averaging period are compared. The same method for the definition of the spatial discretization error is applicable for the definition of the temporal discretization error [27]. Table E.8 gives the resulting performance measures for three runs, each run identified by a normalized time-step (NTS). Figure E.8 gives a graphical representation of the time-step convergence and table E.9 gives the sensitivity of the model to time-step variation, whereas sensitivity is defined analogous to equation E.8.

Table E.8: Temporal discretization errors.

NTS	\bar{P}_x	$\bar{u}_{ref,disk}$	\bar{C}_P	$t_{wc}/t_{wc,1}$
	[mW]	[m/s]	[-]	[-]
0	23.67	1.7416	0.3732	-
1	+0.981%	+0.232%	-0.655%	1
1.5	+0.478%	+0.105%	-0.844%	3/4
2	+0.725%	+0.163%	-0.603%	1/2

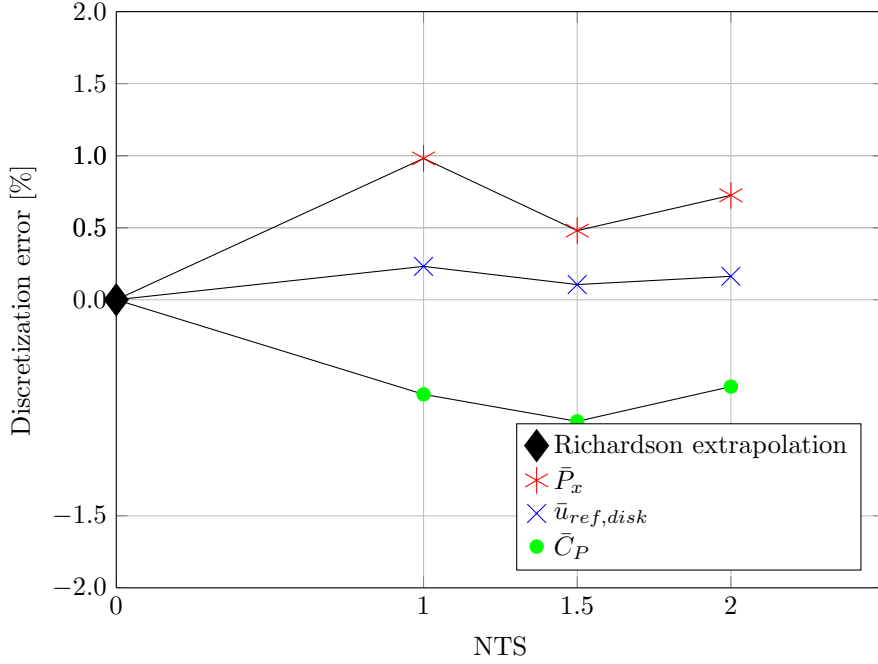


Figure E.8: Discretization errors as function of normalized time-step, NTS.

Table E.9: Sensitivity of performance measures with respect to time-step variation.

	\bar{P}_x	$\bar{u}_{ref,disk}$	\bar{C}_P
s	0.3741%	0.0946%	0.1820%

From figure E.8 it is clear that neither performance measure exhibits convergence on time-step variation. Therefore, the resulting exact solutions by Richardson extrapolation are again inaccurate and the found discretization errors not representative. Table E.9 gives the sensitivity of the model to time-step variation. Here it is found that the sensitivity of the model to time-step variation is about a factor 5 smaller than the sensitivity to yz-grid variation. Furthermore, it is the expectation that the absence of convergence is the result of minimal sensitivity of the model to time-step variation and the relatively large sampling error with respect to this sensitivity. Therefore, it is concluded that the discretization error due to time-discretization is negligible compared to spatial-discretizations and the largest fixed time-step satisfying the CFL criterion is chosen due to highest wall-clock time efficiency.

E.3 Subgrid modeling

To assess the influence of the subgrid model on results, the following subgrid models are compared:

- Smagorinsky, $C_s = 0.10$
- Smagorinsky, $C_s = 0.165$
- Smagorinsky, $C_s = 0.20$
- Vreman, $C_v = 0.07$

For more information on the Smagorinsky subgrid model and/or Vreman subgrid model, refer to Alberto (1993) [35] and/or the work by Vreman [40] [41], respectively. Note that the influence of the subgrid is grid dependent, for coarser grids the subgrid contribution increases and therefore the influence of the subgrid model on results is most likely to increase. Study into the influence of the subgrid model is performed only for the final chosen grid as defined in chapter E.1 with all temporal aspects as defined in chapter E.2. Therefore presented results and conclusions are only valid for this specific grid. Table E.10 gives mean turbine performance measure for the Smagorinsky model with a constant of 0.10 and compares the results of the other models. Also, the local relative maximum subgrid energy near the turbine and the overall relative subgrid energy are given, defined by equation E.15 and E.16 respectively. Here, the term $2\nu_e|\bar{S}|$ is an approximation for the subgrid energy and valid for both Smagorinsky and Vreman subgrid models [40].

$$SGSE_{local} = 100 * \frac{\overline{2\nu_e|\bar{S}|}}{2\nu_e|\bar{S}| + 0.5 \left(\overline{\left(\frac{u'u'}{u'u'} \right)} + \overline{\left(\frac{v'v'}{v'v'} \right)} + \overline{\left(\frac{w'w'}{w'w'} \right)} \right)} \quad (E.15)$$

$$SGSE_{overall} = \frac{\iiint SGSE_{local} dV}{V} \quad (E.16)$$

$$SGS_{dissipation} = \overline{2\nu_e|\bar{S}|}|\bar{S}| = \overline{(u'_i u'_j)_{sgs}} \frac{1}{2} \left(\frac{\partial \bar{u}_i}{\partial x_j} + \frac{\partial \bar{u}_j}{\partial x_i} \right) \quad (E.17)$$

From table E.10 it is found that local maximum and overall relative subgrid energy increases with increasing Smagorinsky constant and thus local eddy viscosity increases analogously, i.e. mostly linearly. Furthermore, the influence of the Smagorinsky constant on wind turbine performance is significant and a proper choice of the subgrid model is required. Comparing velocity profiles and various flow fields of the runs with different Smagorinsky constant with validation data, resulted in no clear 'best case'. According to equation 2.19, an increased eddy viscosity results in an increased production of turbulent kinetic energy. Therefore, an increased subgrid dissipation of mean kinetic energy is to be expected as both subgrid models are fully dissipative and allow no backscatter. The Smagorinsky model is known to overestimate the turbulent dissipation for regions with high shear, such as near the wall and the wind turbine wake boundary [40]. For a channel flow, the Vreman model with a Vreman constant of 0.07 approaches the Smagorinsky model with a Smagorinsky constant of 0.17 outside of regions of high shear [40]. Therefore, it is considered fair to compare the Vreman model with the Smagorinsky model with the Smagorinsky constant set as $C_s = 0.165$.

Figure E.9 gives the subgrid dissipation over the midplane just behind the turbine calculated according to equation E.17 [40] for the Smagorinsky model and the Vreman model. Three areas of increased subgrid dissipation are identifiable: the wall, wake boundary (near turbine bottom-tip and top-tip) and around the nacelle. As expected, the Smagorinsky model gives higher subgrid dissipation near all areas of high shear. Simultaneously, while not shown in figure E.9, the subgrid dissipation near the wall is nearly identical for both subgrid models. This is most

likely due to the application of a wall function instead of actually resolving the wall. Again it is not possible to define a 'best case' by comparison with validation data, while differences in wind turbine performance between the Smagorinsky and Vreman model are small. Therefore, assuming an overestimation of the subgrid dissipation by the Smagorinsky model near regions of high shear, simply because theory states so [40], it is concluded that the Vreman model gives better results around the turbine and therefore the Vreman model is chosen as the definitive subgrid model for all further advancement.

Table E.10: Time-averaged mean results on influence 2dx-waves and streamwise smearing.

Case		\bar{P}_x [mW]	$\bar{u}_{ref,disk}$ [m/s]	\bar{C}_P [-]	$SGSE_{local}$ [%]	$SGSE_{overall}$ [%]
Smagorinsky	$C_s = 0.10$	22.80	1.7245	0.3644	8.9	2.73
Smagorinsky	$C_s = 0.165$	+5.00 %	+1.29 %	+1.98%	15.6	4.78
Smagorinsky	$C_s = 0.20$	+4.82 %	+1.25 %	+1.92%	19.6	5.59
Vreman	$C_v = 0.07$	+4.60 %	+1.16 %	+1.62%	13.5	4.56

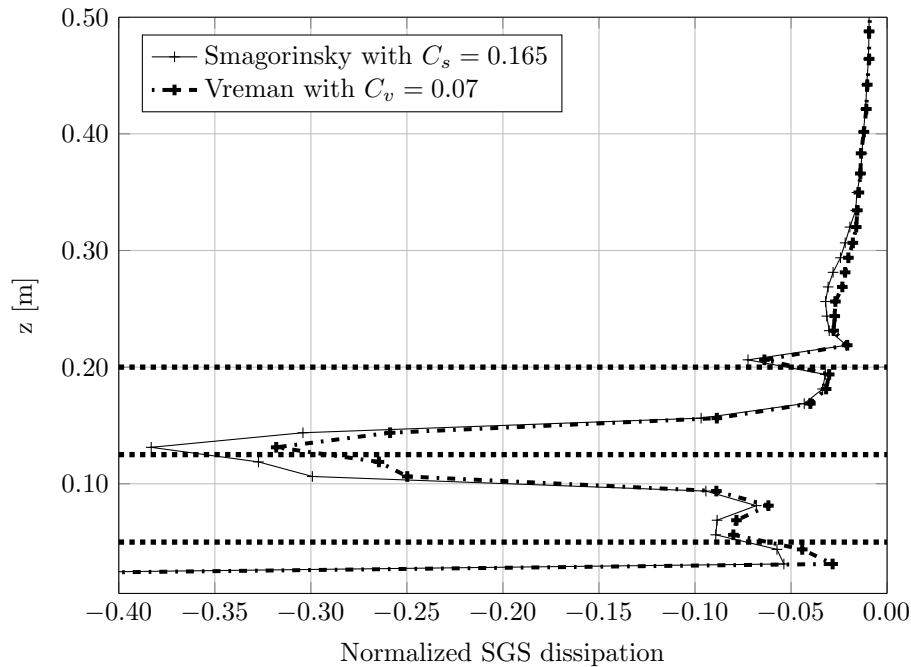


Figure E.9: Subgrid scale dissipation normalized with total pressure work pressure work $\left(\bar{u}_{bulk} \left[\frac{\Delta p_{mod}}{L_x} \right] L_z\right)$ for the Smagorinsky and Vreman model plotted in the midplane directly behind the turbine.

Appendix F

The infinite domain

The infinite domain is set-up as a multitude of single wind turbine domains. For this domain, the number of turbines in a column and the number of turbines in a row are determined and some temporal parameters are assessed. Table F.1 gives the unknown model inputs for the infinite domain.

Table F.1: Unknown model inputs for the infinite domain, require parametrization.

Input	Symbol	Unit
Number of columns	N_{column}	-
Number of rows	N_{row}	-
Convergence time	t_{conv}	s
Statistical avg. period	$T_{stat,avg}$	s
Reference avg. time	T	s

F.1 Domain dimensions

To determine the number of turbines in a column and the number of turbines in a row forming the infinite domain, three conditions are defined:

- Minimize periodic contamination.
- Containment of largest relevant large-scale structures.

Minimization / suppression of periodic contamination is required to simulate a physically realistic case, while simultaneously the infinite domain should be capable of containing the largest relevant large-scale structures. To check the appropriateness of the number of columns and the number of rows, cross-correlations between the reference velocities of the turbines are investigated. Two domains are proposed expected to fit above conditions:

1. Number of turbines in column = 6 Number of turbines in row = 6
2. Number of turbines in column = 12 Number of turbines in row = 6

Additionally, turbines are numbered column first, row second. For example: for the second proposed infinite domain the turbines in the first column are numbered 1 to 12 and in the second column 13 to 24 etc. Figure 3.9 gave a graphical representation of the turbine numbering of the second proposed infinite domain.

Number of columns (domain width)

The domain width is considered appropriate if the cross-correlation between a turbine on the first column and a turbine on the fourth column is near zero. This requirement indicates no response between these turbines and thus, all relevant large-scale structures with respect to the domain width are contained. To check if the width of the domains is appropriate, the cross-correlation of the streamwise and spanwise reference velocity of two turbines are shown in figures F.1 and F.2. The chosen two turbines are turbine 1 and the turbine on the fourth column with the highest corresponding cross-correlation coefficient. For both domains, the cross-correlation coefficient is close to zero while each peak-to-peak corresponds with a streamwise domain flow-through time. Therefore, the domain width appears to be appropriate.

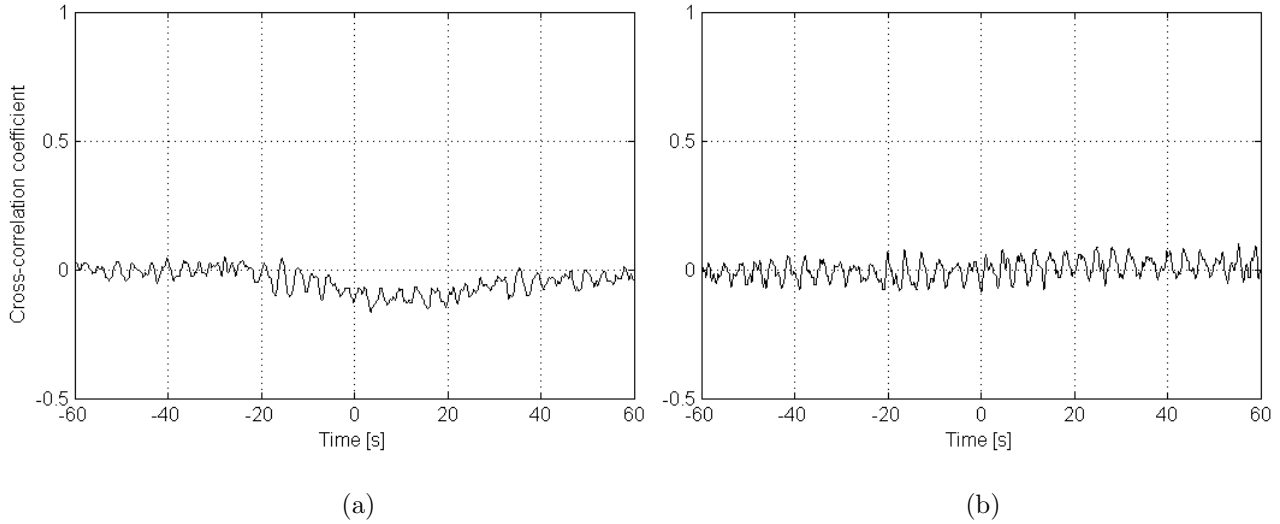


Figure F.1: Cross-correlations to determine appropriate domain width for the first domain, (a) Streamwise reference velocity, (b) Spanwise reference velocity.

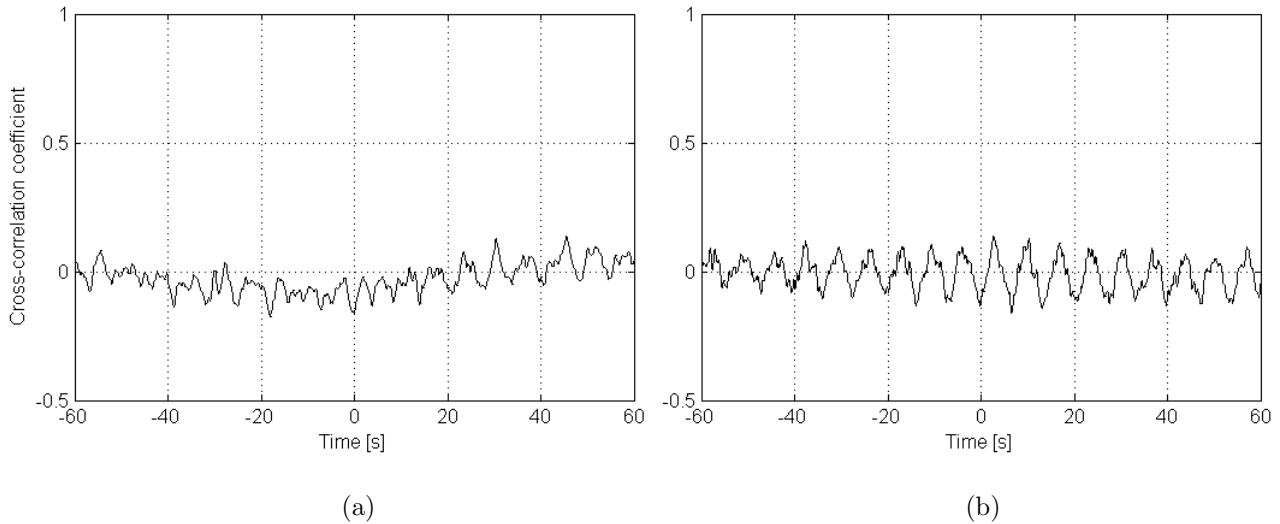


Figure F.2: Cross-correlations to determine appropriate domain width for the second domain, (a) Streamwise reference velocity, (b) Spanwise reference velocity.

Number of rows (domain length)

Ideally, the domain length is considered appropriate if a wind turbine within the double periodic domain does not respond to itself after one flow-through delay. In that case, all large-scale structures with respect to the domain length are contained within the domain and no periodic contamination occurs, i.e. fully physical conditions. The cross-correlation of the streamwise and spanwise reference velocity of two turbines in one column are shown in figures F.3 and F.4. The chosen turbines are located in the column in which the streamwise cross-correlation coefficient of the first row and last row is the highest. For the first domain cross-correlations are defined for turbine 1 and turbine 6. For the second domain cross-correlations are defined for turbine 1 and turbine 12.

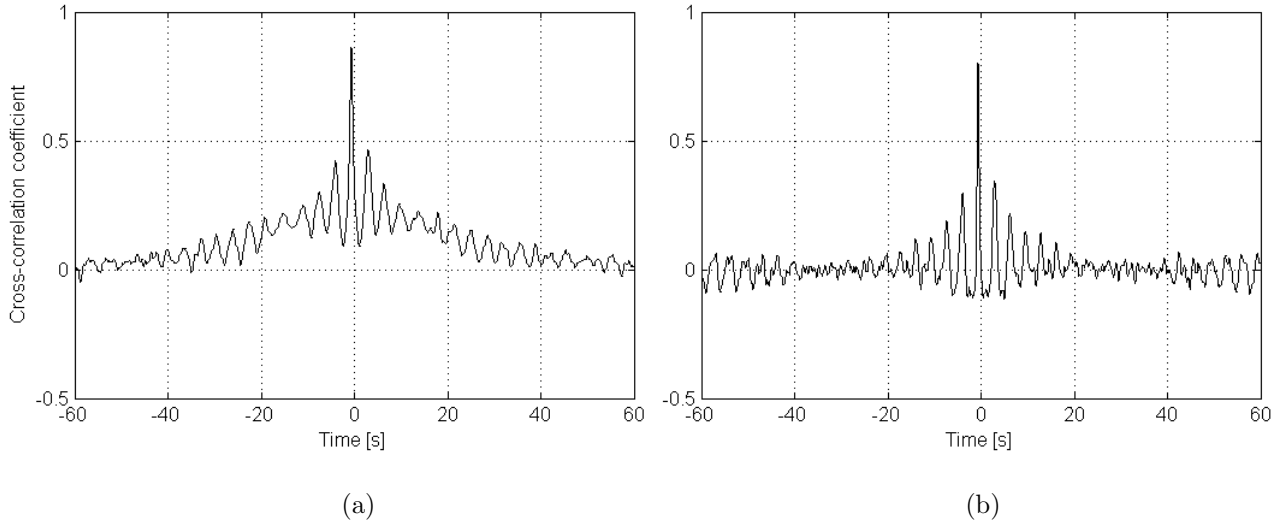


Figure F.3: Cross-correlations to determine appropriate domain length for the first domain, (a) Streamwise reference velocity, (b) Spanwise reference velocity.

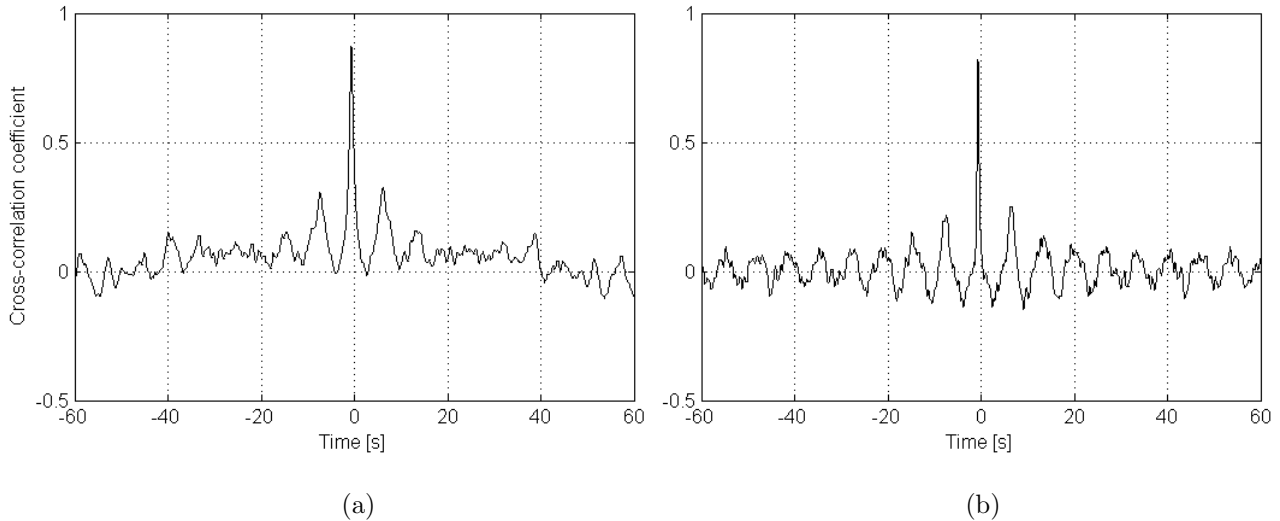


Figure F.4: Cross-correlations to determine appropriate domain length for the second domain, (a) Streamwise reference velocity, (b) Spanwise reference velocity.

The cross-correlations from figures F.3 and F.4 exhibit a near unity peak in past time. This peak occurs over a negative time (past) and is the correlation of the first turbine with the last turbine. This response is as expected as the first turbine is only one turbine spacing from the last turbine due to periodicity of the domain. Therefore, the past-time correlation is not of importance in the determination of the appropriateness of the domain length as it is independent of domain length.

Figure F.3 indicates a strong correlation for both streamwise and spanwise reference velocities between the first and last turbine in a column for the first domain. A significant positive streamwise correlation holds for the whole flow-through time, an indication of a strong continuous periodic contamination. This periodic contamination results in a continuously returning signal which does not die out over a multitude of streamwise flow-through times. Clearly, the domain length of the first domain is not appropriate.

Figure F.4 again indicates a strong correlation for both streamwise and spanwise reference velocities between the first and last turbine in a column for the second domain. However, the correlation between the first and last turbine in a column does approach zero within one flow-through, indicating a strong decrease in periodic contamination compared with the first domain. The signal of the first turbine does return rather strongly after one flow-through but is nearly lost after the second flow-through. Cross-correlations for the second domain are certainly not perfect but a great improvement over the first domain. Based on the cross-correlations of the second domain, the following recommendation can be stated for the domain size in order to greatly suppress periodic contamination:

- Number of turbines in column = 48 Number of turbines in row = 6

The infinite domain size is also limited by the available wall-clock time. Therefore, recommended domain size to greatly suppress periodic contamination is not feasible and the final chosen domain for all further infinite domain simulations is domain 2.

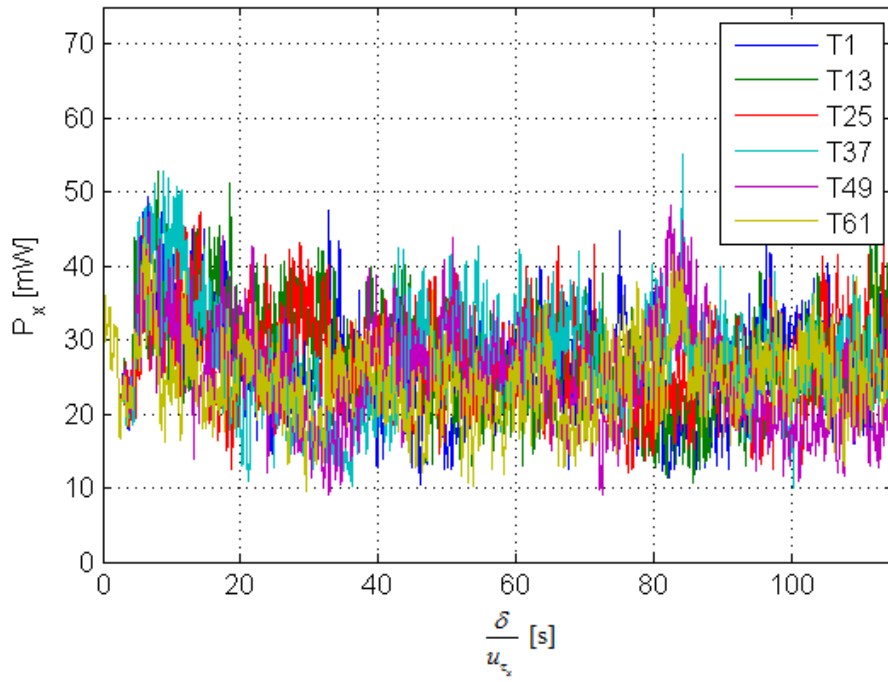
F.2 Power production time-series and temporal analysis

Figure F.5(a) gives the time-averaged time-series of the power production of 6 turbines in the first row as a result of set $T = 1$ s as applied in the single domain simulations. By applying additional time-averaging over $1 \frac{\delta}{u_r}$ s, the large correlation between the large reference velocity fluctuations becomes apparent, as is shown in figure F.5(b). In accordance with the cross-correlations of figures F.2(a) and (b), no clear correlation of the power production between the turbines on the same row is found. Figure F.6(a) gives the time-averaged time-series of the power production of 6 turbines in the first column as a result of set $T = 1$ s. Again, by applying additional time-averaging over $1 \frac{\delta}{u_r}$ s, the large correlation between the large reference velocity fluctuations becomes apparent, as is shown in figure F.6(b). All turbines produce approximately the same power with a slight on distance increasing time-lag compared with the first turbine. Therefore, the power production of a column of turbines is indeed highly correlated as previously found in figures F.4(a) and (b).

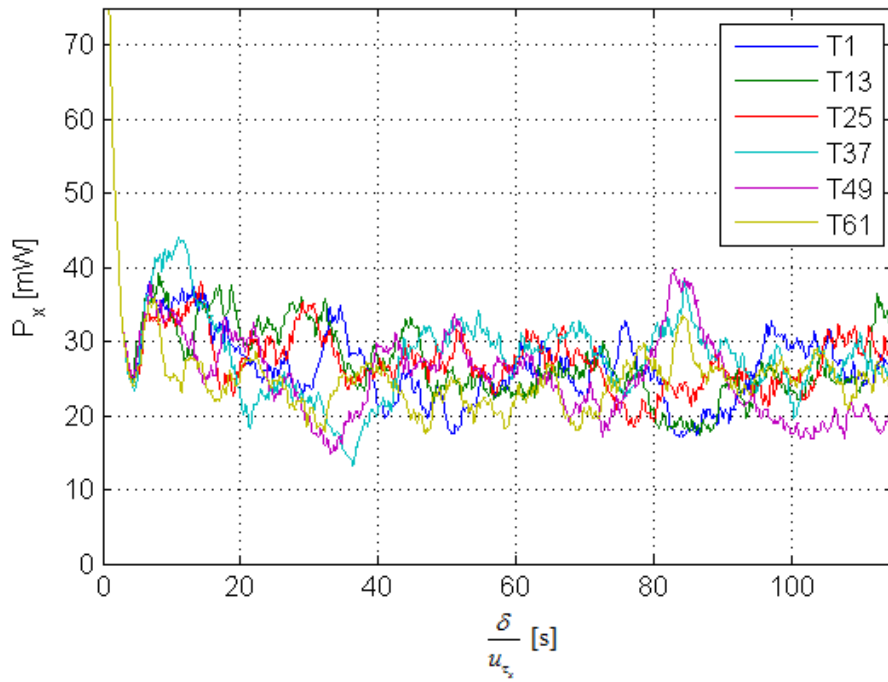
Wind turbine reference velocities averaging time

The frequency of the high-frequency fluctuations in figures F.5(a) and F.6(a) are, comparable with the single domain simulations, approximately in accordance with the domain flow-through time at hub-height. This is a strong indication that periodic contamination is still present even in the largest domain and that these fluctuations are not the result of a physical process that could induce such fluctuations, such as wake meandering. To mitigate these high-frequency fluctuations, an increase in the averaging time, T and/or an increase in the domain length are options. For the increase of the averaging time, a multitude of domain flow-through times is found to be appropriate. However, increasing the averaging time during processing also introduces an increased response delay of the turbine to the instantaneous reference velocities. Also, an increase in the domain size is computationally too expensive. Therefore, also for the infinite domain, the

If averaging time is applied while for time-series analysis purposes, an additional averaging time over $1 \frac{\delta}{u_z}$ s is applied in post-processing.

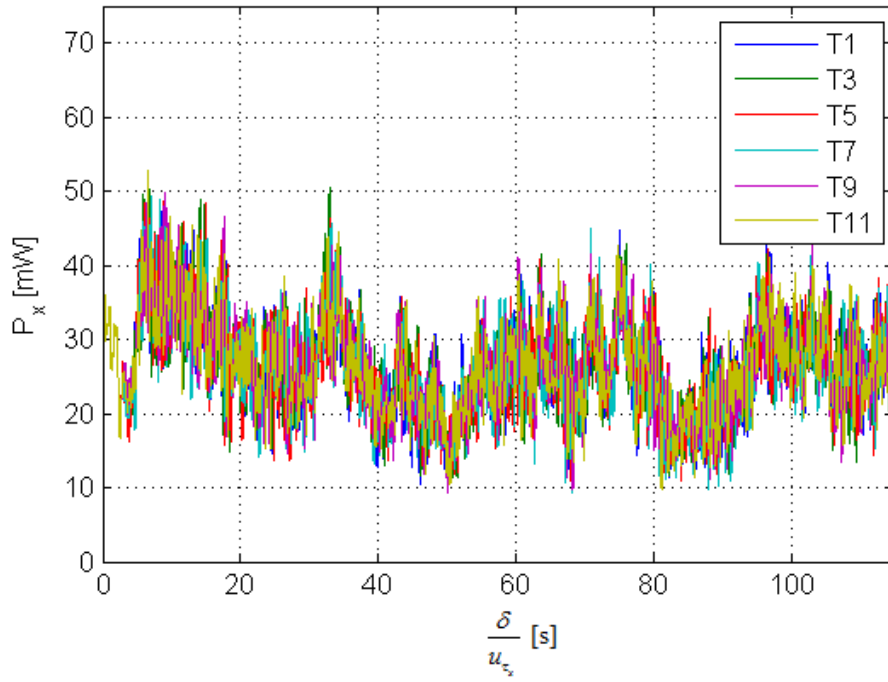


(a)

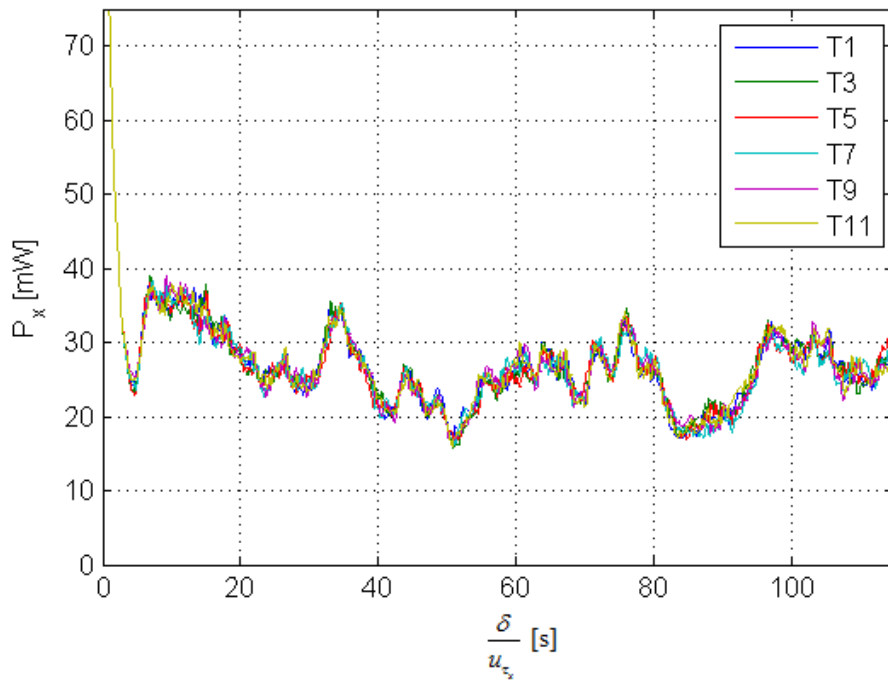


(b)

Figure F.5: Time series of power production of 6 turbines in the first row. (a) As a result of $T=1$ s. (b) Additionally time-averaged in postprocessing.



(a)



(b)

Figure F.6: Time series of power production of 6 turbines in the first column. (a) As a result of $T=1$ s. (b) Additionally time-averaged in post-processing.

Convergence time

Figure F.7 gives the time-series of the total sum of produced power over all 72 turbines. The convergence time for the single domain is set at $20 \frac{\delta}{u_\tau}$ s, while figure F.7 indicates an ongoing development of the total sum of the produced power even past $20 \frac{\delta}{u_\tau}$ s. Full convergence of the overall summed power production for all 72 turbines is found for $40 \frac{\delta}{u_\tau}$ s.

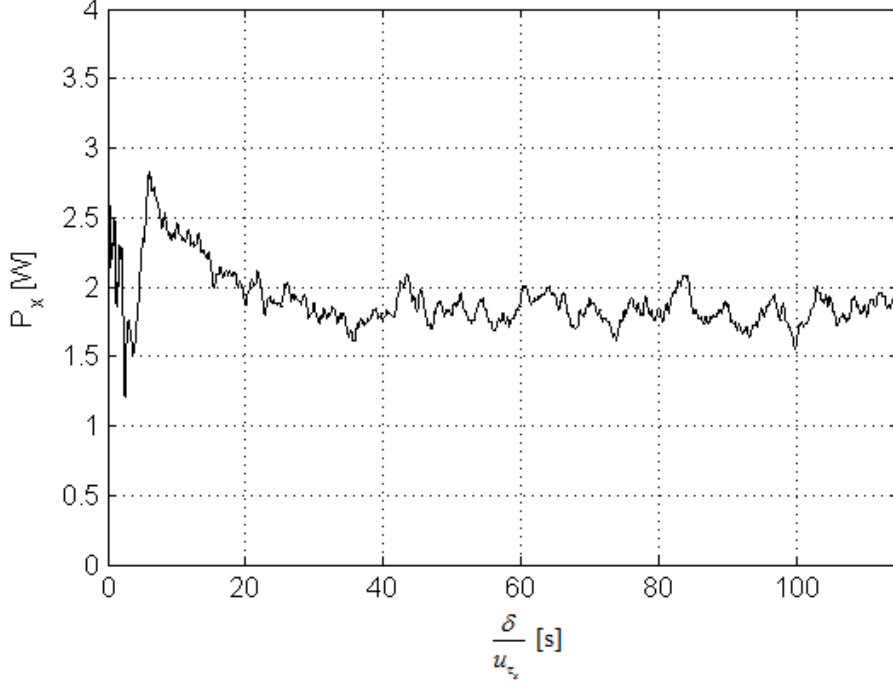


Figure F.7: Time series of sum of power production of all 72 turbines.

Statistical averaging period and sampling error performance measures

Table F.2 gives the sampling error of the combined wind turbine performance measures of all 72 turbines, here, the sampling error is compared with the long-time averages of $T_{stat,avg} = 80 \frac{\delta}{u_\tau}$ s. Figure F.8 gives the corresponding maximum absolute sampling error as function of number of samples. Here, the expected errors are defined according to equation E.11.

The expected error as analogously defined by equation E.11, does not match the measured error in figure F.8. Either, the long-time averages of $T_{stat,avg} = 80 \frac{\delta}{u_\tau}$ s are inappropriate, and/or, the statistical averaging period of $T_{stat,avg} = 10 \frac{\delta}{u_\tau}$ s is too short and corresponds with a too low number of fluctuations to filter out any extremities. Nevertheless, the sampling error appears to be smaller overall than for the single domain. Furthermore, comparing the level of fluctuation of the combined instantaneous power production signal, figure F.7, to the same signal for a single wind turbine, figure F.5, it is expected that the required sampling time is smaller for the combined signal. The final chosen statistical averaging period is set at $T_{stat,avg} = 60 \frac{\delta}{u_\tau}$ s, about 70% lower than for the single domain. This choice results in a reduced wall-clock time of the infinite domain simulations, yet with an accurate estimation of the overall wind farm performance. The resulting time-averaged performance for each single wind turbine is however not as accurate, and only the instantaneous signal of these turbines should be taken into account for the final analysis.

Table F.2: Sampling errors of three consecutive time-averaging periods for the second infinite domain for the instantaneous signal for the combined wind turbine performance of all 72 turbines.

$T_{avg,stat}$	$N_{samples}$	Period	$E_{\bar{P}_x}$ [%]	$E_{\bar{u}_{ref,disk}}$ [%]	$E_{\bar{C}_p}$ [%]
$10 \frac{\delta}{u_\tau}$	20640	1	1.74	0.64	0.05
		2	-1.34	-0.47	0.05
		3	2.85	1.00	0.02
$20 \frac{\delta}{u_\tau}$	41280	1	0.19	0.08	0.02
		2	0.34	0.14	0.09
		3	-0.48	-0.22	-0.09
$40 \frac{\delta}{u_\tau}$	82560	1	0.26	0.11	0.05
		2	-0.25	-0.11	-0.07
$60 \frac{\delta}{u_\tau}$	123840	1	0.01	-0.01	0.00

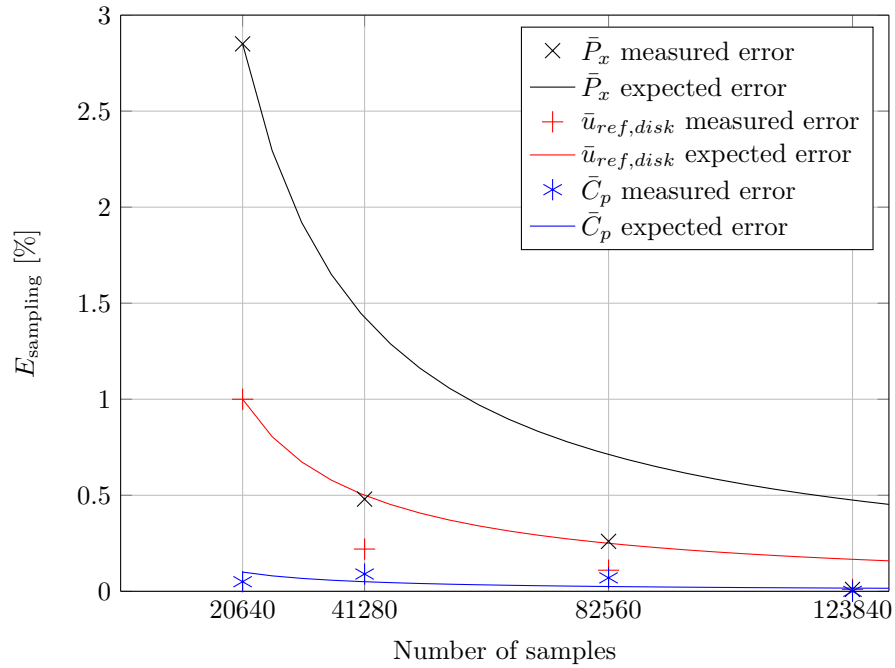


Figure F.8: Maximum absolute sampling error as function of number of samples for the second infinite domain for the instantaneous signal of the combined wind turbine performance of all 72 turbines. Both sampled and expected sampling error are shown.

Appendix G

Single domain flow fields

The following time-averaged flow fields of the single domain are presented:

- Local SGS energy percentage as defined by equation E.15.
- Streamwise velocity.
- Reynolds stress $\overline{u'u'}$.

Local SGS energy percentage as defined by equation E.15 in the turbine midplane, figure G.1.

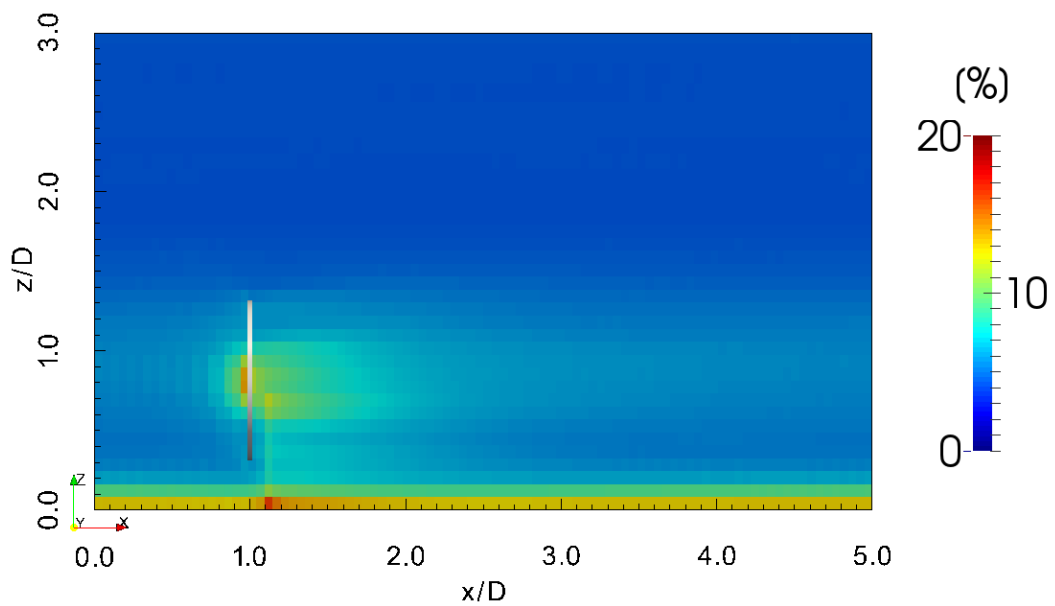


Figure G.1: Non-uniform actuator disk: local subgrid scale energy percentage.

Time-averaged streamwise velocity field in the turbine midplane, figure G.2, and in the horizontal plane through hub-height, figure G.3.

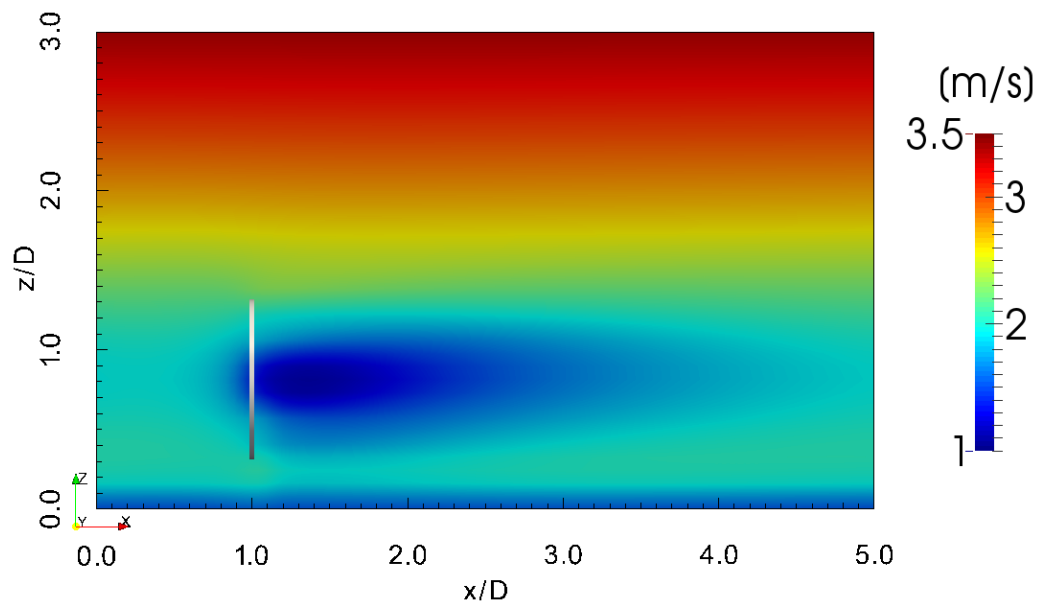


Figure G.2: Non-uniform actuator disk: stream-wise velocity over midplane.

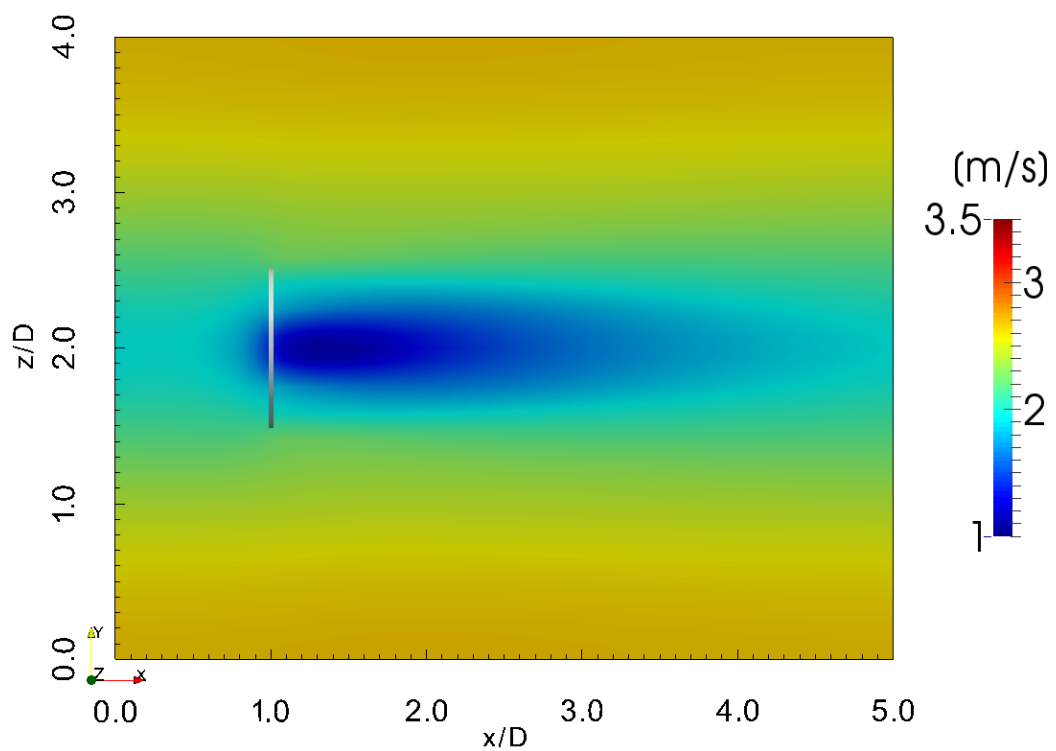


Figure G.3: Non-uniform actuator disk: stream-wise velocity over horizontal plane through hub-height.

$\overline{u'u'}$ field in the turbine midplane, figure G.4, and in the horizontal plane through hub-height gives $\overline{u'u'}$ field in the turbine midplane, figure G.5.

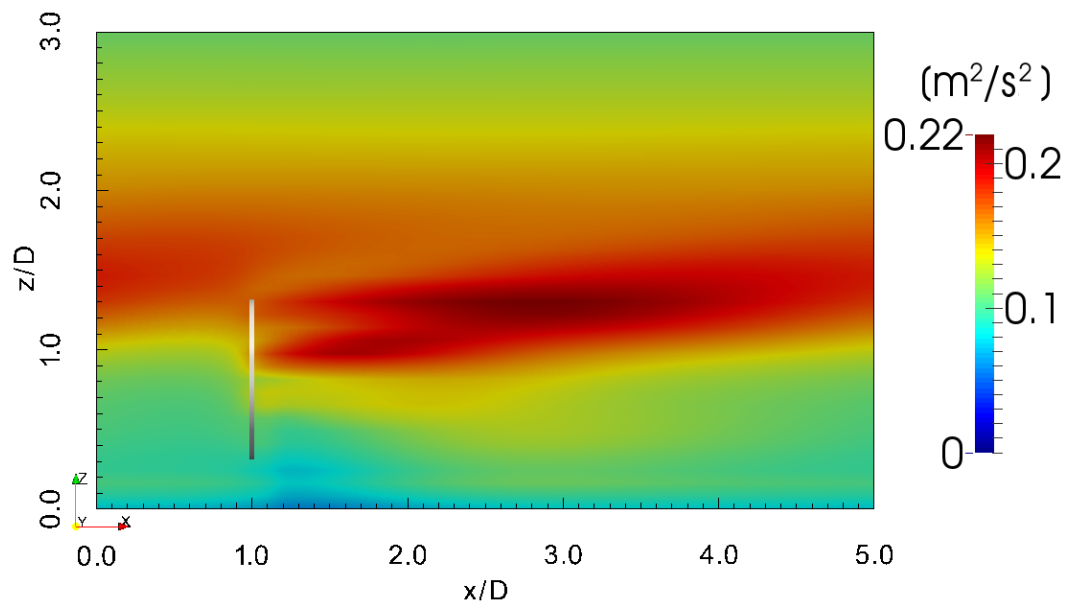


Figure G.4: Non-uniform actuator disk: $\overline{u'u'}$ over midplane.

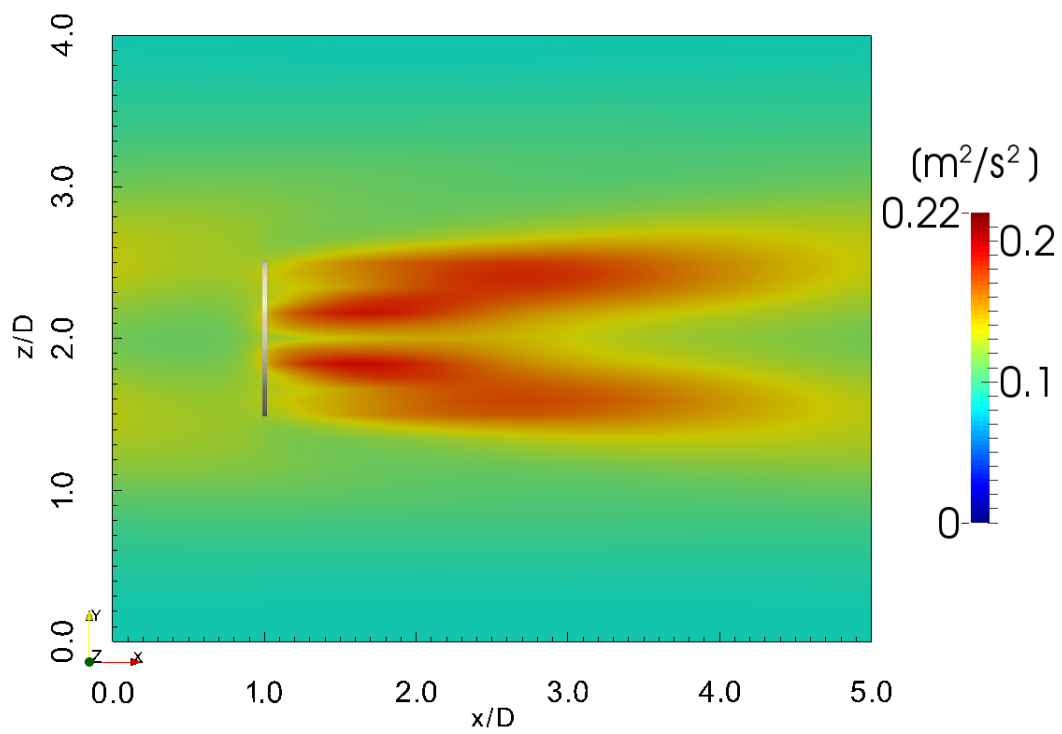


Figure G.5: Non-uniform actuator disk: $\overline{u'u'}$ over horizontal plane through hub-height.